ENGINEERING OF FLUORESCENCE NANODIAMONDS IN A PLASMA DISCHARGE

A Dissertation

by

ABDURRAHMAN ABDULLAH A. ALMETHEN

Submitted to the Office of Graduate and Professional Studies of
Texas A&M University
in partial fulfillment of the requirements for the degree of

DOCTOR OF PHILOSOPHY

Chair of Committee,	Alexei V. Sokolov
Co-chair of Committee,	Phillip R. Hemmer
Committee Members,	M. Suhail Zubairy
	Aleksei M. Zheltikov
Head of Department,	Grigory Rogachev

May 2018

Major Subject: Physics

ABSTRACT

The fourth state of matter (plasma state) was first discovered in an electrical discharge tube (Crookes tube) and named as a radiant matter in 1879 by Sir William Crookes. Nowadays, plasma discharges have innumerable uses in several fields such as material processing, growth, etc. Plasma discharges can be created by electric fields that are AC, DC, Radio Frequency (RF), or Microwave (MW) or a combination, depending on the applications. Examples of plasma applications include growth by plasma-enhanced chemical vapor deposition (PECVD), etching, sputtering, implantation, and oxidation. For RF plasmas, either inductive and capacitive coupling can be used, and are common for synthesizing nanomaterial in the gas phase or in plasma-liquid interactions.

For plasma assisted growth of diamonds, either homogeneous and heterogeneous nucleation mechanisms can occur depending on the type of plasma discharge and other reaction conditions. For example, growth can be at high pressure, atmospheric pressure, and low pressure. Starting materials for nanodiamonds (NDs) can be hydrocarbons like ethanol (C_2H_6O) or low molecular weight hydrocarbons like CH_4 and C_2H_4.

For more controlled growth, diamondoids like Adamantane ($C_{10}H_{16}$), can be used as diamond seeds because they resemble a single lattice unit of diamond. Recently, more complex diamondoids as seeds such as pentamentane ($C_{26}H_{32}$) have been employed for constructing NDs with high efficiency by MW plasma chemical vapor deposition (CVD).

The present work is a study that focuses on nucleation, engineering, and size controlling of NDs; it is motivated by the need to develop more controlled techniques for

synthesizing or growing NDs especially for the formation of nitrogen-vacancy ($N\text{-}V^{-}$) and silicon-vacancy (Si-V) centers. Based on the type of plasma source, the work was divided among three main projects. The first one was centered on studying the DC plasma discharge method at short and long distances between the electrodes as well as at various levels of vacuum. The second project concentrated on manufacturing NDs by applying capacitively coupled RF plasma discharges under various conditions. The third project involved the use of microwave plasma.

DEDICATION

To the spirits of my parents Norah and Abdullah,

To my loyal wife Hend A. Aldamegh,

To my sisters and brothers

To my beautiful daughters Maymouna and Hajer,

To my fabulous sons Abdullah, Abdulmalik, and Abdulilah

ACKNOWLEDGEMENTS

First and foremost, I would like to thank Allah (Subhanahu Wa Ta'ala) the most glorified, the most high for giving me strength, ability, and enthusiasm to complete my graduate study. Without his blessings, this accomplishment would not have been conceivable and achieved.

Second, I would like to deeply thank my advisor Dr. Philip Hemmer for his patience, guidance, support, warmth and open personality which have been more valuable than I can imagine and adequately describe. Dr. Hemmer's expertise and suggestions have been indispensable to me. Without Dr. Hemmer's backing, kindly patronage, and timely directing my research would never have taken place. I would like to take the opportunity to thank Dr. M. Suhail Zubairy for his kindness, keen insight, and advice that have enlightened my research path. Also, I'm very thankful to Dr. Alexei Sokolov and Dr. Aleksei Zheltikov for their teaching and wise comments.

I would also like to express my deep appreciation to Dr. R. Mohan Sankaran, Department of Chemical and Biomolecular Engineering at CWRU, for giving me a chance to work in his labs. While I was working under his supervision, I had excellent opportunities to discuss our experimental subject which has served to sharpen my thoughts. I gratefully acknowledge the support and the funding that I have directly received from Dr. Arfaan Rampersaud. His care is greatly appreciated. My heartfelt gratitude to Dr. Johnathan Cole, who I was working with at CWRU, for his gentleness and

valuable aid. During my stay in Cleveland, OH, John shared his extensive knowledge and skill.

I also express my profound sense of gratitude to Fahad S. Alghannam for his irreplaceable assistance. Our daily discussions in the lab were very constructive and contribute immensely to overcoming some issues. Furthermore, I would also want to thank Masfer H. Al-Kahtani and Saeed M. Asiri for their encouragement and help.

Finally, my family in the US and Saudi Arabia have always inspired me. I'm very grateful to my wife Hend and my children who have made my life warm and colorful.

CONTRIBUTORS AND FUNDING SOURCES

Contributors

This work was supported by the dissertation committee consisting of Professor Philip R. Hemmer [Department of Electrical and Computer Engineering], Professor Alexei V. Sokolov, Professor M. Suhail Zubairy, and Professor Aleksei M. Zheltikov [Department of Physics and Astronomy].

When the student was taking the Curricular Practical Training (CPT) at CWRU, Capacitively coupled RF plasma discharge experiments were carried out by the student under supervision of Professor R. Mohan Sankaran [Department of Chemical and Biomolecular Engineering at CWRU] in his lab with help of Dr. Johnathan Cole. Furthermore, Transmission electron microscopy (TEM) images and the optical measurements were performed by the student and Dr. Johnathan Cole at CWRU.

The TEM images of the MW plasma discharge samples and some of the optical measurements were performed at Texas A&M University by Fahad S. Alghannam. All other work conducted for the dissertation was completed by the student independently.

Funding Sources

Graduate study was supported by a scholarship from King Abdulaziz City for Science and Technology (KACST).

Dr. Arfaan Rampersaud [Columbus Nanoworks, Inc.] funded the student’s CPT at CWRU between May 16, 2016 and May 15, 2017.

NOMENCLATURE

ND	Nanodiamond
FND	Fluorescent Nanodiamond
NCD	Nanocrystalline Diamond
UNCD	Ultra-nanocrystalline Diamond
HPHT	High-Pressure High Temperature
TNT	Trinitrotoluene (or more precisely 2,4,6-trinitrotoluene). It's chemical formula $C_6H_2(NO_2)_3CH_3$.
DND	Detonation Nanodiamond
CVD	Chemical Vapor Deposition
HFCVD	Hot Filament assisted Chemical Vapor Deposition
PECVD	Plasma-Enhanced Chemical Vapor Deposition
LP-PLA	Liquid Phase Pulse Laser Ablation
QD	Quantum Dot
MEMS	Microelectromechanical Systems
UNCD-MEMS	Ultrananocrystalline Diamond Microelectromechanical Systems
MEMS MMAs	Microelectromechanical Systems Moving Mechanical Assemblies
ODMR	Optically Detected Magnetic Resonance
OES	Optical Emission Spectroscopy
CCD	Charge-Coupled Device
MFC	Mass Flow Controller

TABLE OF CONTENTS

Page

LIST OF FIGURES

Page

LIST OF TABLES

Page

1. INTRODUCTION AND MOTIVATIONS

1.1. Conceptual framework

Nanodiamonds (NDs) possess unique optical, mechanical, and thermal properties. These outstanding physical and chemical properties have opened wide windows for new researchers' activities and have inspired scientists to improve the quality of NDs and diamond film. For example, NDs are an ideal tool for many applications in the biomedical field due to their ultra-low toxicity, for instance drug delivery, bioimaging, and antibacterial applications [1-3], In addition there are nonbiological applications in industrial areas [4] like ND lubricant additives, and ND–polymer composite materials.

There are several techniques or methods to form diamonds, micro-diamonds, and NDs. High-Pressure High Temperature (HPHT) growth can produce nanodiamonds by direct growth, though this technique is not widely used. A more common approach to producing nanocrystalline diamond particles is milling of larger natural or synthetic micro-diamonds and sorting out the smaller fragment by screening out and fractionated centrifugation [5, 6].

Another popular method to grow NDs is to use the high-pressure shock wave generated in TNT detonation. This method produces very small NDs with typical sizes of 5nm in diameter, that are predominantly called detonation ND (DND). DNDs were first fabricated in the early 60's [7] and soon become widely used. Recently, another shock-wave technique, liquid phase pulse laser ablation (LP-PLA) has been used to grow nanocrystals diamonds that are <100nm in diameter [8].

Chemical Vapor Deposition (CVD) has become well-established to manufacture nanodiamond films ranging in grain size from ultra-nanocrystalline to microcrystalline films [9]. Low-pressure plasma discharges (i.e., microwave, RF, and DC glow discharges), hot filament-assisted chemical vapor deposition (HFCVD), and plasma-enhanced chemical vapor deposition (PECVD) are so-called "thermal" plasma methods which are now extensively used in synthesizing diamond films [10].

Recently, dispersed nanodiamonds have been grown in a DC micro-plasma discharge. These NDs ranging from 3 to 5nm were grown from ethanol (C_2H_6O) vapor at near-ambient (temperature and pressure) conditions [11].

Several studies have reported the enhancement of nucleation of nanodiamond films by using a nanodiamond as a seed in gas phases in a hot filament assisted chemical vapor deposition [12]. Recent studies have demonstrated nucleation of diamonds using the adamantane, a molecule resembling a single lattice unit of diamond, in glycol chemical solutions [13] and adamantane-coated sapphire substrate [14] in Chemical Vapor Deposition. One of the groups mentioned that they succeeded in using adamantane to form nanodiamonds in the gas phase by applying Microwave (MW) plasma discharge.

Fabrication of nanodiamonds using the existing methods have various disadvantages that have encouraged us to propose new techniques. The problems with previous methods can be summarized as follows:

- Poor crystal quality.
- Low chemical purity.
- Surface defects and graphitization (for DND).

- Agglomeration and formation of clusters (for Liquid Phase Pulse Laser Ablation)
- Low efficiency 10% graphite-to-diamond conversion [4–5 nm] (ultrasound cavitation).
- Contamination with beads material and generation of graphitic layers on the nanodiamond surface [Milling Methods].
- Fused nanoparticles (flow CVD [11])

Therefore, we have focused on new plasma-based techniques, especially for flowing vapor, to address these problems.

1.2. Diamond and graphite

It is appropriate to point out here the variation between the three types of natural allotropes of carbon. Structure and bond types of the atoms are the main areas of differentiation between these species. Amorphous carbon (also sometimes named diamond-like carbon [DLC]) doesn't have any crystalline structure. In amorphous carbon, a mixture of sp^2 and sp^3 hybridized bonds are presented. Diamond-like carbon exhibits some of the physical properties of diamonds such as wear resistance and hardness. Graphite, another allotrope of carbon, has pure sp^2 hybridized bonds (see Figure 1 a). It consists of layers where the carbon atoms, in each one of these layers, are arranged in a honeycomb lattice structure. The third type of allotropes of carbon is a diamond which consists of purely sp^3 hybridized bonds and has a crystalline lattice structure (see Figure 1 b). One of the prime aims in chemical cleaning is to remove the graphite and the amorphous carbon.

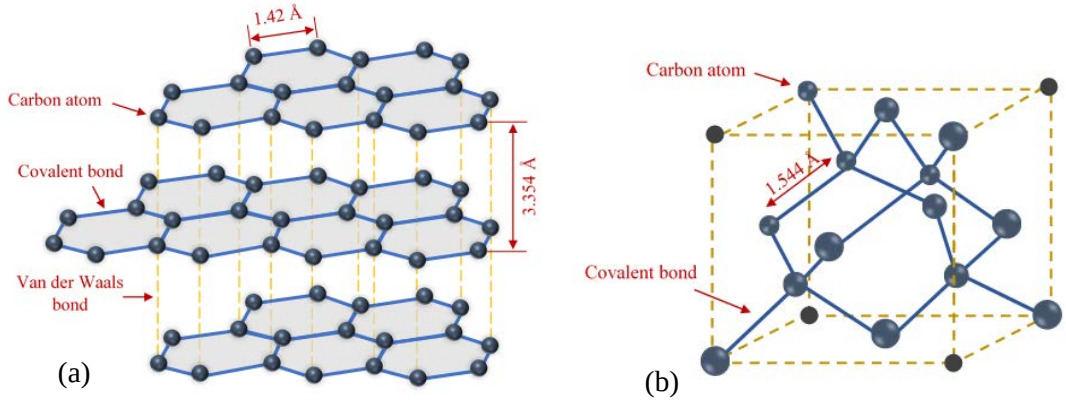

Figure 1: Crystal structure and lattice spacing of graphite (a) and diamond (b).

1.3. Properties and uses of diamond and fluorescent diamond

Diamonds possess a number of features over other nanoparticles which make them preferable candidates to utilize in many fields. To be specific, let us take a short glimpse of some physical and chemical properties of diamond and some representative applications.

I. Atomic density: since each carbon atom in a diamond is attached to four atoms (tetrahedral arrangement) with bonds 1.544 Å in length, a diamond crystal manifests the high atomic density which is 1.77×10^{23} cm^{-3}.

II. Hardness and strength: diamonds exhibit the highest hardness value on the Mohs scale (10) of any known natural material [in Vickers hardness the value is10000 $kgf/mm^2 \approx 98$ GPa]. The high strength of a diamond results from two reasons: bond energy between carbon-carbon atoms is ~ 347 kJ/mol and the directionality of the C-C-C bond, where the C-C-C bond angle is 109.5° [15].

III. Corrosion resistance: due to the chemical inertness of the diamond for the majority of acids and alkalis and its mechanical properties, it is highly resistant to corrosion [16, 17]. However, at high temperatures (over 480 °C) in the presence of oxygen [18] the ND will be etched.

IV. Thermal conductivity: diamond has high thermal conductivity (2200 $W \cdot [m \cdot K]^{-1}$) which is higher than all metals such as copper (401 $W \cdot [m \cdot K]^{-1}$), sliver (429 $W \cdot [m \cdot K]^{-1}$), gold (317 $W \cdot [m \cdot K]^{-1}$), and aluminum (237 $W \cdot [m \cdot K]^{-1}$). Thus, it has been used with semiconducting materials to prevent overheating. [19]

V. Electrical conductivity: diamond, such as IIa type which is entirely devoid of impurities, has the highest electrical resistivity of all material (10^{14} $\Omega \cdot m$). It is preferable here to mention that the method of classifying diamonds depends on the level and type of their chemical impurities. Diamond semi-conductivity is induced by impurity doping, for example, using a very low level of boron impurity (1ppm) is enough to give the diamond electrical properties. This type of diamond is named IIb type (see Table 1).

Properties	3C-SiC	Diamond	Graphite
Hardness (Mohs scale)	9.6	10	1 – 2
Thermal conductivity [W/ (m. K)]	490	2200	398
Density (g/cm3)	3.21	3.5	2.26
Thermal expansion coefficient [α: ($\times 10^{-6}$ C^{-1})]	4.0	3.8	1.8
Semiconductor	✓	Type IIb, is p-type semiconductors (Boron impurity doping)	× (Conductor)
Bandgap [eV]	2.36	5.47	-0.04

Table 1: Some of the diamond properties comparing with silicon carbide (3C-SiC) and graphite at room temperature. [19]

VI. Photostability: fluorescent NDs (FNDs) are photostable for a very long time with continuous excitation, and there is no drastic decrease (or blinking) in the recorded photoluminescence intensity with time [20]. In contrast, when using a dye or fluorophore molecules under continued excitation, fading (photobleaching) or disappearing of fluorescence will occur after a short time [21]. Quantum dots (semiconductor nanoparticles) (QD) also do not bleach but photoluminescence intermittency or blinking will occur. The emission of light by these QD nanocrystals will switch between bright (ON) or dark (OFF) states [22, 23]. For this reason, scientists in different fields, especially biologists, have chosen FNDs to facilitate some of the fluorescent measurements, e.g., imaging, in living cell [24]. For

example, FNDs have been applied to facilitate optical tracking, imaging, and studying living cells *in vivo* and *in vitro* environments.

VII. Toxicity: FNDs are highly inert chemically which leads to low toxicity and high biocompatibility. Several groups have studied the toxicity of fluorescent nanodiamonds on biological functions of organelles, proteins, and cells. The relation between the viability of the cells vs. the dosages showed favorable results for all but exceptionally high doses, beyond those used in most biological applications [25-28]. From this it is clear why researchers focus on utilizing the FNDs in biological applications such as potential drug delivery.

1.4. Functionalization of nanodiamond

Functionalization is one of the keys to employing NDs for specific applications. The chemical treatment of NDs is required to modify their surfaces for targeted applications. Figure 2 shows some of the functional groups that can be bonded to NDs' surface.

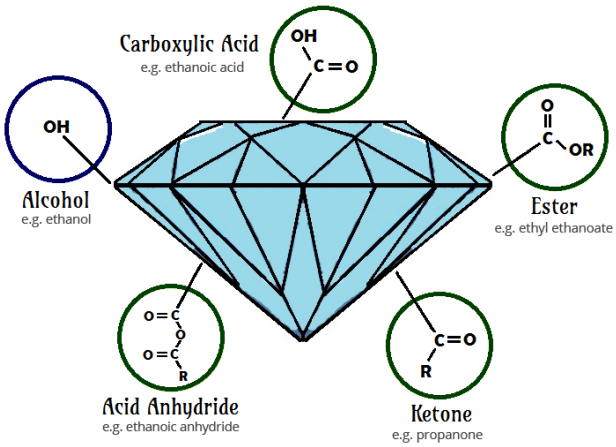

Figure 2: Variety of functional groups that can be conjugated with NDs' surface.

1.5. Applications of nanodiamonds

1.5.1. DNA and antibody integration with diamond

Yang, W. S. *et al.* [29] have claimed that thin film of nanocrystalline diamonds can be used as an extremely stable substrate for eclectic biological modification. Using diamond as an interface, they integrated the DNA and other biological material with microelectronics to develop integrated bioelectronic sensing systems and signal processing. In this experiment, they connected diamonds with hydrogen surface termination to a long-chain ω-unsaturated amine, omega-Decenylamine ($C_{10}H_{21}N$). This primary amine, after some chemical processes as illustrated in Figure 3, was then reacted with thiol-modified DNA. The final product was a very stable DNA-modified nanocrystalline diamond surface that performed well compare to DNA-modified gold, silicon, and glassy carbon surfaces that have been used in this study as well.

The noteworthy capability of easily monitoring and tailoring NDs' surface chemistry is the advantage that Bradac, C., *et al.* [30] have used in their work. In this work, fluorescent nanodiamonds (FNDs) (~ 30 nm in size) have been coupled to protein filaments of actin (F-actin, for "filamentous actin") with a range in length of 3-7 μm. This is accomplished starting with carboxylated fluorescent nanodiamonds that have been mixed with a carboxyl activating agent (EDAC = "1-ethyl-3-(3-dimethylaminopropyl) carbodiimide hydrochloride") and then with Sulfo-NHS (N-hydroxysulfosuccinimide) to convert the carboxyl groups to amine-reactive NHS esters which produce a FND Sulfo-NHS ester intermediate. Finally, for bioconjugation, an amine functional group on the target actin filament was tied to the functionalized FNDs to produce a FND-protein

complex that has a stable bond. Figure 4 displayed the chemical processes that have been explained previously. Relying on the self-assembling capabilities of biological systems, manufacturing hybrid FND-biological quantum devices have been discussed and demonstrated where the proteins structure act as a structural scaffold for surface functionalized FNDs [31].

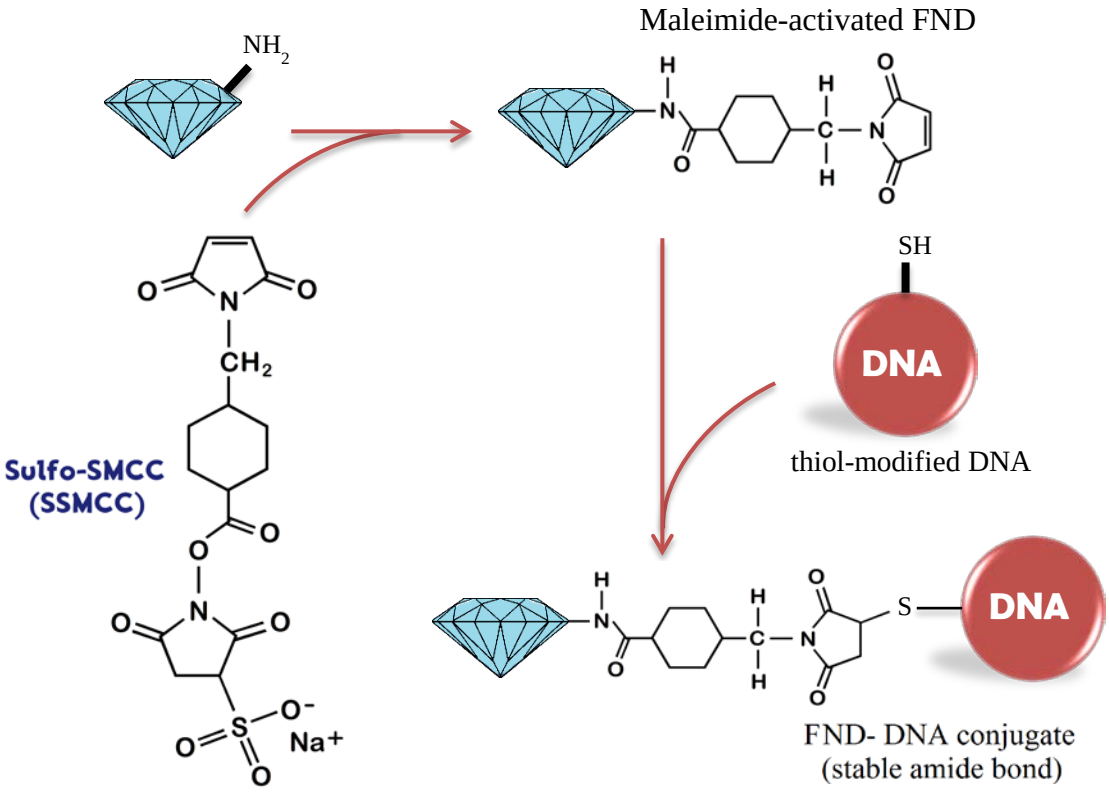

Figure 3: Schematic of fluorescent nanodiamonds - DNA conjugation.

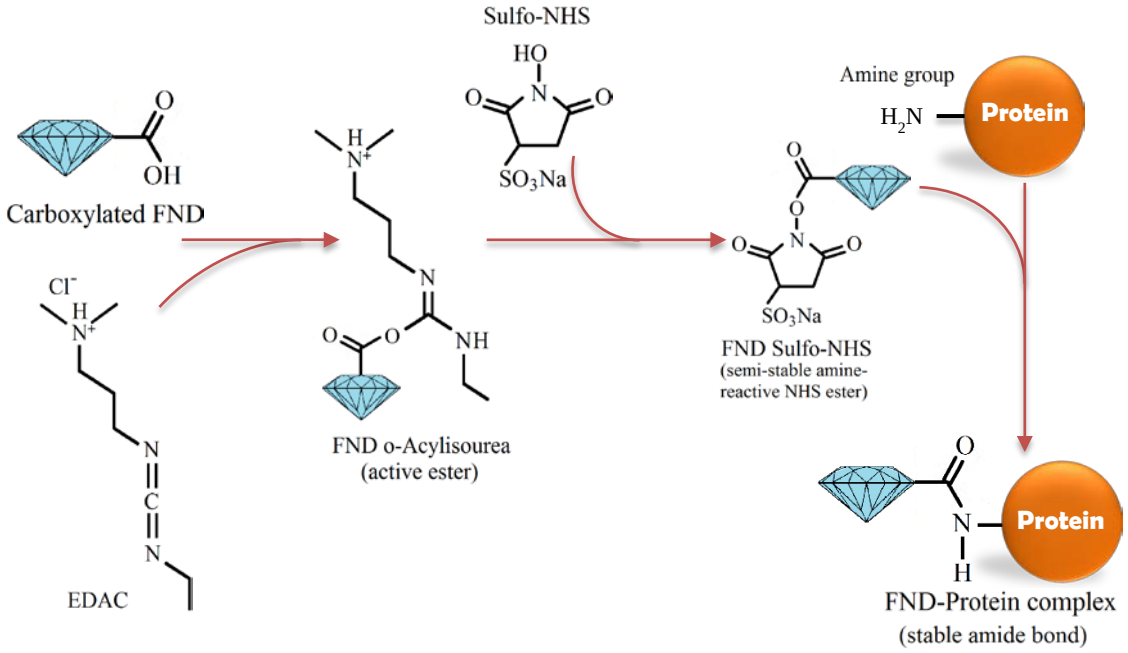

Figure 4: The chemicals processes to couple FND with F-actin.

1.5.2. Diamond-based medical devices

K. Jozwik and A. Karczemska [32] designed an artificial heart valve ring coated with nanocrystalline diamond (NCD). The studied valve was tested with constant operation over a period of 14 months, where the number of cycles (heartbeats) throughout the exertion operation period was 1000 cycles/min. This was estimated to be equal to 17.5 years of operation in an artificial heart valve inside the human body. The surface and the thickness of the NCD layer after a long test of mechanical fatigue is in the same range as before the examination.

Amaral, M., *et al*. [33] have used a coated Si_3N_4–bioglass composite with nanocrystalline diamond (NCD) in their experiment. The tribomechanical properties of

NCDs such as friction response were studied to determine how to utilize them with *in vivo* hip and knee joint implants. The first tests were ball-on-disc friction and wear. The contact stresses values were in the range 100-300 MPa, which is greater than the nominal contact pressures generally used in tribotesting of artificial hip and knee joints. Further, in pin-on-disc tests tribological experiments the contact stresses of 25 MPa were employed for up to 5×10^5 cycles. In the human body and at perfect functioning, the typical friction coefficients of hip joints are in the range 0.025-0.05. The measured values of the friction coefficients in this experiment were 0.01–0.02. From the results of the previous two studies (i.e. Refs [32] and [33]), it is concluded that coating the bio-parts with diamond gives better performance and is more durable than alternate materials.

Biomedical microelectromechanical systems (MEMS) are microscale devices (<100 μm) that are fabricated with different material like ceramic, Si, or metals using deposition and pattering techniques. They are currently and mainly manufactured using silicon-based technology. However, Si exhibits unfavorable tribological and mechanical properties, including imperfect fracture resistance, bend strength, and the tendency of adhering to wet surfaces. A.R. Krauss *et al.* [34] have developed a new lithographic technique for the construction of ultrananocrystalline diamond microelectromechanical systems (UNCD-MEMS). The exceptional properties of diamonds compared with Si, SiC, such as hardness, mechanical strength, chemical inertness, and thermal stability make it an incomparable candidate material for microscale devices that can be used, for instance, for sensing or drug delivery. The projected wear life of a diamond MEMS device is 10,000 times more than that of Si, which makes, in principle, the diamond

microelectromechanical systems (MEMS) is an exemplary device for replacing the Si MEMS.

1.5.3. Magnetic sensing

Hegyi, A. and E. Yablonovitch [35] have utilized optically detected electron spin resonance (ESR) mechanism to measure the nitrogen-vacancy (NV) color center fluorescence in 100 nm sized nanodiamonds (NDs), which have been planted inside a small piece of chicken breast. Different shapes of phantoms have been made out of a double-sticky tape covered with a 3.75 μg mm^{-2} area density of NDs and put between two optical sealing tapes. Then they were positioned inside the tissue at 5 mm back from the surface facing a light-emitting diode (LED). Nitrogen-vacancy centers inside scattering tissue were optically excited by the red LED at wavelength 610−630 nm. To make image, a B-field-sample stage has four permanent magnets, which are connected and organized to generate a field-free point. To define the location of this point, especially its distance from the NDs point inside the tissue, a raster scan pattern technique was applied to the field-free point using additional electromagnet coils. When microwaves were employed, the fluorescence was decreased by an amount that's proportional to the concentration of the NDs at the field-free point. Using this technique, the achieved sensitivity and the spatial resolution were, respectively, 740 pg of ND and 800 μm over a 1 cm^2 field of view after 100 second of measurement time.

The optically detected magnetic resonance (ODMR), Rabi cycling, and spin-echo of single fluorescent nanodiamond (FND) nitrogen-vacancy (NV^-) color centers placed into living human HeLa cells were elucidated by McGuinness, L.P., *et al.* [36]. FNDs with

an average size of 45 nm were utilized and diluted in a medium with 20 μg ml^{-1} of concentration, and then the HeLa cells were cultured in this medium. This work, as well, has reported that the integration of high-accuracy fluorescent tracing and quantum monitoring is harmonious with cells viabilities. With nanoscale exactness several types of measurements have been done, e.g., spin coherence times (T_2), and location of FND.

1.5.4. Temperature sensing

At temperatures ranging between 5.6 K and 295 K, Chen, X.-D., *et al.* [37] have measured optically detected magnetic resonance (ODMR) and photoluminescence of NV color centers. Below 100 K, NV centers have a higher frequency stability and performance due to the transition energies drifting less. Both zero-field splitting (ZFS) *D* and zero phonon line (ZPL) energies have nonlinear relationships with temperature, and they tend to change more slowly with temperature at low temperatures. Furthermore, the dependency (i.e., temperature with ZFS and ZPL) has been observed for various charge states. Figures 1 (b) and 3 (a), in Ref. [37], distinctly showed that ZFS [*D(T)*] and ZPL both decrease by increasing the temperature. After comparing the energy shifts of ZFS with ZPL lines with temperature for NVs in the negative charge state, they found the shapes of these two lines corresponded very well (see Figure 3 (a) in Ref. [37]).

Temperature dependence of the magnetic resonance (MR) spectra of NV^- color centers ensembles, at different concentrations, was studied by Acosta, V.M., *et al.* [38] with temperatures ranging from 280 K to 330 K. Diamonds with NV^- ensembles concentration in the range of 0.3 – 16 ppm was utilized. The temperature dependence of

axial (D) and transverse (E) ZFS parameters for the samples were dD/dT = 74.2(7) kHz/K and $dE/(EdT)$ = 1.4(3) $\times 10^{-4}$ K^{-1} respectively. At the magnetic field ≤ 1G and when the temperature was increased, both ZFS parameter D and the amplitude of the peaks decreased.

Kucsko, G., *et al*. [39] have evolved a new nanometer-scale thermometry technique to measure the temperature changes in a living cell (human embryonic fibroblast WS1 cell) by NV^- in nanodiamond. NDs and gold nanoparticles (NP) with ~100 nm in size injected into a living cell. Two 532 nm green lasers were used, where one of them was for heating up the gold NPs and the other for exciting the NDs. A confocal microscope was equipped with an XY scan to collect the fluorescence and then generate an XY illumination map. Temperature changes were measured at positions of two different NV color centers at different distances from the heated gold NP. The precision of this nanometer-scale thermometry (i.e., NV^-) sensor was appraised to be δT = 44 ± 10 mK. The computed temperature change agreed with the steady-state solution of the heat equation. The altering in temperature [$\Delta T(r)$] was proportional to $1/r$, where r was the distance between the NDs and the gold NP.

Relying on an optically detected electron spin resonance (ODESR) mechanism, nanoscale temperature sensing using a single negatively charged nitrogen-vacancy (NV^-) color center in diamond was demonstrated by Neumann, P., *et al.* [40]. In either bulk diamond or NDs, a single NV^- color center was probed via optical excitation and photoemission collection. A microstructure with loop-gap resonator (LGR) at a resonance frequency of ≈1.8 GHz which can be excited from a distance by RF radiation were

engineered on a glass coverslip. NDs of ~50 nm in average size, containing NV^- defects, were placed on the top of the coverslip. There was an association relationship between the temperature changes of NDs and the RF that was applied to excite the resonator. A single NV nanoscale thermometer in a bulk diamond was used to measure the temperature shift due to the heating by the microstructure. Temperature accuracy down to 1 mK was achieved, and improved efficiency of the photon collection will raise the temperature sensitivity.

1.5.5. Drug delivery

Based on the chemical inertness and the exceptional optical properties of FNDs, much research has exploited the NDs to serve as biocompatible drug carriers. Doxorubicin, an anticancer chemotherapy medication, was conjugated to nanodiamonds, and then the resulting ND-Dox complex was used for malignant brain tumor treatments *in vivo* and *in vitro* by Xi, G., *et al.* [41]. Convection-enhanced delivery (CED), which is a therapeutic strategy, was utilized to administer an ND-Dox complex into malignant gliomas. To understand the efficacy of utilizing ND-Dox in the treatment, drug retention, uptake, toxicity, and cell viabilities (i.e., MTS assay) were investigated for different cell lines (see, e.g., Fig. 1 c & f in the Ref. [41] and Figs. 6 & 7 in its supplementary information). After 72 h, the ND-Dox complex, which was delivered via CED, significantly impeded proliferation, boosted apoptosis, and increased DOX retention and localized the DOX toxicity in the brain glioma cells more than unmodified DOX. Figures

5 and 6, respectively, show two scenarios of delivery of DOX without and with NDs conjugation.

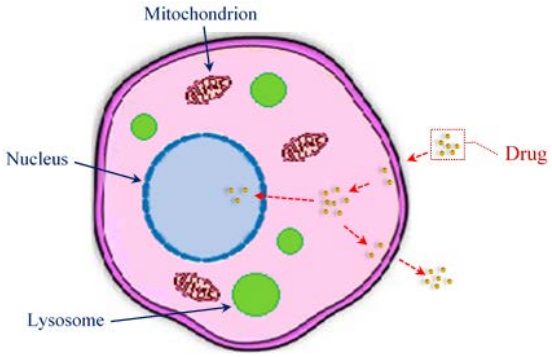

Figure 5: DOX delivery scenario into the cells without NDs.

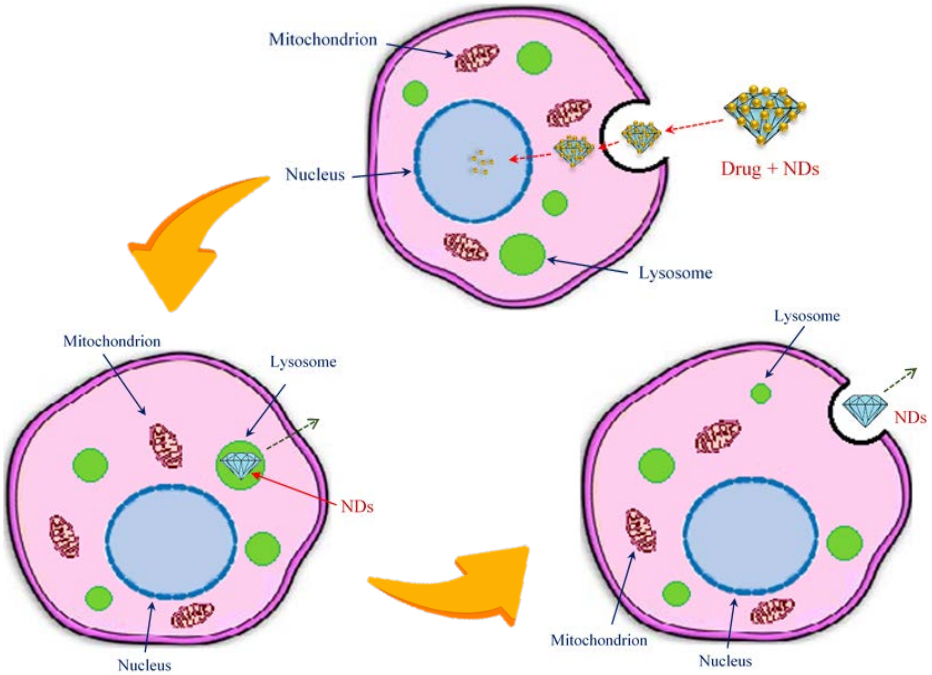

Figure 6: Schematic presentation of ND-DOX complex delivery into the cells.

1.5.6. Nanodiamond and lubrication

The remarkable tribological properties of nanodiamond have motivated the scientists to use the NDs as additives to lubricants when studying the lubrication of interacting surfaces moving relative to each other. The NDs improve oil performance by reducing the friction coefficient 20-40% more than oil without NDs, and oil/surface temperature will decrease between 16-20%. Rounded NDs particles within the oil enhance the hydrodynamic lubrication and act as nanoscale ball-bearings between moving surfaces which converts the sliding friction of contacting surfaces to rolling friction. Oil/NDs lubricant also reduces fuel consumption by ~ 6 %, making engines last longer, and extending the tools lives by a factor of 1.5-4.0 times [42, 43].

1.6. Existing mass production and growth methods of NDs

The common techniques for NDs mass production are milling of high pressure high temperature (HPHT), chemical vapor deposition (CVD) diamond, and detonation of graphite mixed with an oxygen deficient explosive mixture of TNT/RDX. The output of crushing (milling) HPHT diamonds results in diversity of sizes from micrometer to a few nanometers in size. Rough edges, a high degree of polydispersity (diameters ranging), and contamination from the bead material are some issues found in this mechanism. The detonation approach to mass-produce nanodiamonds (DNDs) has some problems, as well, relating to, for instance, agglomeration, chemical impurities on surface, and surface termination defects (like sp^2 defects on the surface) (see Figure 7). Detonation conditions such as carbon sources concentration, pressure, and temperature have a great impact on

the quality of nanodiamonds. Figure 8 demonstrates the detonation approach, and there is a photo of the raw soot (detonation nanodiamonds before treatment). It is imperative in this regard to point out that both milling and detonation, as mass-produced techniques, yield ultra-small NDs (~5 nm in size), and many of the produced detonation nanodiamonds (DNDs) have a high quantity of nitrogen impurity.

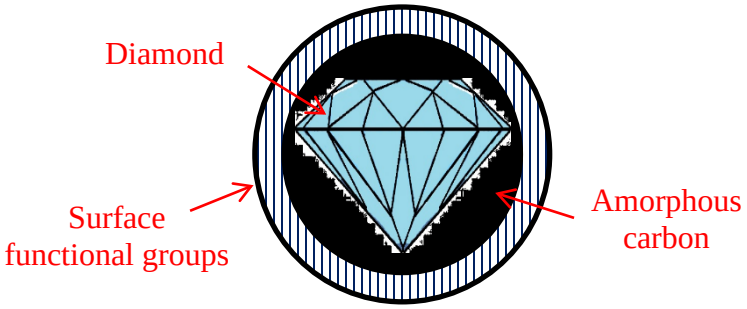

Figure 7: Structure of detonation of nanodiamonds (soot).

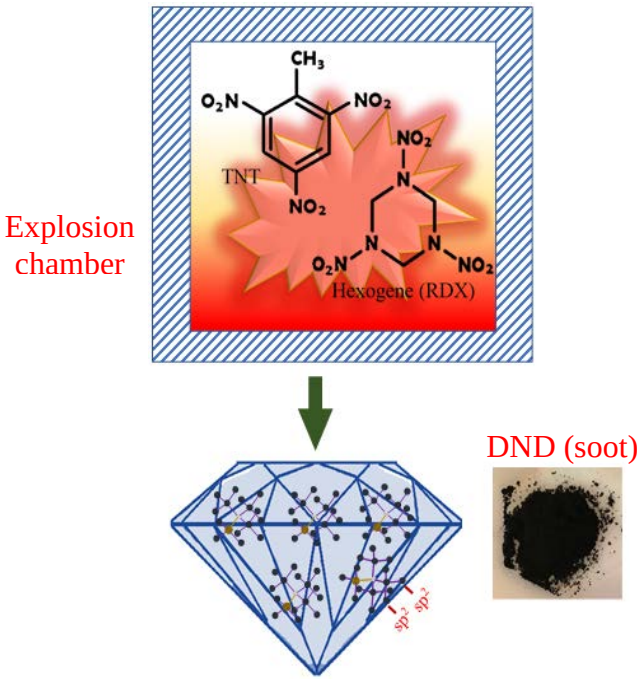

Figure 8: Detonation nanodiamonds technique.

In the chemical vapor deposition (CVD) mechanism a variety of hydrocarbon compounds (e.g., CH_4, CH_3COCH_3) which have both low and high molecular weight can act as a carbon source. For CVD growth there will sometimes be additives that are non-hydrocarbon components such as oxygen, nitrogen, and silicon. Conventional CVD is a very slow growth process, and in some cases, requires plasma discharges to enhance the NDS nucleation (PECVD for "plasma-enhanced chemical vapor deposition"). CVD diamonds need substrates to grow on. For example, to grow or manufacture high purity and single crystal, the substrate should be a diamond or iridium, whereas a silicon substrate has been used to produce diamond with lower thermal stress property. CVD has been vastly applied to form thin films with nanocrystalline and ultrananocrystalline grain sizes. Figure 9 presents the basic principle of NDs formation via CVD growth technique. To

overcome the sp^2 bonds that form during growth, an abundance of hydrogen is provided to etch sp^2 bonds. Other methods such as dispersed NDs growth on a surface via CVD, dispersed ND growth without a surface via flowing plasma, and ultra-small NDs growth in a flowing plasma will be discussed in detail in Chapter 3.

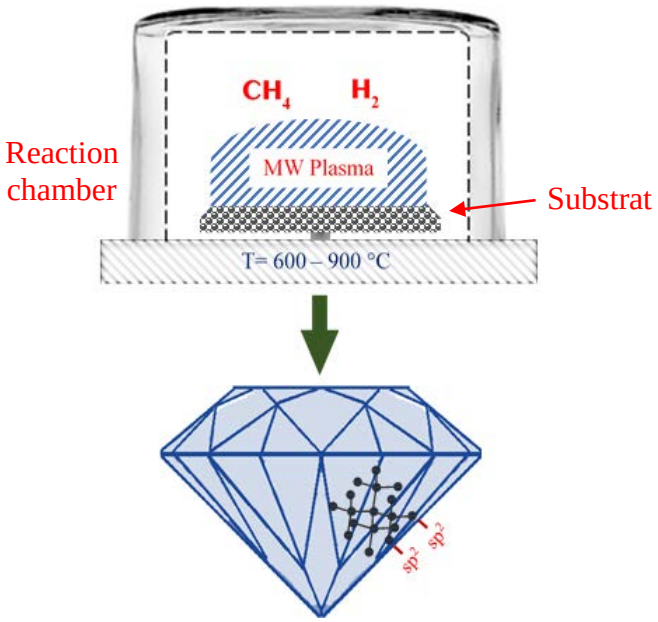

Figure 9: The conceptual design of chemical vapor deposition.

1.7. Problems with existing NDs.

From the prior discussion, the problems with the existing nanodiamonds are summarized in the list below. They are divided based on the applications of NDs.

- **Magnetic and temperature sensing.**
    - *Surface defect and termination*: except for termination with hydrogen, the diamond surface will have an incomplete coverage. Thus, the dangling

bonds create surface radicals and subsurface damage also forms radicals and these degrade magnetic sensitivity.

- *Probabilistic placement*: radicals or sp^2 defects on the NDs surface act as charge traps which leads to quenching the NV^- color center luminesce. When the negatively charged nitrogen-vacancy color center is close to the surface then the electron might escape from the vacancy and bond with the radical. The NV^- color center will then be converted to a neutral nitrogen vacancy center (NV^0). For this reason, the nitrogen-vacancy color center should be in the center of a nanodiamond. This goal is a challenge that hasn't been reached yet.

- **Toxicity:**
  - *Surface graphitization*: surface chemistry (or surface functionalization) of NDs by hydrogen suppresses surface graphitization. But oxygen-containing functional groups confer charge stability to NV^-. These are conflicting requirements. Unlike pure nanodiamonds, raw DND can be toxic before further chemical treatments and cleaning or air oxidation.

- **Biolabeling**:
  - *Polydispersion*: means there is no consistency in NDs sizes (you can find 5 nm and find 200 nm). In the bio-applications, ultrananocrystalline nanodiamonds less than 8 nm in size are required. This is because the threshold of the pore size in the human kidney filtration system is between 6-8 nm. Thus, the size of the utilizing NDs as drug delivery agents inside

the human body must be in this range so the NDs can pass through the kidney filtration system and be expelled in the urine.

- *Agglomeration*: conglomerated NDs cannot be useful and must be dispersed. Heating, sonication, and centrifugation NDs are some of the techniques that have been broadly used for producing dispersing NDs.
- *Rough edge*: regardless of the NDs' surface chemistry, size, or composition, prickly NDs might pierce the endosomes' membrane and then stay in the cytoplasm for a long time. Sharp-shaped NDs have been shown to pierce the lysosome. If this occurs during the late stage, waste escapes to the cytoplasm and poisons the cell [44].

2. LITERATURE REVIEW

2.1. Non-seeded growth

All the attempts to nucleate nanodiamonds in the vapor phase used compounds such as hydrocarbons as a source of carbon. An example of such carbons source or fuels are methane, ethanol, dichloromethane, and chloroform. Reactor pressure, power, gases volumetric flow rates, and residence time are significant and effective constituents which control the fabricated particles properties. Spitsyn, B. V. *et al.* [45] have studied the vapor growth of diamonds on diamond and nondiamond surfaces. Nanocrystals of diamonds were grown on nondiamond substrates including silicon, molybdenum, copper, tungsten, gold, silica, graphite, tantalum, aluminum nitride, and sapphire [46]. On the carbide-forming substrates such as Si, the nucleation rate of the diamond was higher by one to two orders of magnitude more than non-carbide-forming substrates. Spitsyn, B. V. *et al.* claimed that the substrate temperature is an important factor which affects the diamond's crystal (i.e., single-crystalline or polycrystalline) and nucleation rate. When the substrate temperature, for instance, was 600°C a polycrystalline diamond was formed whereas a single-crystalline was formed at 750°C. The homoepitaxial diamond films growth rate was increased by raising the temperature where the maximum was reached at about 1μm/h at 1000°C. As a result of increasing the temperature further, the structure of the diamond layers is deteriorated and the growth rate is reduced.

Shapes of deposited diamonds tend to transfer from polyhedron to hemispherical with increasing methane concentrations. When a lower methane concentration was

applied, particles with crystallographic planes such as (111) and (100) were found (where [Miller indices, *hkl*] describe the crystal orientation). In other words, high-quality diamonds were deposited at lower methane concentrations, and both Raman and cathodoluminescence spectra of diamond particles have confirmed this result [46].

2.1.1. Hot filament technique

Wei, J. and Y. Tzeng, [47] have evolved a sequential deposition and etching procedure to grow high quality diamonds via a hot-filament CVD technique. In the sequential deposition, a methane-hydrogen mixture was applied, whereas the hydrogen by itself was harnessed for etching nondiamond components. The substrates in the experiments were silicon wafers which were polished with diamond paste before the depositions. In the precipitation process or cycle, the ratio of CH_4/H_2 was 3.1 %. While in the etching cycle, 100% of H_2 was applied, namely there was no CH_4 introduced in the chamber. The rest of the conditions were: chamber pressure, 50 Torr; substrate temperature, 600 to 1000°C; filament temperature, 2100- 2400°C. At a suitable ratio of deposition and etch temperatures near 1:1 (T_D:T_E), high growth rate and high-quality diamonds were produced. There was strong dependence between the diamond films' crystallite sizes and the cycling time of deposition (T_D) and etching (T_E). At the same settings conditions, making continuous diamond sedimentation instead of deposition-etching process was decreased the growth rate by 2.5 times.

Seiichiro, M. *et al.* [48] study was one of the first experiments constructing nanodiamonds from the gas phase using the hot-filament CVD technique. They used a

CH_4 and H_2 mixture with low volumetric flow rate around 10 sccm. The other conditions were pressure, 10-100 Torr; substrate temperature, 800-100°C; filament temperature, 2000°C. The measured Raman fingerprint was slightly different from single crystal natural and HPHT synthesized diamonds. They claimed that the difference was caused by internal strain and structural imperfections.

Matsumoto, S., *et al.* [49] reported growing diamonds from methane-hydrogen gas on diverse non-diamond substrates at various temperatures and CH_4-H_2 concentrations using a hot filament. Typical deposition conditions of their work were as follows: heating temperature, 700-1000° C, total gas pressure 10-l00Torr, methane concentration 1 %, filament temperature 2000° C, and reaction time 3 h. Raising the methane concentration changed the particles from euhedral to ball-like with graphite disorder revealed in the Raman spectrum. At an appropriate methane concentration, the diamond growth rate grew with increasing temperature of the filament. Substrate material has an effect on the nucleation rate. Furthermore, the size and the crystal properties of the deposit particles were changed as a consequence of changing the reactor pressure.

2.1.2. DC plasma discharge technique

A DC plasma chemical vapor deposition technique was used by A. Sawabe *et al.* to form diamond thin films. The reactor was fed with a CH_4/H_2 mixture at 0.5 to 4 vol% ratio. The total volumetric flow rate was fixed to be 100sccm, and the reactor pressure was over 200 Torr. The conditions of the DC discharge were 1 kV, 4 A/cm^2, and the substrate temperature was over 800°C. They claimed that the nucleation density of the diamond film

was 10^8 cm^{-3} [50, 51]. At higher pressure conditions, A. Kumar *et al.* [11] presented a new manner of nucleation of NDs ranging from 3 to 5 nm using ethanol (C_2H_6O) vapor in DC micro-plasma discharge. This mechanism has shown that synthesizing NDs without substrate and with a short growth time is feasible. The manufactured NDs were collected on a filter outside of the reactor.

Using a DC plasma torch, Aoyama, K., *et al.* [52] have elucidated the effectiveness of the presence the H_2 on diamond deposition. Mixtures of Ar, CO_2, CH_4, and H_2 have been used. Both the total volumetric flow rates of the gases mixture and the pressure were fixed to be 12 *l*/m and ~ 195 Torr. The DC powers were 1.7, and 2.5 kW where the current was 90A. For an equivalent period (90 min), three types of systems (Ar-CO_2-CH_4-H_2, Ar-CO_2-H_2, and Ar-CO_2-CH_4) were examined. The characteristics of deposited diamonds in the first two systems were approximately the same. In the absence of H_2 (i.e., Ar-CO_2-CH_4), small amounts of small particles were fashioned. Reduction of the concentration of H_2 in the gas mixtures suppressed diamond nucleation and grew much more graphite and amorphous carbon. Kotaki, T., *et al.* [53] have deposited diamonds on different substrates with two types of plasma discharges. A DC plasma jet with fixed power at 2 kW was used in an Ar- CCl_4-H_2 system and the substrate was made of molybdenum sheets. The concentration of CCl_4 was 0.03 vol.% whereas H_2 was 1.7 vol.%. The values of total volumetric flow rate and total pressure, respectively, were 12 *l*/m, and ~ 100 Torr. The second gas mixture system was CCl_4-H_2. In this system, microwave discharge plasma at 100 W power was used with silicon (111) oriented and α-alumina $(10\bar{1}1)$ oriented wafer substrates. The concentration of CCl_4, the total volumetric flow rate, and the pressure were

3-6 vol.%, 40 sccm, and ~ 10 Torr respectively. The substrates' temperatures of both systems were estimated to be around 1400 K. In the CCl_4-H_2 plasma system, amorphous carbon components covered the deposited diamonds which clearly affected the diamond Raman spectra. The diamond's grain size increased by increasing the growth time.

2.1.3. Inductively and Capacitively coupled RF plasma discharge techniques

Inductively coupled radio frequency plasma-assisted chemical vapor deposition has been widely used. Seiichiro [54] employed this approach using CH_4 vol% from 0.2 to 1 in H_2 where the total volumetric flow rate was fixed to be 50sccm. The rest of the experimental conditions were: 0.5 to 3 kPa chamber pressure, 0.5 to 1 kW power, 13.56 MHz RF, and finally, the substrate temperature was 800-940°C. Seiichiro Matsumoto *et al.* [55] used the same carbon source (i.e., CH_4 as fuel) with a volumetric flow rate at 0.1-1.2 l/m. They injected the fuel in the center of Ar plasma which functioned at 60 kW and 4 MHz frequency. An Ar and H_2 sheath was used to assist in controlling quality of the diamonds. The material was grown onto substrate at a temperature between 700-1200°C.

Electrodeless capacitively coupled RF discharge technique was applied to growth by Laimer, J., *et al.* [56]. The running conditions of the experiments were: RF power, 900-1000W; CO_2 and CH_4 flow rates ratio to the total flow rate, 5%; H_2 flow rate, 200sccm; reactor pressure, from 20 to100 mbar; substrate temperature, 900-950°C. Diamond grains between 2 to 10 μm in size were deposited with several morphological types of diamond and crystal structures. The fountainhead of this diversity is the ratios of CH_4 and CO_2 to each other and the flow rate of H_2. Additionally, a black carbon coating was formed on

the inner surface of the quartz tube (i.e., reactor) which largely influenced the created materials' morphology and the deposition conditions, and consequently, the experiments become irreproducible. To overcome this issue, CO_2 was introduced with the reactants. When the CH_4 was presented in a surplus of CO_2, the diamond facets vanished. Faceted crystals were observed at ~ 0.25% CO_2 in CH_4. The design of electrodes to be outside of the reactor prevented the contamination that comes from the electrodes material reaching the depositions.

2.1.4. Microwave plasma discharge technique

T Gries *et al.* [57] used CO-H_2 and CH_4-CO_2 to synthesize nanodiamond grains ranging in 15 to 100nm at low pressure (~1.33 kPa) via a microwave plasma-assisted chemical vapor deposition (MPACVD). They fed one reactor with 35-45% CH_4-CO_2 mixture and the other with 8% with CO-H_2. This experiment used a MW frequency source at 35.2 GHz. A diamond film was created on the silicon wafer at a temperature ~350°C. Mutsuku Kamo *et al.* [58] have confirmed growing polycrystalline diamonds on a nanodiamond coated substrate at a temperature between 800 to 1000°C. The CH_4/H_2 ratio in the range 1 to 3 % was used. Additionally, this attempt was run from 1 to 8 kPa total pressure, and the MW power was between 300-700 W. The film growth rate was ~ 3μm/h as a maximum. Chen, C.-F., *et al.* [59] studied CO_2-(C_2H_2, CH_4) gas mixtures systems, with no additional hydrogen gas, to deposit diamonds using the microwave plasma CVD technique. The growth rate was higher than many of other techniques. For instance, they found that the diamond's growth rate in CH_4-CO_2 experiments was about four times more

than in the CH_4-H_2 experiments. The conditions of their experiments were: microwave power, 400W; C_2H_2 and CH_4 volumetric flow rates, from 13.7 to 15 sccm and 20,6 to 22 sccm respectively; the reactor pressure, 25 Torr; substrate temperature, 800°C. Furthermore, the crystallinity and the quality of the deposited film are comparable to natural IIa diamond type. Carbon sources (i.e., C_2H_2 and CH_4) volumetric flow rates have played important roles to increase or decrease the film growth rate. The maximum film growth rate in the CH_4-CO_2 system was when the C_2H_2 volumetric flow rate was 14 sccm 0.98 μm/h and it will decrease rapidly when rasing the volumetric flow rate higher.

M. Frenklach et al. [60] have presented evidence for the homogeneous nucleation of diamonds in a microwave plasma discharged. A variety of diluted carbon compounds, e.g., dichloromethane (CH_2Cl_2), methane, and acetylene with argon, hydrogen, or oxygen were tested. A MW generator in this study was operated at a 2.45 GHz with power from 200 to 300W. CH_2Cl_2 was the most important agent that was delivered to the reaction volume with varied volumetric flow rates at different reaction pressures. Two recipes without and with Ar shielding have been experimented with and successfully synthesized nanodiamonds under the following conditions: the first conditions were CH_2Cl_2 and O_2 where they were done at: flow rates, 120 and 100 sccm, respectively, reaction pressure, 20 Torr. The second conditions, in the presence of Ar shielding, were: flow rates of CH_2Cl_2 200-240, O_2 100-200, and Ar 300-400 sccm; pressure, 30 Torr. Samples characterizations were performed in three stages. Nondiamond materials was removed via wet chemical oxidation then the sample was heated in perchloric acid at around 180 °C. Finally, to remove the impurities such as SiO_2, the remaining material was rinsed with HCl and HF

acid solutions. Also, the same group [61] tested silane (SiH_4) and diborane (B_2H_6) with acetylene as fuel to form a diamond powder. The reactor pressure was fixed to be at 50, 100, or 200 Torr. MW power was tested in the range between 300 to 900 W, and the total volumetric flow rate of the experiments was 350sccm. A theoretical calculation has demonstrated the homogeneous formation of a diamond in the gaseous phase [62].

"Towards a general concept of diamond CVD" technique is a very good review that has been published by Bachmann, P.K., *et al*. [63]. This investigation studied more than 80 deposition experiments from over 25 studies (see Table 2). The collected data was presented in C-H-O diamond deposition phase diagram, as depicted in Figures 10 and 11, utilizing the ternary plot (sometimes termed a triangle plot or ternary diagram).

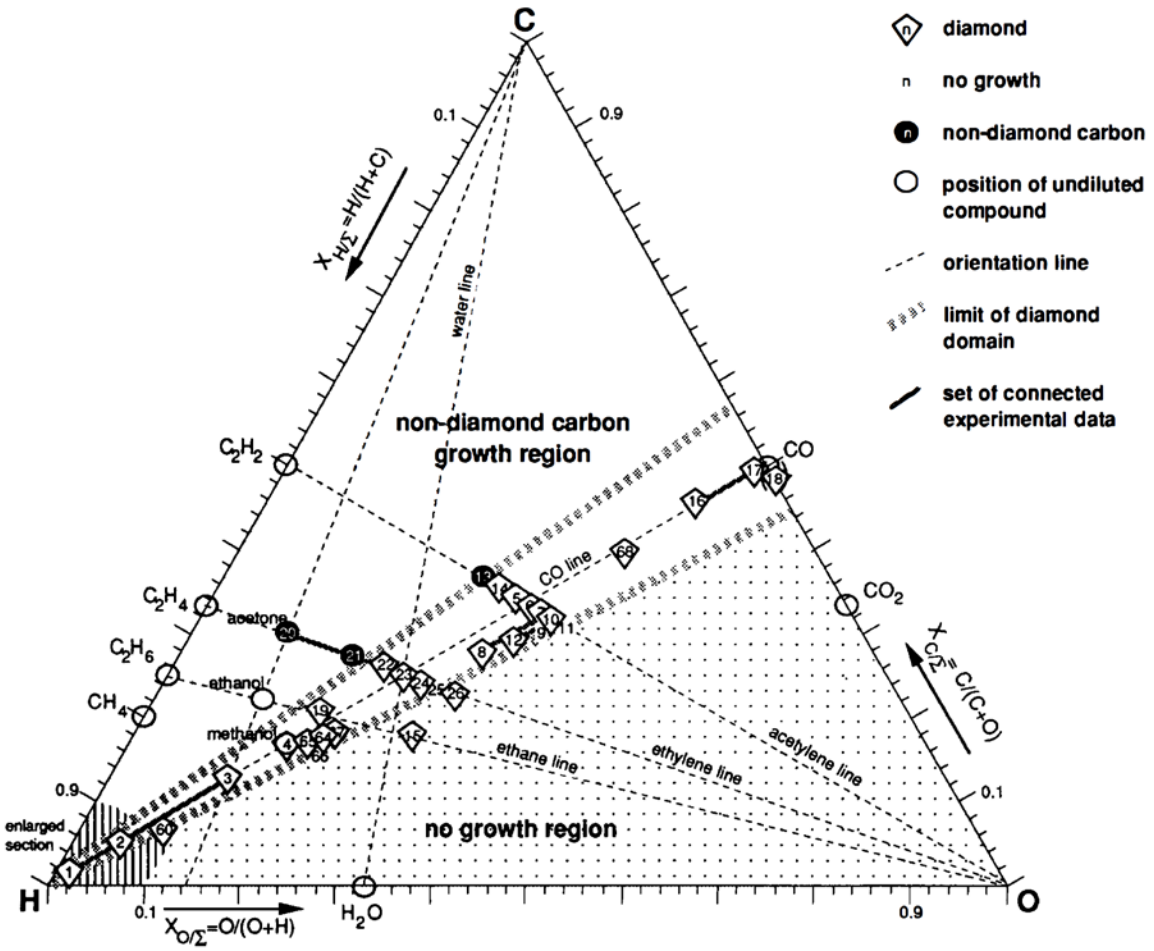

Figure 10: Atomic C-H-O diamond deposition phase diagram with the "diamond domain". The diagram comprises more than 80 deposition experiments [63].

(Figure 10 is reprinted from *Diamond and Related Materials*, 1991. **1**(1), Peter K. Bachmann, Dieter Leers and Hans Lydtin, "Towards a general concept of diamond chemical vapour deposition" [Figure 1: a], p. 1-12, with permission from Elsevier Science Publishers B.V., Copyright 1991 [License Number: 4203731417983, License date: Oct 07, 2017]. DOI 10.1016/0925-9635(91)90005-U)

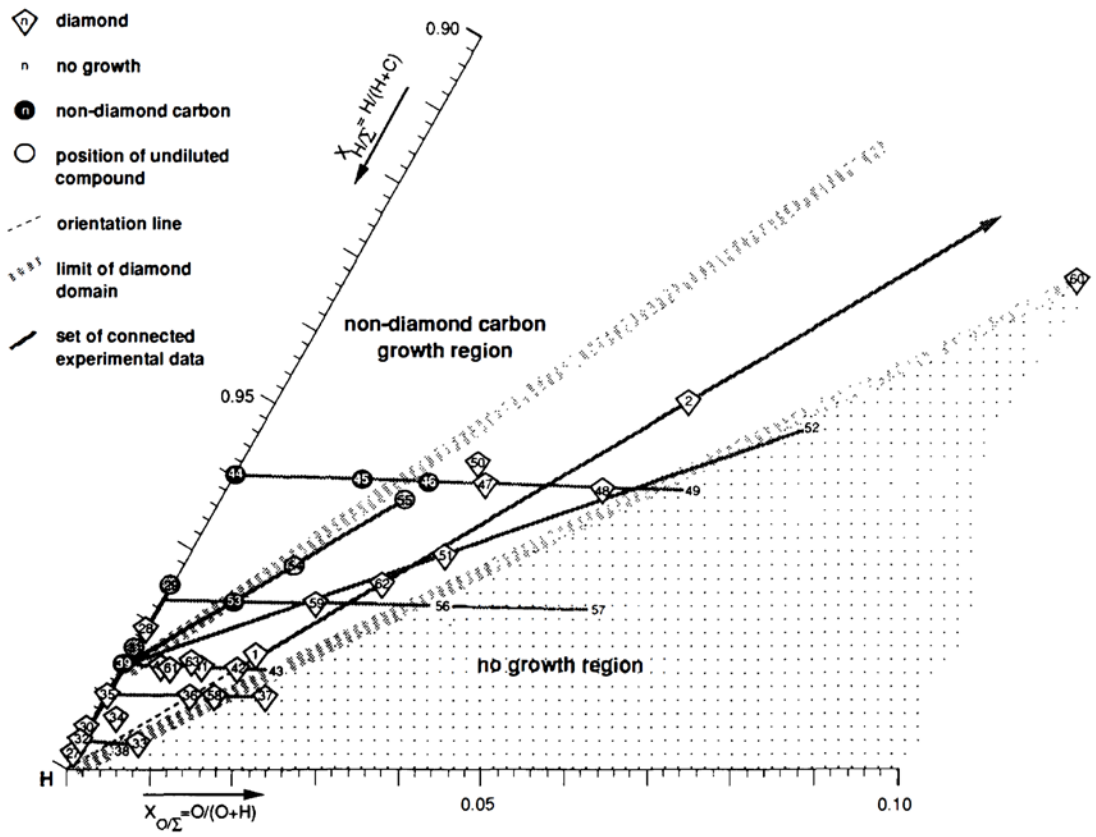

Figure 11: Enlarged hydrogen-rich sector of the phase diagram (Figure 10) [63].
(Figure 11 is reprinted from *Diamond and Related Materials*, 1991. **1**(1), Peter K. Bachmann, Dieter Leers and Hans Lydtin, "Towards a general concept of diamond chemical vapour deposition" [Figure 1: b], p. 1-12, with permission from Elsevier Science Publishers B.V., Copyright 1991 [License Number: 4203731417983, License date: Oct 07, 2017]. DOI 10.1016/0925-9635(91)90005-U)

Data point in Fig. 1	Reactants	CVD method	$X_{H\Sigma}$	$X_{C\Sigma}$	$X_{O\Sigma}$
1	$CO-H_2$	MW plasma	0.985	0.500	0.015
2	$CO-H_2$	MW plasma	0.947	0.500	0.053
3	$CO-H_2$	MW plasma	0.857	0.500	0.143
4 (also ○)	Pure methanol	MW plasma	0.800	0.500	0.200
5	$C_2H_2-O_2$	Flame	0.500	0.505	0.495
7	$C_2H_2-O_2$	Flame	0.500	0.469	0.531
8	$C_2H_2-O_2-H_2$	Flame	0.592	0.472	0.436
9 (growth limit)	$C_2H_2-O_2$	Flame	0.513	0.459	0.528
10 + 11 (growth limit)	$C_2H_2-O_2$	Flat flame	0.500	0.459	0.541
12	$C_2H_2-O_2-H_2$	Flat flame	0.558	0.463	0.479
13	$C_2H_2-O_2$	Flame	0.500	0.577	0.423
14	$C_2H_2-O_2$	Flame	0.500	0.536	0.464
15	$C_2H_6-O_2$	Flame	0.750	0.380	0.352
16	$CO-H_2$	Thermal (1 atm)	0.182	0.500	0.818
17	$CO-H_2$	Thermal (1 atm)	0.010	0.500	0.990
18	$CO-CO_2$	Thermal (cyclic)	0.000	0.488	1.000
19	$CH_4-CH_3COCH_3-O_2$	MW plasma	0.747	0.534	0.228
20 (also ○)	Pure acetone	MW plasma	0.667	0.750	0.143
21	$CH_3COCH_3-O_2$	MW plasma	0.667	0.600	0.250
22	$CH_3COCH_3-O_2$	MW plasma	0.667	0.549	0.291
23	$CH_3COCH_3-O_2$	MW plasma	0.667	0.524	0.312
24	$CH_3COCH_3-O_2$	MW plasma	0.667	0.491	0.342
25 (growth limit)	$CH_3COCH_3-O_2$ + CTR	MW plasma	0.667	0.476	0.355
26	$C_2H_4-O_2$	Flame	0.667	0.435	0.394
27	CH_4-H_2	MW plasma	0.998	1.000	0.000
28	CH_4-H_2	MW plasma	0.981	1.000	0.000
29	CH_4-H_2	MW plasma	0.977	1.000	0.000
30	CH_4-H_2	D.c. plasma jet	0.995	1.000	0.000
31	CH_4-H_2	D.c. plasma jet	0.983	1.000	0.000
32	CH_4-H_2	MW plasma	0.996	1.000	0.000
33	$CH_4-H_2-O_2$	MW plasma	0.997	0.333	0.007
34	$CH_3COCH_3-H_2$	Hot filament	0.993	0.750	0.002
35	CH_4-H_2	MW plasma	0.990	1.000	0.000
36	$CH_4-H_2-O_2$	MW plasma	0.990	0.500	0.010
37	$CH_4-H_2-O_2$	MW plasma	0.990	0.333	0.019
38 (no growth)	CO_2-H_2	MW plasma	0.997	0.333	0.005
39	CH_4-H_2	MW plasma	0.986	1.000	0.000
40	$CH_4-H_2-O_2$	MW plasma	0.986	0.754	0.005

Table 2: Data of deposition experiments included in the analysis. Where **MW**. microwave; **CTR**. chemical transport reaction; **ECR**. electron cyclotron resonance [63].

Data point in Fig. 1	Reactants	CVD method	$X_{H\Sigma}$	$X_{C\Sigma}$	$X_{O\Sigma}$
41	$CH_4-H_2-O_2$	MW plasma	0.986	0.607	0.009
42	$CH_4-H_2-O_2$	MW plasma	0.986	0.508	0.014
43 (growth limit)	$CH_4-H_2-O_2$	MW plasma	0.986	0.436	0.018
44	CH_4-H_2	MW plasma	0.960	1.000	0.000
45	$CH_4-H_2-O_2$	MW plasma	0.960	0.712	0.016
46	$CH_4-H_2-O_2$	MW plasma	0.960	0.622	0.024
47	$CH_4-H_2-O_2$	MW plasma	0.960	0.553	0.032
48	$CH_4-H_2-O_2$	MW plasma	0.960	0.452	0.048
49 (growth limit)	$CH_4-H_2-O_2$	MW plasma	0.960	0.398	0.059
50	$CH_4-H_2-H_2O$	MW plasma	0.957	0.595	0.030
51	$CH_4-CO_2-H_2$	MW plasma	0.970	0.485	0.032
52 (growth limit)	$CH_4-CO_2-H_2$	MW plasma	0.951	0.410	0.070
53	CH_4-CO-H_2	MW plasma	0.977	0.718	0.009
54	CH_4-CO-H_2	MW plasma	0.972	0.670	0.014
55	CH_4-CO-H_2	MW plasma	0.963	0.618	0.023
56 (growth limit; low flow)	$CH_4-H_2-O_2$	MW plasma	0.977	0.397	0.035
57 (growth limit; high flow)	$CH_4-H_2-O_2$	MW plasma	0.977	0.291	0.055
58	$CH_4-H_2-CO_2$	MW plasma	0.990	0.435	0.013
59	$CH_4-H_2-O_2$	MW plasma	0.977	0.556	0.019
60	$CH_4-H_2-CO_2$	ECR MW plasma	0.927	0.429	0.095
61	$CH_3COCH_3-H_2$	Hot filament	0.986	0.750	0.005
62	$CO-H_2$	MW plasma	0.974	0.500	0.026
63	$CH_4-H_2-H_2O$	MW plasma	0.986	0.652	0.008
64	$CO-CO_2-H_2$	MW plasma	0.781	0.475	0.237
65	$CO-CO_2-H_2$	MW plasma	0.787	0.482	0.225
66 (growth limit)	$CO-H_2-O_2$	MW plasma	0.800	0.450	0.234
67	$CO-CO_2-H_2$	MW plasma	0.772	0.465	0.254
68	$C_2H_2-CO_2$	MW plasma	0.333	0.492	0.682
69 (not shown)	$CH_4-CO_2-H_2$	MW plasma	0.977	0.560	0.018
70 (not shown)	$C_2H_2-O_2$	Flame	0.505	0.467	0.528
71 (growth limit, not shown)	$C_2H_2-O_2-H_2$	Flame	0.600	0.472	0.428
72 (not shown)	$C_2H_2-O_2-H_2$	Flame	0.524	0.472	0.505
73 (not shown)	$CH_4-CO_2-H_2$	MW plasma	0.981	0.672	0.009
74 (not shown)	Example in eqn. (4)		0.935	0.545	0.054
(undiluted)	Pure CO		0.000	0.500	1.000
(undiluted)	Pure CH_4		0.800	1.000	0.000
(undiluted)	Pure CO_2		0.000	0.333	1.000
(undiluted)	Pure C_2H_4		0.667	1.000	0.000
(undiluted)	Pure C_2H_6		0.750	1.000	0.000
(undiluted)	Pure C_2H_2		0.500	1.000	0.000
(undiluted)	Pure C_2H_5OH		0.750	0.667	0.143

Table 2: continued.

2.2. Seeded growth

Nucleation of nanodiamonds from the gas phase with high nucleation density (~ 10^8 cm^{-2}) using a hot-filament assisted chemical vapor deposition was reported by Ajji, Z., *et al.* [12]. They ran the experiment with 0.5% methane in 100 sccm of CH_4/H_2 mixture. The other conditions were: ~24 Torr pressure, 2000-2200°C filament temperature, and the temperature of the Si wafer substrate was 800-850°C. The presence of nickel (Ni) wire and a CVD diamond membrane enhanced the nucleation density where the distance between the Ni wire and the substrate was around 0.1-0.5 mm. The existence of Ni wire significantly raised the nucleation rate by two orders of magnitude more than the diamond film. Also, there is an inverse proportion between the nucleation density and the heights of both the Ni wire and the diamond disk from the substrate.

Han, Y. X., *et al.* [64] have investigated the diamond nucleation by graphite seeding, with a continuous CO_2 laser irradiation, and C_2H_2/O_2 combustion flame which was directed toward the substrate at ~ 55° to the substrate surface normal. A thin layer of graphite powder (< 1 μm) was produced from copper (Cu) substrates seeded with a graphite aerosol spray. The C_2H_2/O_2 ratio was set to be 1% of a total 2.5 *slm* gas flow rate. As a consequence of heating the graphite seeds by the CO_2 laser to 750 °C for 1 min and utilizing the combustion flame, 4 μm of diamond film was deposited on the substrate. Diamond formations on virgin and graphite seeded Cu substrates were examined. The synthesized diamond sizes on the graphite seeded surface were smaller than on the virgin surface; for instance, after 2 min of deposition the diamonds' average sizes were 1.5 μm and 4 μm respectively. There was a correlation between increasing the nucleation site

density and decreasing the crystal sizes. To investigate the effectiveness of the CO_2 laser, a few experiments were performed without a CO_2 laser for 2, 5, and 15 min under the same conditions where the temperature of the substrate was also 750 °C. In 2 and 5 min, diamonds were detected. While after 15 min of deposition, large diamond crystals and diamond film with a thickness of 5.5 μm were observed on the graphite seeded and virgin Cu substrates respectively.

Yi-Chun Chen and Li Chang [14] used adamantane solutions with a thick layer of ethylene or diethylene glycol on Si wafers for the construction of diamonds. They've reported that the experiment was running under the following condition: 30 Torr, one-hour deposition time, 2:98 CH_4:H_2 ratio, 300 sccm total volumetric flow rate, 600°C, and the microwave power was 800 W 1. Also, the same group presented a new technique for synthesizing diamonds on an adamantane-coated sapphire substrate. The conditions were slightly different than the previous one. Rajanish N. Tiwari and Li Chang [65] have used MPCVD for the formation of a good-quality diamond film on an adamantane-coated Si substrate at a relatively low temperature ~ 530°C. The conditions of this study were: total pressure, 20 Torr; MW power, 350 W; total volumetric flow rate, 200sccm; running time, between 15 to 270 min. K. Tsugawa *et al*. [66] have grown monocrystalline diamond film using a CH_4 (1-5 %)/ CO_2 (1-5 %)/ H_2 (90-98 %) mixture aided with Adamantane seed to enhance the nucleation of diamond crystals. The produced ND has an initial nucleation density around 10^{11} cm^{-2}. MW power of 10-20 kW at 2.45 GHz, a pressure range of 20-100 Pa, and the substrate temperature at ~ 150°C were applied.

Tzeng, Y.-K., *et al.* [67] developed a microwave-plasma CVD technique to grow NDs using pentamantane ($C_{26}H_{32}$) as a seed. A hydrogen plasma was applied; in this configuration, atomic hydrogen density, temperature, and plasma density continuously differed over the length of the substrate. This advantage comes from the orientation of the substrate vertical to the electrode, so as to expose the seed to diverse conditions from bottom to top. Different growth parameters along the substrate height yielded various crystal diamonds' sizes which were from 10 nm to 75 nm in diameter. The experiment was run with pressure, 23 Torr; CH_4, 0.5 sccm; H_2, 300 sccm; microwave power, 400 W; stage temperature, 350 °C. Diamond growth was on nitrogen-doped (N-type) silicon carbide ⟨0001⟩. Due to the lower atomic hydrogen density and the higher temperature near the top, there were more particles but polycrystalline. Meanwhile, because of the higher density of atomic hydrogen and lower temperature near the bottom, the particles were well-faceted and single-crystal. Computer simulations have been done to study the disparate growth conditions which were presented as a function of distance along the vertical substrate. Comsol Multiphysics software was utilized for these simulations. The results of modeling have suggested that the plasma electron density was concentrated at the top-edge of the Si-wafer.

Oriented diamond particles on single crystal cobalt (Co) ⟨0001⟩ substrates using a hot-filament chemical vapor deposition approach have been nucleated by Liu, W., *et al.* [68]. A multi-step procedure was followed which includes seeding with either diamond or graphite powders, annealing, nucleation, and then a diamond growth process. Based on the seeds species, two types of experiments have been done. The first experiment utilized

1-2 μm of diamond powder as a seed. The cobalt substrate was pretreated by coating with a suspension of diamond powder in acetone; after the acetone evaporation, a layer of diamond powder was generated. The cobalt substrate was annealed in a hydrogen atmosphere, at 900 °C for 10- 30 min. Then the temperature of the cobalt substrate was raised and fixed at 1100 °C for a duration ranging from 10- 60 min to dissolve the seeds into the cobalt. After that, the cobalt substrate temperature was reduced in in temperature to 900 °C for diamond nucleation. The conditions of diamond growth were: pressure, 30 Torr; total flow rate, 600 sccm; CH_4/H_2 ratio, 0.3%. Another pretreatment was done to the cobalt substrate with CH_4/H_2 ratio of 5.0% at 1100 °C in a hydrogen environment to fabricate the Co-C-H intermediate surface layer. Graphite powders ranging from 10 to 15 μm in size were suspended in acetone, dried, and annealed as described previously. These attempts showed the formation of ⟨111⟩ oriented diamond particles.

3. EXPERIMENTAL APPARATUSES, SETUPS, AND TECHNIQUES

3.1. Introduction

The experiments in the present work have helped to increase our understanding of the effectiveness of plasma power, volumetric flow rates, the concentration of carbon sources, and gas mixture systems. Changing the experiments' parameters was extremely advantageous for enlarging our comprehension to the suggested growth method and for making our products' analysis coherent and scientifically logical. From this sense, we have tried in the present work different gases, mixtures, concentrations, volumetric flow rates, runtime, and plasma powers. Capacitively coupled radio frequency (CCRF) plasma discharge, and microwave (MW) plasma discharge have been applied. In some cases, the previous works results were utilized to support and solidify our proposals as well as to improve and upgrade our own designs. New developments have resulted from the understanding we have gotten. Our work was divided in two parts which focused in the beginning on non-seeded growth and then on seeded growth.

Three designs of reactors were tested. Two small designs were tested with a RF plasma discharge while the third one (large design) was used with a MW plasma discharge. After the tests, we did many of the experiments under a wide range of conditions. If we chose the RF plasma power to be fixed, for example, then we changed the rest of the parameters to build a map for several experiments. This map intends to discover if there is a clear trend we should follow to help us recognize the underlying phenomena and then facilitate the path to reach our objective.

3.2. Built-in setups and techniques

3.2.1. Optical characterization setups

A confocal laser scanning microscopy setup was built to do optical characterization of the samples before and after a chemical treatment or air oxidation. The confocal setup is capable of measuring the Raman spectrum using two kinds of lasers, red (671nm) and green (532nm). The returning light from the sample, in our confocal setup, also passes a beam sampler to create an image of the sample on a CCD camera. This allows us to get a live look at the sample and then to make the needed adjustment. Confocal scans in XYZ directions are valuable features of this setup. Galvo scanner and electrically tunable lenses (Optotune electrically Focus-Tunable Lenses, Low Dispersion, VIS Coated, Edmund Optics Inc.) were used for the XY scanning, and Z scanning respectively. This set up is easily upgradeable to get an Optically Detected Magnetic Resonance (ODMR) capability, for instance.

A beam splitter (50/50) was utilized to play a double role in the setup. First to reflect the collimated laser to the galvo scanner and then to the excitation system (i.e., telescope, objective, and sample stage). The second role is to transmit the fluorescence to the detection system (pinhole- detectors).

The components of the excitation system are pairs of 2Ø" lenses with 15 cm focal length, 100x objective (Olympus MPlanAPO, ∞/0) with a numerical aperture (NA) 0.95, and the last is an XYZ translation stage to modify the sample position manually. From our experience, we found that the 15 cm focal length lenses are the best match for the microscope objective.

The spectral detection system (i.e., spectrometer) has a pinhole (100μm), a (50/50) beam splitter, lenses, a grating, a camera (Starlight Xpress Ltd, Trius SX-674, cooled CCD camera system), and a photon counting (Hamamatsu, model H7155-21). Refocusing the emitted fluorescence from the specimen onto the pinhole makes it perform as a light filter. Discarding undesirable light from the sample that was not from the focal point is another beneficial attribute of the pinhole, as in any confocal system. Figures 12 and 13 show the constructed spectrometer and the basic design of our confocal setup respectively.

We have written a Python code for controlling some devices (i.e., galvo scanner, tunable lenses, photon counting, cameras) for detecting, and analyzing of the collected data.

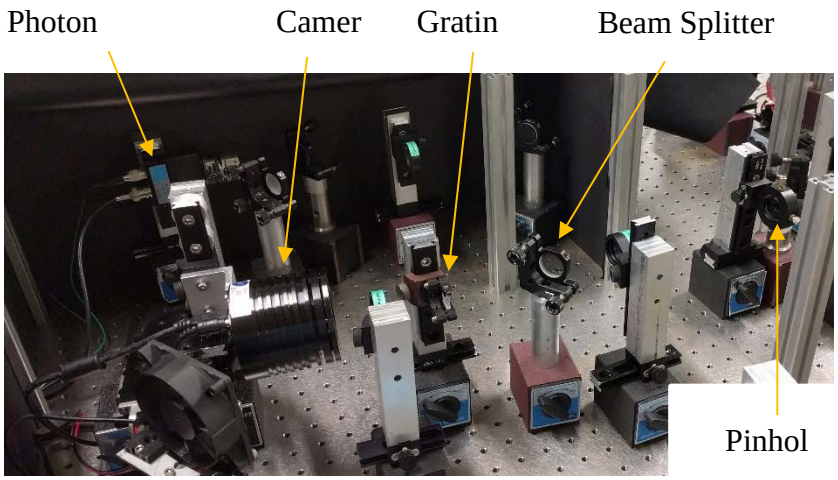

Figure 12: The detection division (*i.e.*, Spectrometer).

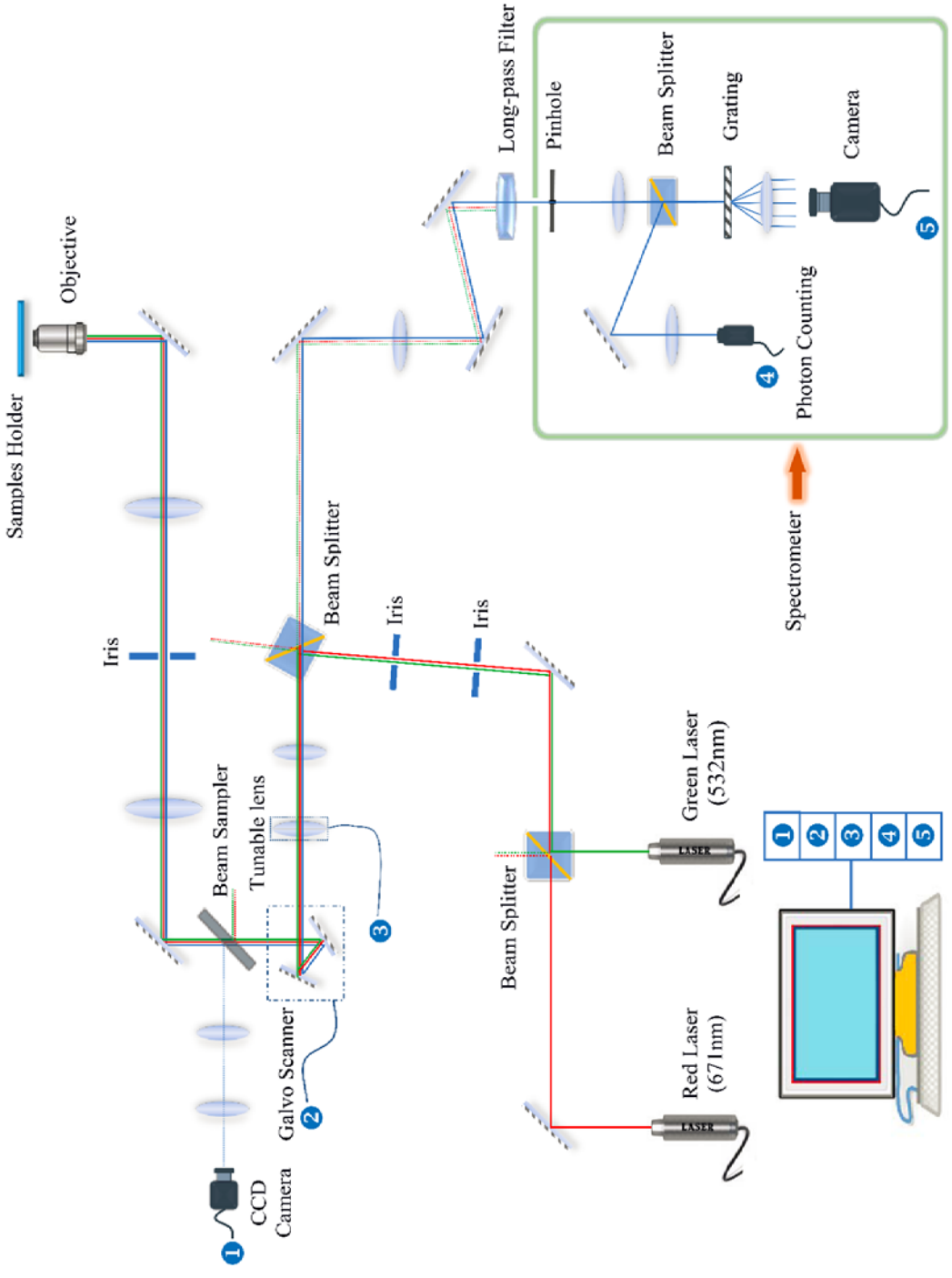

Figure 13: Basic design of our confocal laser scanning microscopy setup.

3.2.2. Thermal oxidation in air setup and technique

The importance of air oxidation comes from the impurity of our collected materials. In most of the experiments, the sample collection filters have impurities such as graphite or amorphous carbon in much higher quantities than the nanodiamonds. Organic compound contaminations were also observed due to the breakdown of the large hydrocarbon molecules by the plasma. Thus, oxidation of the samples in the air (which has 20% oxygen) was performed at atmospheric pressure for 10 mins at 550°C to etch the non-diamond carbon (sp^2 carbon) and organics. Oxidative etching can also be used as a top-down technique of production NDs where the key function of oxygen in the air is oxidizing the carbon and reduce nanodiamond size. Additionally, heating the sample to 550°C with forming gas rather than air at atmospheric pressure was proposed to remove only the organic compositions from the filters. Figure 14 illustrates a schematic of the oxidation setup.

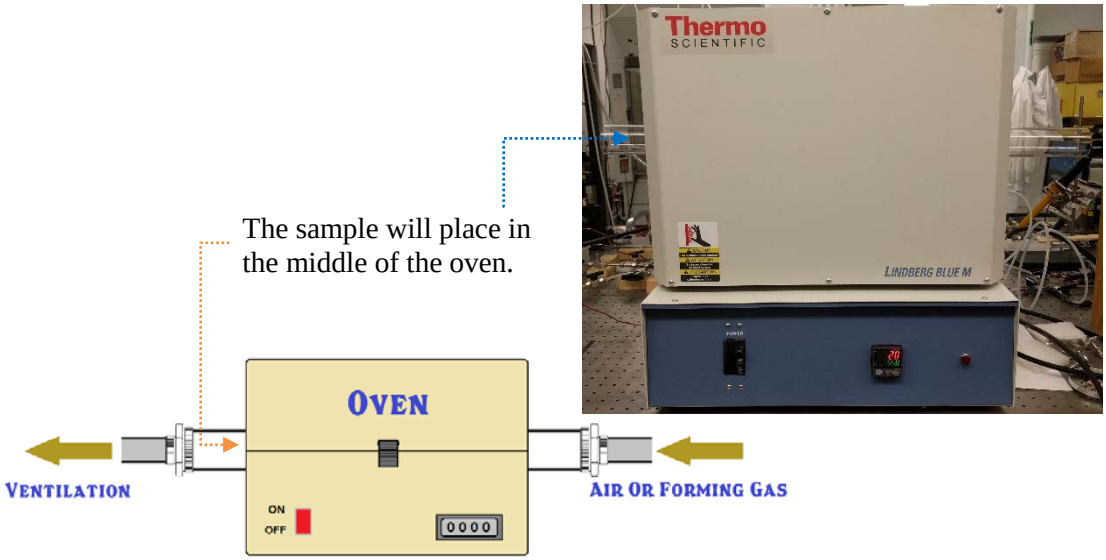

Figure 14: Oxidation setup.

Gaebel, T., *et al.* [69], have investigated the size-reduction of nanodiamonds via air oxidation. They reported that at atmospheric pressure, the average size reduction of individual crystals from air oxidation was lower than 1 nm/h at 500 °C, 4±1 nm/h at 550 °C, and 10±1 nm/h at 600 °C. Annealing DNDs at 520 °C for 25 min has been done by Stehlik, S., *et al.* [70]. They laid out a controllable size-reduction of DNDs down to 1.4 nm. 520 °C annealing temperature was selected since it lies between the point that DNDs thermal weight loss starts (480 °C) and the temperature where intense weight loss onsets (560 °C). Also, mean sizes of HPHT NDs after air-annealing were reduced by only 1.1 nm. Thus, the main effect of thermal annealing NDs in the air is etching sp^2 carbon.

Figure 15: Oxidation tests for commercial samples[1].

Using our setup (i.e., Figure 14), we did numerous oxidation tests for commercial samples (detonation soot and standard ND, see Figure 15). These samples were oxidized at different temperatures and times. Based on previous studies, our tests were aimed to achieve the optimal oxidation conditions that we should follow when oxidizing the collected material from the real experiments. Furthermore, Figure 15 presents both the air oxidation and chemical treatment of commercial samples.

[1] Detonation soot and standard nanodiamond (4-5 nm primary particle size which is 200nm average agglomerate size) are commercial samples (International Technology Center). They have been tested at various time and temperatures.

3.2.3. Chemical cleaning setup and technique

Chemical cleaning is a common procedure for removing metal, graphite, amorphous carbon, or any organics contaminations from the surface of the diamonds. It has been widely used due to its strong interaction with impurities, but inability to harm the diamond. Since there were many types of contaminations in our products, it was imperative for us to treat the collected materials with diverse procedures. One of them is the thermal oxidation which was mentioned previously, and the chemical treatment or cleaning is another mechanism. In order to remove graphite, metals, silicon, and organic compounds, we have picked the chemical treatment to process our materials first. Scientists have utilized several chemical recipes that vary in strength depending on the purpose of usage.

The followings are some chemical formulae including the goal of treatments:

3.2.3.1. Acid piranha solution

Piranha solution is a 1:3 mixture of hydrogen peroxide (H_2O_2) and sulfuric acid (H_2SO_4). Since this mixture is a robust oxidizer, it was chosen to remove most of the organic residues. Piranha solution is an extremely dangerous mixture, so care must be taken when handling it. Safety guidelines have recommended preparing a fresh mixture for each use, and they strongly warn against storing any leftover piranha solution. One of the possible reactions between sulfuric acid and hydrogen peroxide in the mixture is

$$H_2SO_4 + H_2O_2 \rightarrow [H_3O]^+ + [HSO_4]^- + O$$

Molecular oxygen is highly reactive atom that attacks organics and can react with free carbon atoms.

3.2.3.2. Aqua Regia

It is a 1:3 mixture of nitric acid (HNO_3) and hydrochloric acid (HCl). It has been used for etching and chemical cleaning of metals and organic compounds from glassware. Aqua Regia is a strong acid which requires careful storage and handling. The following reactions are examples of Aqua Regia uses:

$$FeS_2 + 3\ HCl + 5\ HNO_3 \rightarrow FeCl_3 + 5\ NO + 2\ H_2SO_4 + 2\ H_2O$$

$$Au + 4\ HCl + HNO_3 \rightarrow HAuCl_4 + NO + 2\ H_2O$$

$$4\ HCl + 2\ HNO_3 + Sn \rightarrow SnCl_4 + NO_2 + NO + 3\ H_2O$$

3.2.3.3. Hydrofluoric (HF) acid

Hydrofluoric (HF) acid is an exceedingly reactive acid with glass. For this reason, (i.e., the high reactivity of HF acid with silicon oxide) it has been used in our cleaning procedure for the collected material. The reaction between HF and silicon dioxide (quartz, SiO_2) can be written as:

$$SiO_2 + 4\ HF \rightarrow SiF_4(g) + 2\ H_2O$$

HF has a powerful ability to penetrate tissue. Direct contact with HF acid will lead to acute effects and serious injury. It is a very toxic acid and requires a high level of attention and care when working, handling, and storing. Typically, HF acid is stocked up in plastic containers due to its excessive reactivity toward glass.

In laboratories, calcium gluconate ($C_{12}H_{22}CaO_{14}$), as a source of Ca^{++}, has been mainly used for first aid, as an antidote for hydrofluoric acid treatment, and for neutralizing HF, when employed appropriately and speedily.

$$2\ HF + Ca^{++} \rightarrow CaF_2$$

3.2.3.4. Nitric (HNO_3) and sulfuric (H_2SO_4) acids mixture

A 1:1 ratio of this mixture has been elected to utilize in our decontamination procedures because they are strong oxidizing agents. Heating this mixture to the boiling point will increase HNO_3 and H_2SO_4 reactivities. Our group and other laboratories have used this mixture for cleaning metal and graphite contaminations from bulk diamond surfaces. Also, in this regard, nitric and sulfuric acids are relatively safe to use, and they won't etch the diamond. Adding perchloric acid ($HClO_4$) to the mixture with 1:1:1 ratios has been proven to give better results.

The following reactions are a few examples of these two acids reacting with metals and carbon.

$$C + 2\ H_2SO_4\ (aq) \rightarrow CO_2 + 2\ SO_2\ (g) + 2\ H_2O$$

$$C + 4\ HNO_3\ (aq) \rightarrow CO_2 + 4\ NO_2\ (g) + 2\ H_2O$$

$$Ca\ (s) + H2SO_4\ (aq) \rightarrow CaSO_4\ (aq) + H_2\ (g)$$

$$Mg\ (s) + 2\ HNO_3\ (aq) \rightarrow Mg(NO_3)_2\ (aq) + H_2\ (g)$$

We have treated our collected materials with the following chemical procedure:

- Acid cleaning: Boil the sample using HNO_3, H_2SO_4, $HClO_4$ and (with ratio 1:1:1) for 12 hr. The built-in setup for the chemical treatment is illustrated in Figure 16.
- Acids removing & drying:
    - Centrifuge the sample for 30 min.
    - Remove the supernatant and then dilute the precipitate with DI water.
    - Repeat the previous two steps a few times to increase the pH level.
    - Dry the precipitate in the drying oven.

- HF (3%) cleaning: put the dry sample with HF in a polyethylene or Teflon container for ~12 hr.
- Acids removing: do the centrifuging and remove the supernatant as explained previously to increase the pH level.

The residual materials after chemical cleaning will be treated with an aur oxidation techinique to remove any remaining graphite or amorphous carbon impurity (see Figure 15).

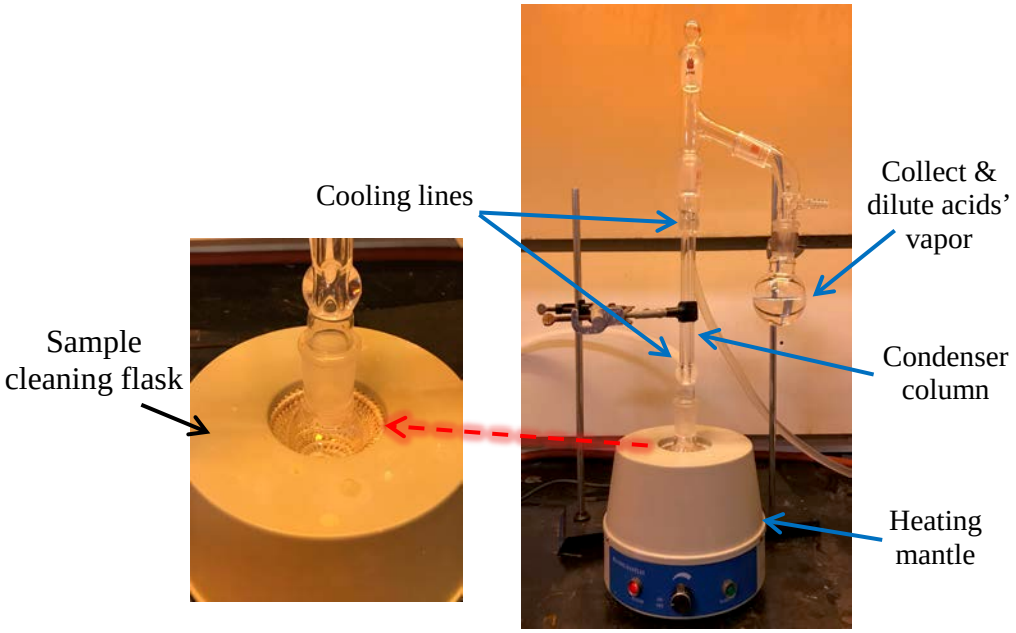

Figure 16: Chemical treatment setup.

3.2.4. Ultraviolet-Ozone cleaning technique

We employed the UV-O_3 treatment technique primarily to decompose or turn the organic material on the sample into volatile gases such as water vapor, oxygen, and carbon

dioxide (PSD Series, Digital UV Ozone System, Novascan Technologies, Inc.). The basic principle of UV-O_3 cleaning is to use the high-intensity wavelengths (1849.499 Å and 2536.517 Å), which are persistent lines of neutral mercury atom in low-pressure mercury vapor lamps. This starts by irradiation diatomic oxygen gas (O_2) with 1849.499 Å UV to form ozone (O_3). Then irradiation of the ozone with 2536.517 Å UV to create an oxygen atom (O^*). The oxygen atom, which has a strong oxidizing ability, will oxidize the organic compounds converting them to volatile gases [71, 72]. The working mechanism of UV-O_3 is presented in Figure 17.

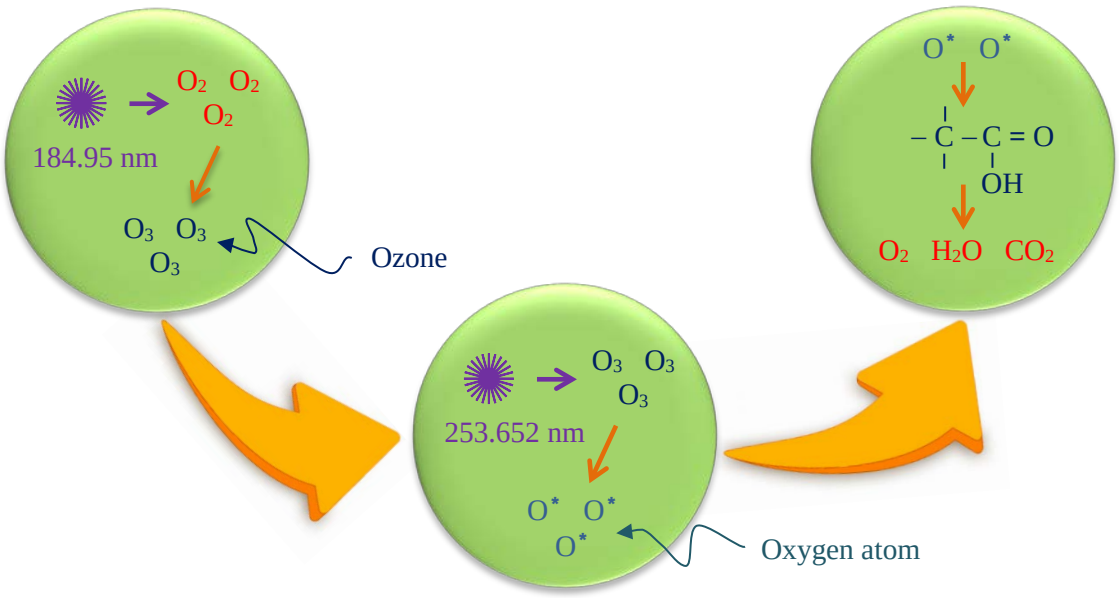

Figure 17: Ultraviolet-Ozone treatment mechanism.

3.2.5. DC plasma discharge setup

We have proposed and built the first version of this setup to illustrate the advantages of the DC plasma discharge technique for manufacturing NDs. This setup was equipped with a live observation region for nucleated materials which consisted of a filter that is monitored by a camera and a laser Raman spectrometer. This live monitor makes it easy to adjust the collection time and allows longtime optical characterization of the plasma (i.e., Raman spectrum) during the experiments. The first experiment was done with Ar, cyclohexane (C_6H_{12}, $\geq$ 99.9%), and adamantane ($C_{10}H_{16}$, $\geq$ 99%). The adamantane was dissolved in the cyclohexane with ratio 1:99 ($C_{10}H_{16}$:C_6H_{12}). A DC power supply at 6 KV and 8 mA was employed to generate a DC plasma between two graphite electrodes (Poco Graphite, EDM Grade). Figure 19 (a & b) displays photos of the reactor's design and the plasma discharge between the electrodes respectively. The components of the optical characterization setup, are shown in Figure 18. They include pairs of 2Ø" lenses and 20x objective (Objective Yelled [OY], Plan Achhro, CAT-2556) with a numerical aperture (NA) 0.50. Also, the spectrometer has a pinhole (100μm), a grating, a camera (Starlight Xpress Ltd, Trius SX-674, cooled CCD camera system), and some lenses.

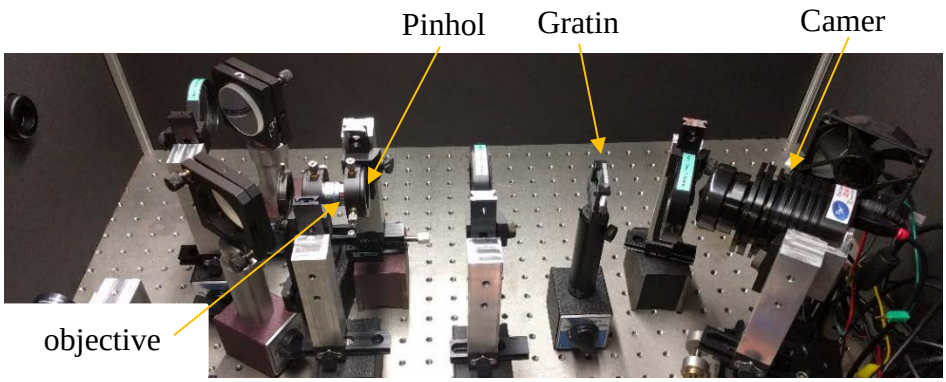

Figure 18: DC plasma discharge spectrometer.

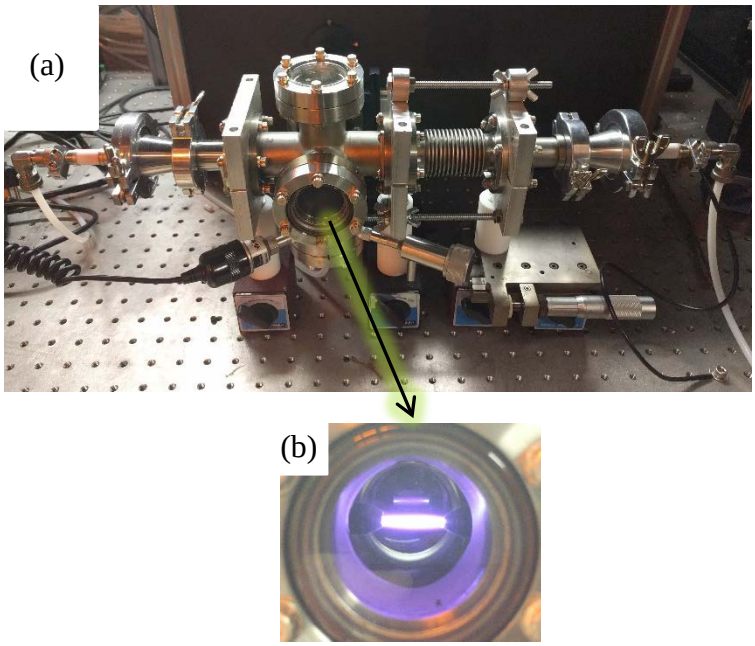

Figure 19: (a) Design of the reactor. (b) DC plasma discharge between the graphite electrodes where the distance between the electrodes was ~1.5 cm.

The high cost of modernizing this setup led to our exploration of other options. In addition, the existence of a plasma sheath (also called electrostatic potential structure) was another problem, as the strength of the plasma sheath causes dissociation of both the

cyclohexane and adamantanes' bonds. As a result, liquid materials were produced by the plasma which is undesirable and hinders the use of seed molecules for NDs' formation. In our design, since the length of the plasma discharge was short (the distance between the electrodes around ~ 1-2 cm), the radicals' residence time was also short this made the seeded growth very difficult. Increasing the distance between the electrodes made the generation of the plasma much more difficult, especially at low pressure. A schematic of the built-in DC plasma discharge is illustrated in Figure 20.

3.2.6. Radio frequency (RF) plasma discharge setup

This setup was designed to run experiments with various plasma gases such as argon and hydrogen. We exploited dissimilar gases like Ar, CO_2, O_2, or H_2, plus some diamond precursors, like, CH_4, CH_3OH (≥ 99.9%), CH_2Cl_2 (99.9%), and SiH_4 (≥ 0.8% silane in argon). In addition, organic and nonorganic source of diamond seeds have been suggested such as adamantane and diamond nanocrystals, respectively. A group of four flow rate controllers (MFCs) regulated with 4 channels controller (Brooks, Gas and liquid mass flow secondary electronics, model 0254) was utilized. Calibration of the MFCs was accomplished by a flowmeter (Restek's ProFLOW 6000) to ensure that our calculated d flow rates agree with the MFCs readout.

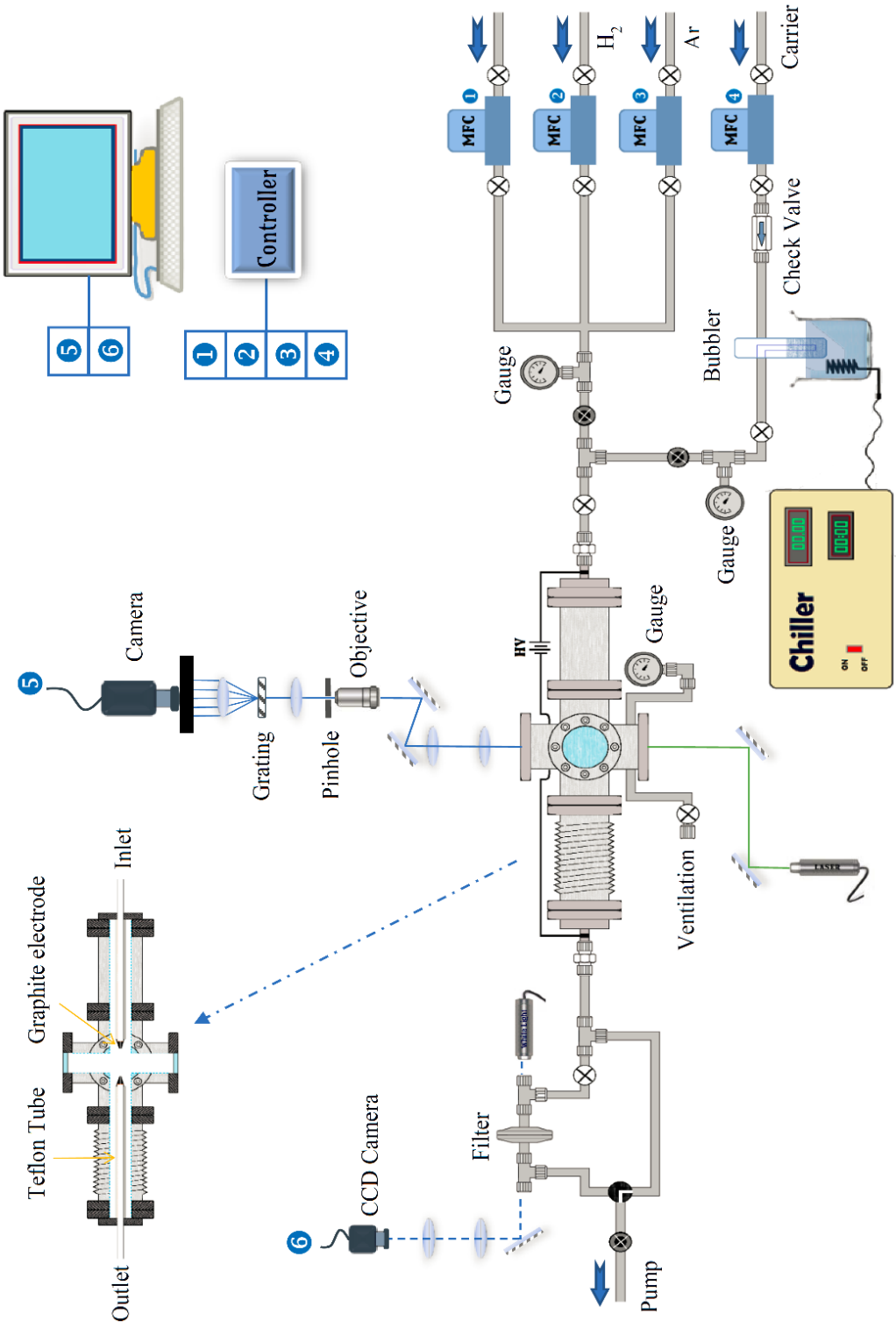

Figure 20: Schematic of the DC plasma discharge setup

The setup was subject to excessive leak tests (Restek's leak detector, cat. # 22655) after we connected the components and when we moved or replaced any part. Pressures of the reactor (downstream) and upstream (precursor or bed) were measured by a convectron Pirani vacuum gauge (MKS, Granville-Phillips 275) and a baratron (direct [gas independent] pressure/vacuum capacitance manometers, MKS, 0.1-1000 Torr). The carrier gas volumetric flow rate and both the pressure and the temperature of the organic compounds were adjusted to control the diamond precursors' mass flow rates. For controlling the temperature of the organic compounds, we used an immersion cooler (Julabo USA, Inc., model FT402) with silicone oil. The RF capacitively coupled plasma discharge was generated via a radio frequency (13.56 MHz) power supply source with maximum power 300W (RF VII. Inc., model RF-3) and a homemade manual matching network.

An optical emission spectrometer (Ocean Optics high-resolution fiber optic spectrometers, model HR4000) was employed to measure the Optical Emission Spectrum (OES) before the experiment to test the reactor for contamination as well as during the experiments to monitor growth species. PTFE filters (Omnipore membrane filter, hydrophilic, with a 0.1 μm filter pore size, JVWP02500) and quartz filters (Quartz fiber membrane filter without binder, QFA03700) were employed to collect reaction products. The capability to heat the filter to a high temperature after the experiments for air oxidation treatment of the product was the advantage prompted us to utilize the quartz filters. We started our experiments with a small straight reactor (quartz tube with 7mm inner diameter and 12 inches in length) where the Ar, precursor, and adamantane passed through the RF

plasma. Before we put in the adamantane seed molecules, we did scores of experiments with dissimilar environments trying to determine which parameters play key roles in controlling the product formation, quantity, morphology, and crystallinity structure.

After discovering that the adamantane was broken down into smaller organic compounds producing a yellow liquid, we reformed the reactor design (i.e., Tee design) as shown in Figure 21. The new reactor increased our ability to control the plasma position relative to the adamantane inlet point. Figure 21 also illustrates the seeded nanodiamond growth concept. Methane (CH_4) as a carbon source has selected to start with since it is commonly used in almost all the CVD experiments. Very little research has been published about synthesizing NDs from compounds other than methane. So, we also tried out more complex carbon-based compounds with or without nono-carbon functional groups, required to create color centers like NV.

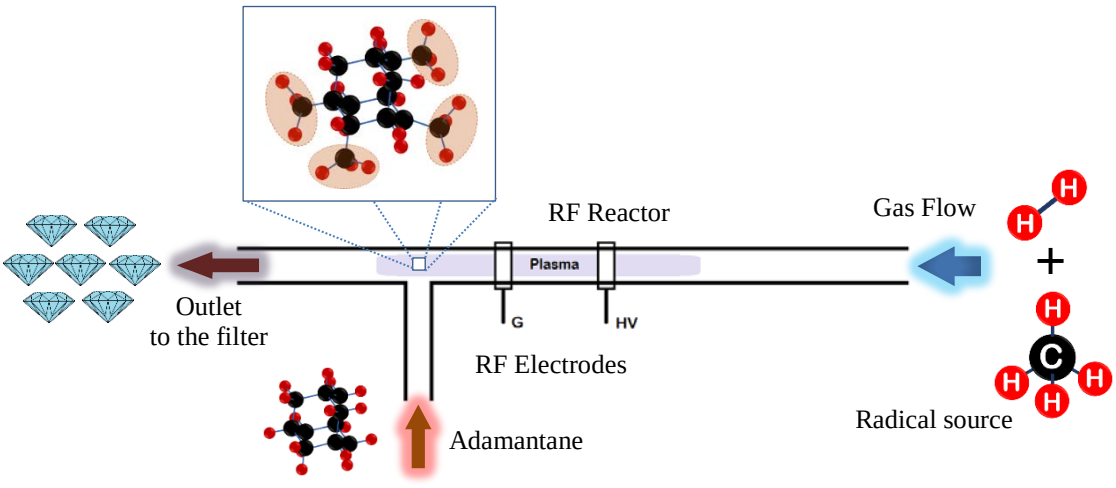

Figure 21: The tee reactor with the concept of seeded NDs growth.

Some upgrades were then done on the first reactor design (i.e., Figure 21). We positioned two stages of seed molecule heating before and after the plasma to create a convenient environment for the seeds to interact with the radicals which have come from plasma. Figure 22 exhibits the new updates of the system. Additionally, to give us enough room for modifying some growth parameters, we increased the length of some of the branches. A schematic of the final design of the RF system that we used in our seeded experiments is shown in Figure 23. Finally, Excel sheets were generated to calculate mass, volumetric flow rates, and condensation rates using gases laws, mole fraction formulas, and a ternary plot was generated.

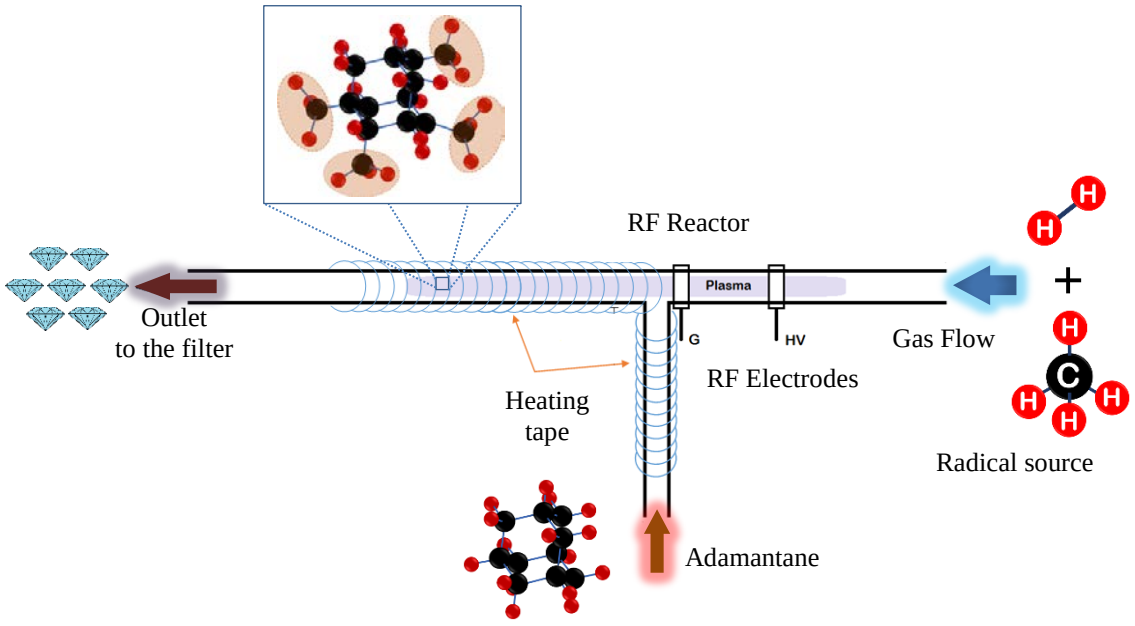

Figure 22: New upgrades that have been done on reactor design.

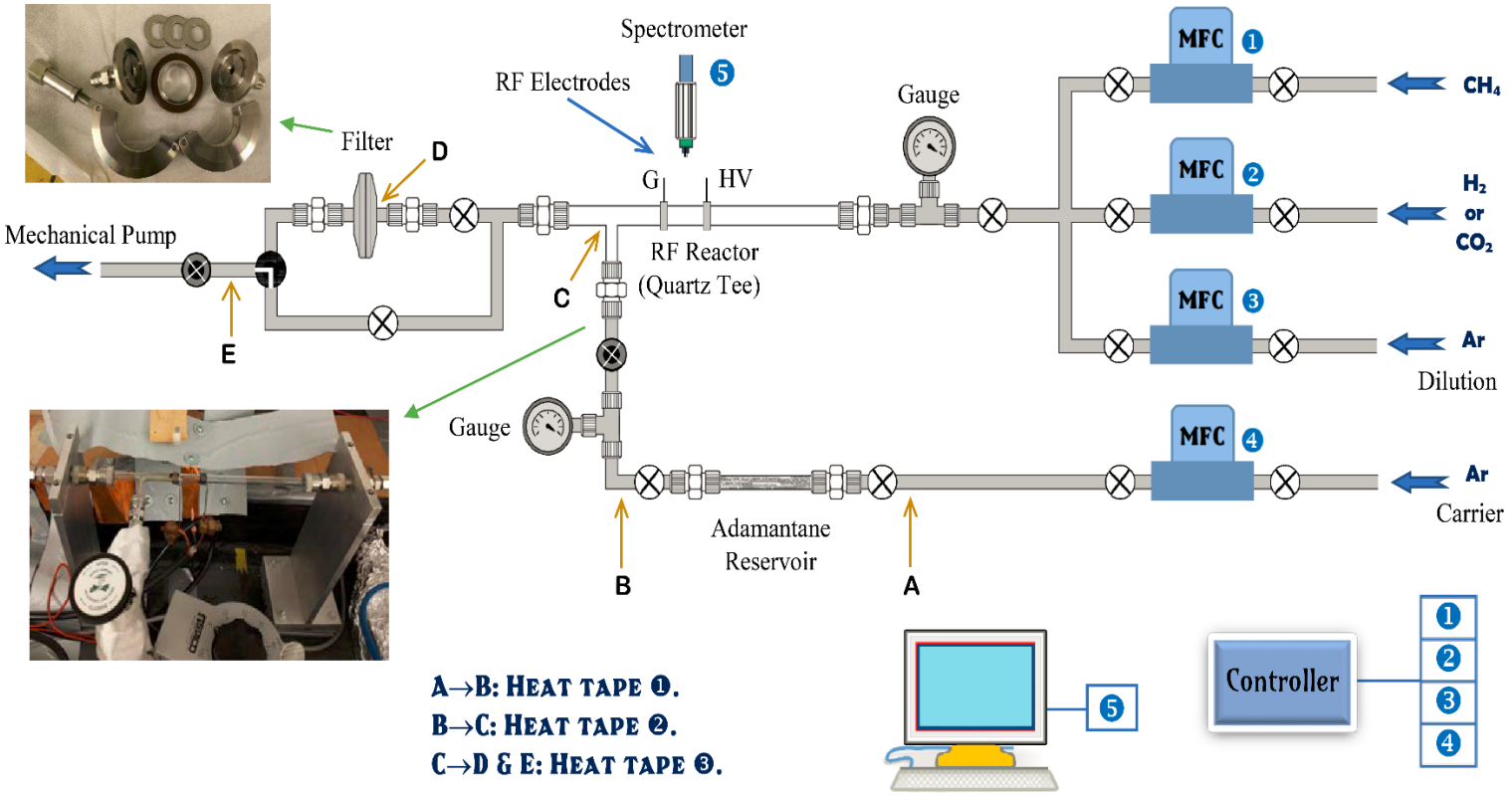

Figure 23: Final design of the inductively coupled RF discharge setup.

3.2.7. Microwave (MW) plasma discharge setup

Relying on the results we previously obtained from RF plasma discharge experiments, we have built a more sophisticated system with a different plasma source; namely microwave plasma. Microwave (MW) plasma is classified as high temperature (or thermal) plasma where the electron density (n_e) was around 10^{12} cm^{-3}, electron temperature (T_e) between 3-5 eV, and the frequency equal to 2.45 GHz. The sheath in the MW plasma discharge is much less intense than in the RF capacitively coupled plasma discharge and the Dc plasma discharge. This feature of MW plasma was one of the forces that highly impacted our system design. A commercial kitchen microwave (Mainstays, 0.7 cu.ft., 700 W) was used to generate the MW plasma discharge.

We have employed three types of gases, Ar, H_2, and N_2 where the Ar and H_2 were combined as forming gas (≤ 5% hydrogen in argon). The organic precursors were CH_2C_{l2} (99.9%) and $C_6H_{15}N$ (≥ 99%). A group of five flow rate controllers (MFCs) were exploited and regulated separately by homemade controllers. As elucidated in Figure 24, the system was structured in a vertical arrangement and the reactor was a straight quartz tube with 46 mm inner diameter and 2.5 m in length. There are two 0.5-inch inlets quartz tubes branches for gas precursor mixing and mixing with seeds. This system was equipped with a long heating stage (~ 1.5 m) after the plasma region and with two positions for collecting product. Small particles will gather on quartz filters (Quartz fiber membrane filter without binder, QFA03700) and the big particles will fall into a quartz container on the bottom of the system.

A homemade stainless-steel bubbler was built for controlling the temperature of the organic precursors mixtures, and a seed molecule chamber was constructed as well. The temperature was monitored by an immersion cooler (Thermo Fisher Scientific, Neslab CC-100). Four main points were targeted to measure and set the pressures using vacuum gauges and needle valves. Two of them are oil-less mechanical vacuum gauges located in the bubbler and seeds sections. The other two are digital vacuum gauges (Mastercool, 20,000 to 1 mTorr in range, model # 98061) connected to the reactor and the vacuum pump. The seed molecule chamber was also heated by heating tapes. One of them was wrapped around the seed reservoir, and the second was twisted around the line between the seed chamber and the reactor to prevent any deposition in the line.

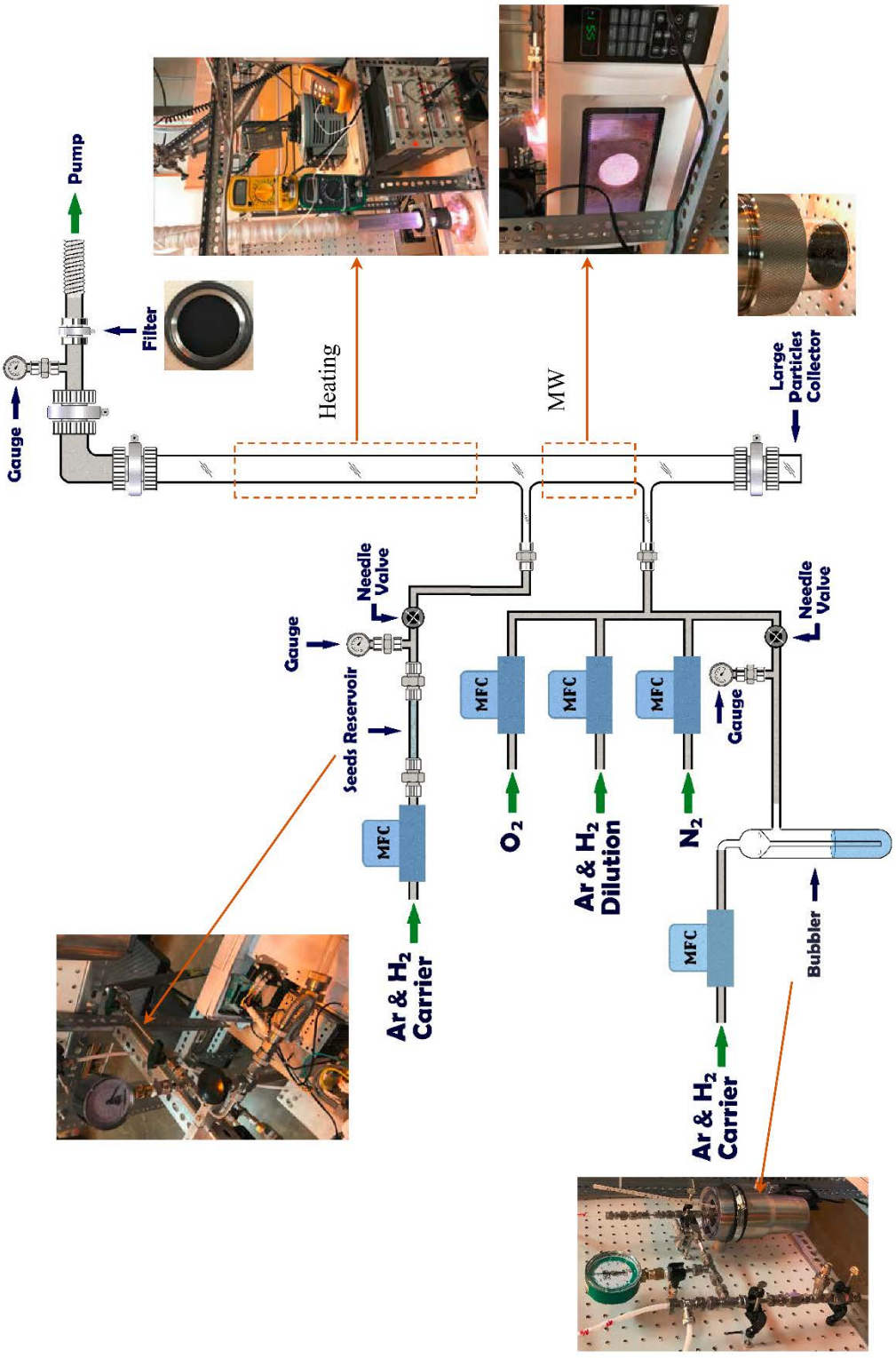

Figure 24: Schematic of the MW plasma discharge setup.

3.3. Gases laws and their calculations

Before dealing with the gas calculations that we made, it is necessary to give adequate explanations of some concepts. As illustrated in Figure 25, the volume of passed fluid per unit time is defined as volumetric flow rate which is denoted, sometimes by the symbol *Q*.

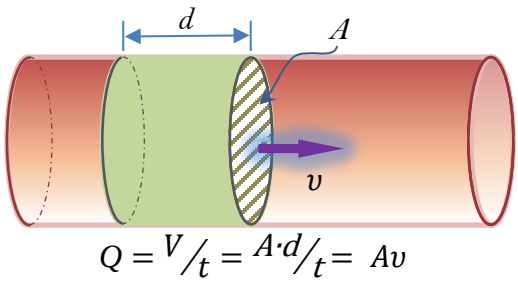

Figure 25: Fluid flow rate parameters.

Because of the confusion between the mass and volumetric flow rates, it is important to recognize their distinction. The mass flow rate is the mass of matter (e.g., molecules) which passes per unit time. Both mass and volumetric flow rates are variables per time and their units are *g/min* and cm^3/min respectively.

We know that the gas density is defined as

$$\rho = {}^{m}/_{V} \qquad (1)$$

Rewriting this equation in the form of mass flow rate ($\dot{m}$) and volumetric flow rate ($\dot{V}$ or *Q*) give the conversion equations

$$\dot{m} = \rho \cdot \dot{V} \quad \text{or} \qquad \dot{m} = \rho \cdot Q \tag{2}$$

One of the major dissimilarities between mass and volumetric flow rates is that the mass flow rate doesn't change (is constant) between the inlet (in) and outlet (out), while the volumetric flow rate and density (ρ) can be changed from inlet to outlet (see Figure 26). Thus, we might express the mass flow rates from inlet to outlet as

$$\dot{m}_{in} = \dot{m}_{out} \tag{3}$$

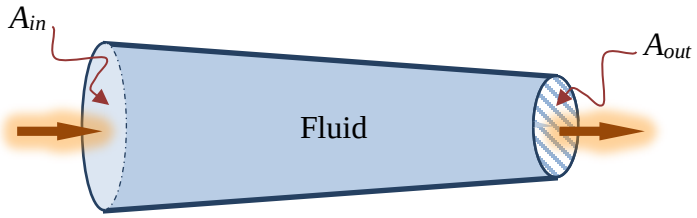

Figure 26: Flow rates and the equation of continuity.

If the fluid is incompressible, then

$$Q_{in} = Q_{out} \qquad \text{and} \qquad \rho_{in} = \rho_{out} \tag{4}$$

Since $Q = A\upsilon$, therefore, the equation of continuity can be derived as

$$A_{in} \cdot \upsilon_{in} = A_{out} \cdot \upsilon_{out}$$

In the case of a compressible fluid such as a gas,

$$\dot{m}_{in} = \dot{m}_{out} \qquad \text{yet} \qquad Q_{in} \neq Q_{out} \quad \text{and} \qquad \rho_{in} \neq \rho_{out} \tag{5}$$

and finally, the equation of continuity is

$$A_{in} \cdot v_{in} \cdot \rho_{in} = A_{out} \cdot v_{out} \cdot \rho_{out}$$

The ideal gas law is repeatedly expressed as

$$PV = nRT \tag{6}$$

Replacing the volume from Eq. (6) into Eq. (1) redefines the density gas as:

$$\rho = \frac{m\,P}{nRT} \tag{7}$$

Exchanging the value of *V* from Eq. (6) to Eq. (1) and then into Eq. (7). Thus, solving for $\dot{m}$ produces

$$\dot{m} = \frac{Q_{pre} \times P_s \times \mathcal{M}}{R \times T_s} \qquad where \quad \mathcal{M} = \frac{m}{n} \tag{8}$$

where *m* is mass (*g*), *n* is the number of moles (*mol*), and Q_{pre} is precursor volumetric flow rate (cm^3). $\mathcal{M}$ is the molecular weight (*g/mol*), and *R* is the gas constant [0.0821 *l·atm/(mol·K)* or 82.1 cm^3· *atm/(mol·K)*].

Most of the MFCs companies used the **NIST** (National Institute of Standards and Technology) system as standard conditions for temperature and pressure, where T_S = 293.15 *K* (20 °C) and P_S = 1 *atm* (760 Torr). Substituting the constants will lead to

$$\dot{m}\ (g/min) = \frac{Q_{pre} \times 1 \times \mathcal{M}}{[82.1 \times 293.15]}$$

$$\dot{m} = [4.155 \times 10^{-5}] \times Q_{pre} \times \mathcal{M} \qquad (g/min) \tag{9}$$

To calculate the residence time (τ) of the radicals inside the reactor, we start by dividing the ideal gas law [Eq. (6)] by τ which yields

$$P_s \frac{V_s}{\tau} = \frac{n}{\tau} R\, T_s \qquad \text{or,} \qquad P_s Q_s = \frac{n}{\tau} R\, T_s$$

Also, we can write

$$P \frac{V}{\tau} = \frac{n}{\tau} RT$$

From the last two equations,

$$\frac{V}{\tau} = \frac{P_s Q_s}{T_s} \cdot \frac{T}{P}$$

Then the residence time can be calculated from:

$$Residence\ time\ (\tau) = V. \left[Q_s \times \left(\frac{T}{T_s} \right) \times \left(\frac{P_s}{P} \right) \right]^{-1} \tag{10}$$

where Q_S is the volumetric flow rate expressed in standard conditions for temperature and pressure (P_S and T_S). P is the mean pressure, and T is the temperature of the reactor. The value of P_S and T_S are as mentioned previously.

From Eqs. (2) into Eq. (7), we obtain

$$\dot{m} = \frac{mP}{nRT} \cdot Q \tag{11}$$

According to Equations (5) and (11), the nonstandard volumetric flow rate can be calculated from standard volumetric flow rate by

$$Q = \frac{P_s \cdot T}{T_s \cdot P} \cdot Q_s \tag{12}$$

The mole fraction of the specified component (χ_i) is defined as the ratio of the number of moles of this component in a mixture (n_i), [expressed in moles], to the total number of moles present in that mixture (n_t), [expressed in moles].

$$\chi_i = {}^{n_i}/_{n_t}$$

For the ideal gas mixtures, the mole fraction

$$\chi_i = \frac{\dot{n}_i}{\dot{n}_t} = \frac{Q_i}{Q_t} = \frac{P^i}{P_t} \tag{13}$$

For the precursor and the carrier

$$\frac{P_v^i}{P_t} = \frac{Q_i}{Q_t^{i,c}} = \frac{Q_i}{Q_i + Q_c} \tag{14}$$

From the previous equation, we obtain

$$Q_i = \left[\frac{P_v^i}{P_t - P_v^i}\right] \cdot Q_c$$

Or as follows,

$$Q_i = \frac{P_v^i}{P_t} \cdot \frac{Q_c}{[1 - P_v^i/P_t]} \tag{15}$$

Through equations (13) and (15) we have that

$$\chi_i = \frac{Q_i}{Q_t} = \left\{\frac{P_v^i}{P_t} \cdot \frac{Q_c}{[1 - (Q_i/[Q_i + Q_c])]}\right\}\frac{1}{Q_t}$$

Finally, we get

$$\chi_i = \frac{P_v^i}{P_t} \cdot \frac{(Q_c + Q_i)}{Q_t} \tag{16}$$

where, χ_i: precursor mole fraction

$P_v{}^i$: precursor vapor pressure (Torr)

P_t: total pressure (Torr)

Q_c: carrier volumetric flow rate (sccm)

Q_i: precursor volumetric flow rate (sccm)

Q_t: total volumetric flow rate (sccm)

3.4. Adamantane and Dichloromethane vapor pressures

In the literature, there are different versions of vapor pressure formulas to calculate the vapor pressure for adamantane and dichloromethane. The selected equation commonly depends on which one is compatible or has a good agreement with the vaporization and the sublimation enthalpies data of the targeted hydrocarbon. In our work, we have chosen the most reliable equations that have been widely used in some data bases like **NIST** and some references such as refs. [73, 74].

For adamantane, we calculate the vapor pressure based on the following formula

$$ln(P_v/\text{kPa}) = A + B \cdot (T/\text{K})^{-1} + C \cdot ln(T/\text{K}) \quad (17)$$

whereas with the dichloromethane we have relied on

$$\log_{10}(P_v/\text{bar}) = A - \left[\frac{B}{(T/\text{K}) + C}\right] \quad (18)$$

where p_v is the vapor pressure, and A, B, and C coefficients' values are given in Table 3.

Coefficients	Adamantane [73, 74] [temperature range 254.0 - 543.0 K]	Dichloromethane [75] [temperature range 233.0 - 313.0 K][1]
A	50.9139	4.53691
B	– 8494.50	1327.016
C	– 4.6395	– 20.474

Table 3: Vapor pressure coefficients' values for adamantane and dichloromethane.

[1] Dichloromethane's coefficients have been calculated by NIST (National Institute of Standards and Technology) from author's data.

From equations (17) and (18), the diagrams of adamantane and dichloromethane vapor pressure vs. temperature can be calculated as in Figures 27 and 28.

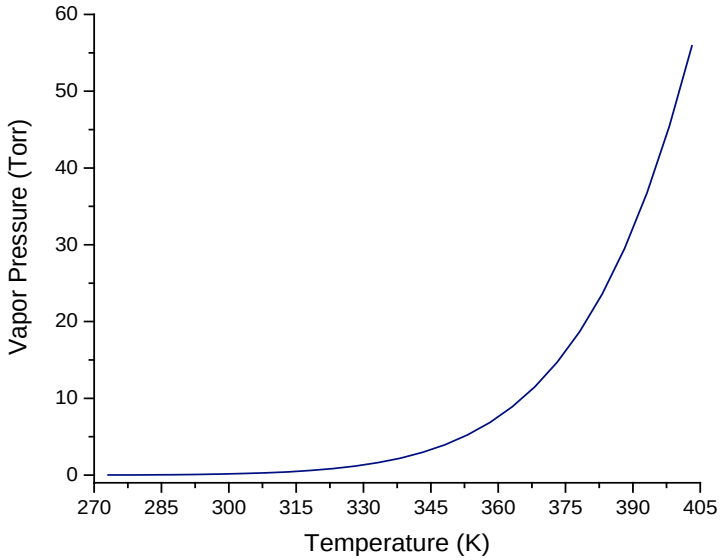

Figure 27: Vapor pressure vs. temperature diagram for adamantane

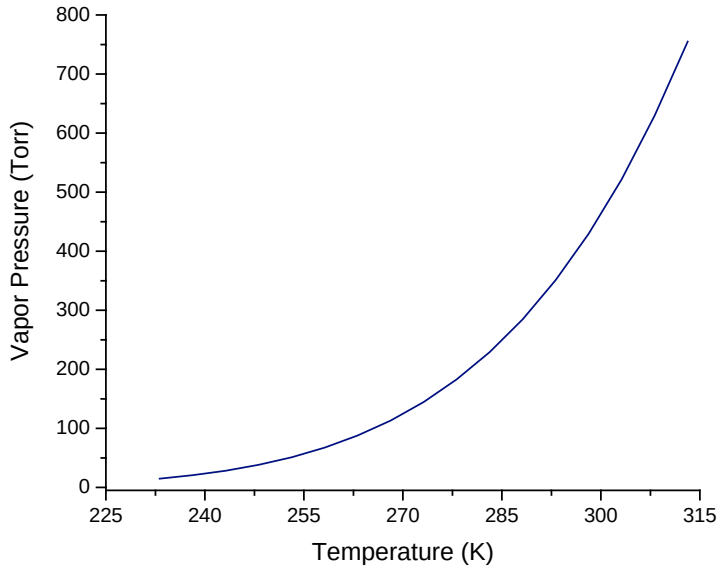

Figure 28: Vapor pressure vs. temperature diagram for dichloromethane

4. ENGINEERING OF FLUORESCENCE NANODIAMONDS

4.1. Introduction

Our experiments and the results will be discussed in detail in this chapter. We have divided our growth experiments into three stets (or categories). The first one was DC plasma discharge, as shown in Figure 20. It was the first attempt to grow nanodiamonds from the gas phase. Forming gas (H_2–Ar) with ratio H_2/Ar 5.3% was used. A 10 sccm of total flow rate (100 sccm) was utilized as a carrier of the adamantane ($C_{10}H_{16}$) and cyclohexane (C_6H_{12}) solution where the $C_{10}H_{16}$: C_6H_{12} ratio was 1:99. Due to the strong plasma sheath in the DC plasma discharge, no adamantane survived. A yellowish liquid material was collected on the filter and deposited on the electrodes and tubes. After this study, different types of plasma sources such as capacitively coupled RF and MW plasma discharges were proposed. The second set of experiments studied the sublimation of the adamantane without plasma which was focused on verifying the conditions to transfer the adamantane from the reservoir to the collecting position. The third set of experiments investigated temperature, pressure, carrier flow rate, and the distance between the adamantane's inlet point and the plasma were the targeted conditions with presence and absence of the plasma. From our previous experiments and studies, capacitively coupled RF and MW plasma discharges were chosen to be the stage of create radicals for nanodiamond growth. Various precursors, fuels, and seeds with diverse of flow rates, concentrations, temperatures, pressures, and powers were extensively studied and applied at this stage. Table 4 shows the experiments we have accomplished in the present work.

	Plasma type	Reactants (gases, liquids) and Seeds
1	No plasma	$C_{10}H_{16}$ (Adamantane) [*Sublimation experiments*]
2	Capacitively coupled RF plasma discharge	$Ar + CH_4 + CO_2$
3		$Ar + CH_4 + H_2$
4		$Ar + CH_2Cl_2$ (Dichloromethane) + H_2
5		$Ar + CH_2Cl_2 + O_2$
6		$Ar + C_{10}H_{16} + H_2$
7		$Ar + C_{10}H_{16} + CH_4$
8		$Ar + C_{10}H_{16} + CH_4 + H_2$
9		$Ar + C_{10}H_{16} + CO_2 + CH_4$
10		$Ar + SiH_4$ (Silane)
11		$Ar + SiH_4 + H_2$
12		$Ar + SiH_4 + CH_4 + H_2$
13	MW plasma discharge	$CH_2Cl_2 + [Ar/H_2]$
14		$CH_2Cl_2 + N_2 + [Ar/H_2]$
15		$CH_2Cl_2 + C_6H_{15}N$ (Triethylamine) + $[Ar/H_2]$

Table 4: Outline of our experiments in the present work.

4.2. Our engineering concepts

Initially we aimed to self-nucleate nanodiamonds from the gas phase homogeneously useing low-weight hydrocarbon compounds such as methane and dichloromethane as a carbon source. The vast majority prior research, based on CVD

growth, used a high concentration of hydrogen in the gaseous mixture during the synthesizing of Micro- and Nano-crystalline diamonds and thin-film nanodiamonds. The reason for the usage of hydrogen is due to its ability to etch the sp^2 carbon bonds leaving only sp^3 [76]. However, it proved easier in the literature to grow diamonds by starting with halogenated hydrocarbons such as dichloromethane and chloroform as sources of carbon and chlorine. Some studies indicated that the diamond nucleation density was enhanced when the halogenated hydrocarbons was present, for example see Refs. [60, 77]. Chlorine was much more capable of etching the sp^2 hybridized bond than the hydrogen.

A number of concepts or layout were suggested for our experiments. Foremost among them was to run capacitively coupled RF plasma discharge experiments as illustrated in Figure 29. These were studied comprehensively in the literature. The theoretical parameters such as plasma power and processors' concentrations and flow rates on the diamond production rate were one facet of these studies. Based on the theoretical study, a plan was proposed to run the experiments. The main carbon source was methane (CH_4), and argon plasma that was induced with an RF generator. In other studies O_2, CO_2, and CH_2Cl_2 (dichloromethane), for instance, were used to nucleate diamonds [63]. Thus, we also used these materials under a variety of conditions. Adamantane and silane (SiH_4) were also employed as diamond seed molecules.

The second approach was to use MW plasma discharge. From the previous results (i.e., RF plasma), we chose to utilize CH_2Cl_2 as a carbon source and $C_6H_{15}N$ (triethylamine) as a nitrogen source to make NV centers. We switched to MW plasma due to its predicted thinner plasma sheath. An assortment of diamond-like seed molecules such

as adamantane, 1-Adamantylamine ($C_{10}H_{17}N$), and AZADO (2-Azaadamantane-N-oxyl, $C_9H_{14}NO$) were proposed. Figure 30 demonstrates the fundamental principle of this concept.

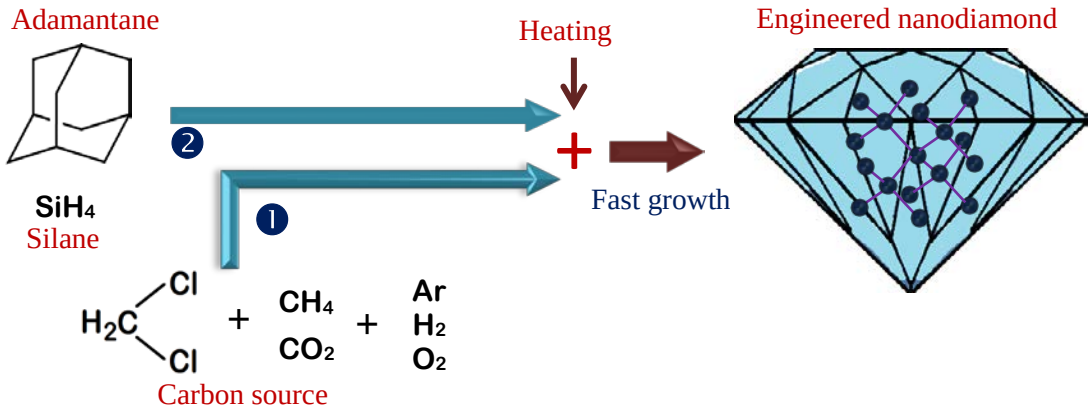

Figure 29: RF plasma discharge engineering concept.

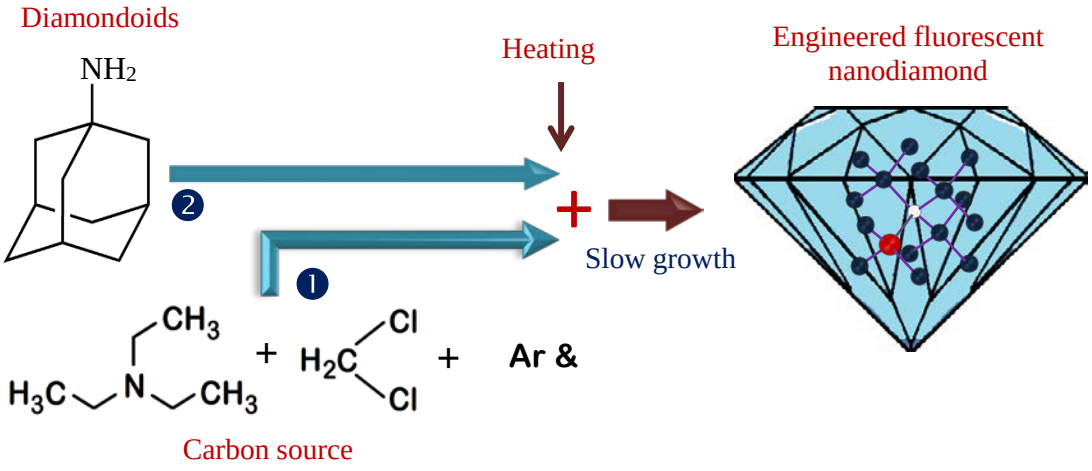

Figure 30: MW plasma discharge engineering concept.

4.3. Experimental works

Adamantane sublimation and Rf plasma discharge experiments were conducted with two small horizontal reactors (tubes). The first one was a straight tube where the gaseous mixture (diamond precursor) and the seeds pass through the plasma region. The second design was a T-shaped where the diamond precursor passes through the plasma while the seed inlet was after-glow. The inner diameter of both configurations was 7 mm and both were around 35 cm in length which made the radicals' residence time very short (< 250 ms). The electrodes in these designs were chosen to be out of the plasma reactor to avoid contamination and to prevent the plasma from etching the electrodes. Figure 31 (a) and (b) exhibits the schematics of the reactors configurations. The MW plasma discharge system was engineered to be vertical (> 2 m) with 46 mm diameter reaction tube to make the radicals' residence time on order of a second, as shoun in Figure 24.

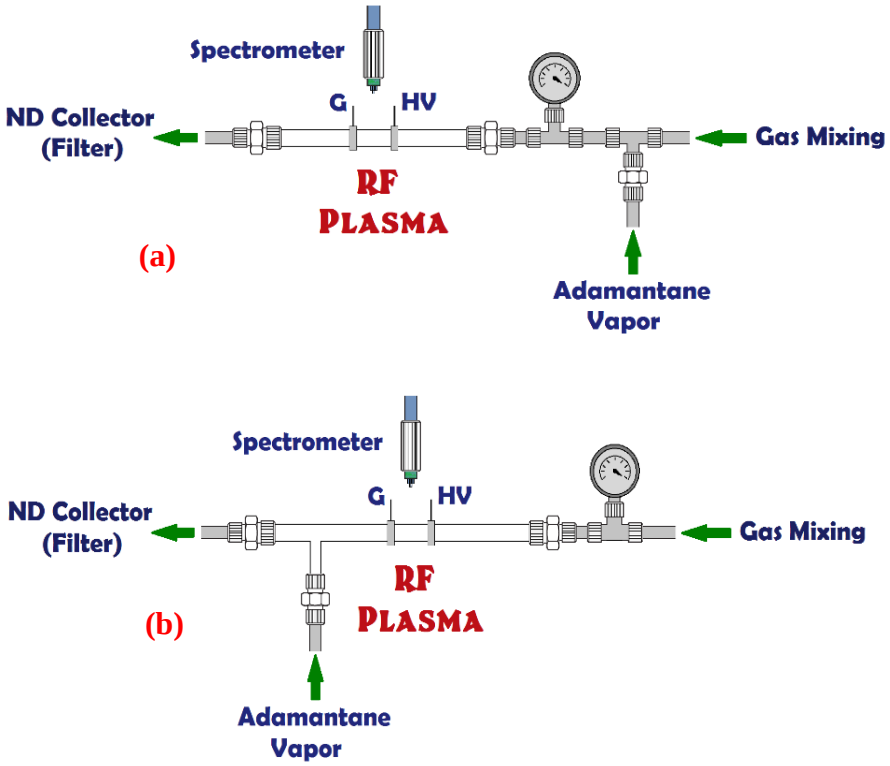

Figure 31: Schematics of the straight-tube (a) and T-shaped (b) configurations.

4.3.1. Adamantane sublimation experiments:

In these experiments, the sublimation and re-collection of adamantane was examined with and without plasma. The major aim was to carry the adamantane (seed) from the reservoir to the collecting position (filter) with no molecular dissociation either in the plasma or deposition on the lines before reaching the filter.

4.3.1.1. Straight-tube reactor

In the absence of plasma, everal experiments were done under dissimilar conditions of pressures, temperatures, and flow rates. For instance, one of the experiments' conditions was Ar carrier at a flow rate 25 sccm and reactor pressure 20 Torr. Also, the

adamantane's pressure, temperature, volumetric and mass flow rates were 51 Torr, 50 °C, 0.422sccm, and 140.97mg/h respectively. The reaction lines temperature (i.e., downstream) was ~ 80 °C. The reactor design and conditions were confirmed to transfer the adamantane from reservoir to the filter, as shown in Figure 32.

Figure 32: The collected adamantane on the filter.

The Raman spectrum of the collected adamantane was taken and compared with the fresh adamantane, and found to be identical (see Figure 33). Si peak in the spectra came from the silicon wafer that was used as a substrate to measure the Raman spectra.

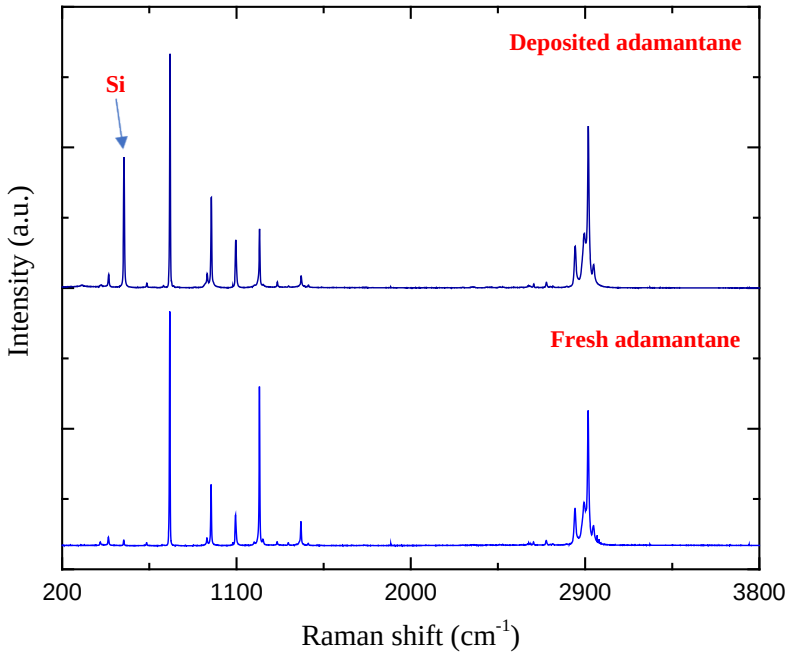

Figure 33: Raman spectra of the fresh and deposited adamantane.

However, *in the case of plasma discharge* and under otherwise the same conditions the adamantane didn't survive, as displayed in Figure 34. Here the RF plasma power was 20 W. The collected materials were clumpy and brownish flakes. In addition a film was formed on the inner surface of the reactor (quartz tube) between the electrodes. Thus, the Adamantane dissociated after passing through the plasma, converting into a brown powder which appears to be composed of some elemental carbon along with the organic material. Raman spectra, as presented in Figure 35, indicates the appearance of D and G bands but the signature peaks of adamantane disappeared. Figure 36 is the optical emission spectrum (OES) of one of the attempts where the adamantane mass flow rate was 15.7 mg/h. A minor leak in the system or impurities in the gases might explain the existence of nitrogen

in the OES. The dissociation of the adamantane can be clearly distinguished due to the presence of C_2, CH, and CN molecules and H_α atom peaks.

Figure 34: The collected material when the adamantane passes through the plasma.

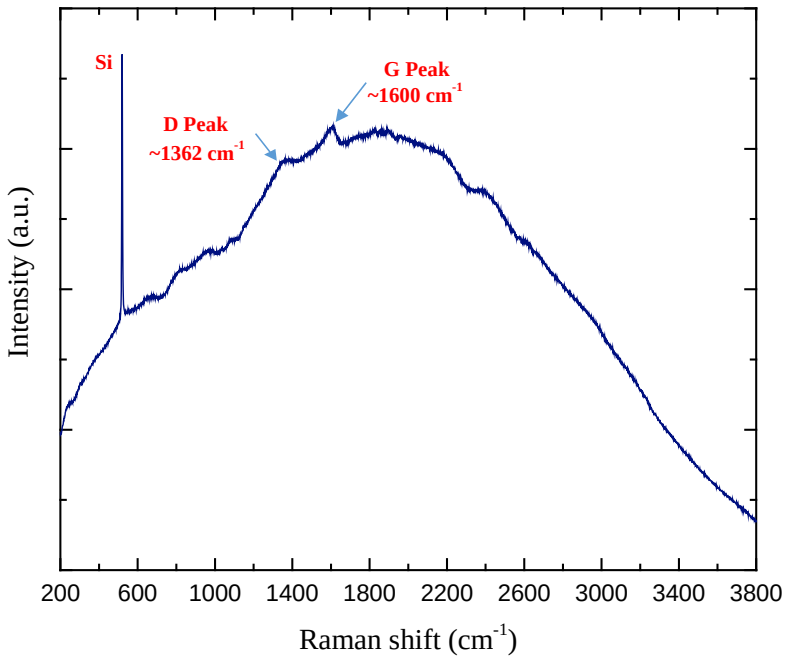

Figure 35: Raman spectrum of the deposited material.

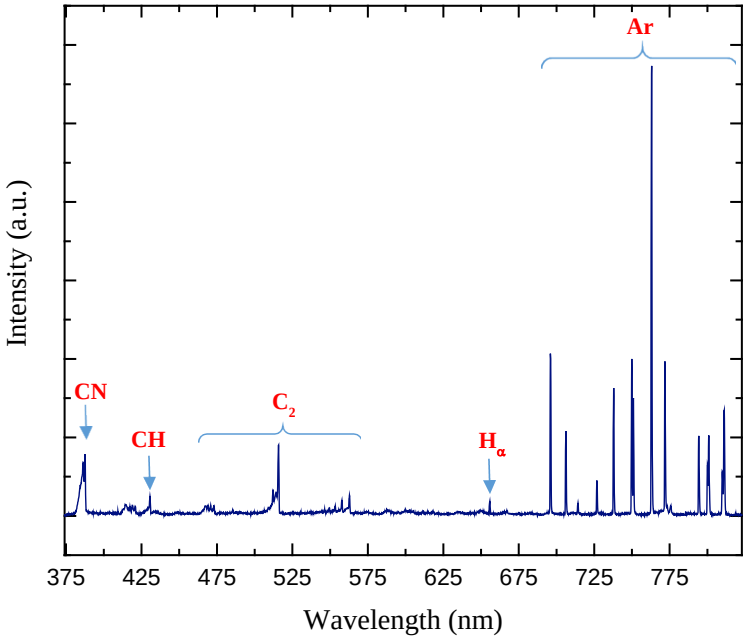

Figure 36: OES of the plasma.

After some more unsuccessful attempts, it was suggested to add some additional gas or another precursor to reduce adamantane decomposition. Hydrogen, methane, and carbon dioxide were the candidates investigated to achieve the goal. Under 20 W RF power, 130.14 mg/h adamantane mass flow rate, and ~25 Torr reactor pressure, two growth attempts with different H_2 and Ar carrier flow rates were attempted as shown in Figure 37. The hydrogen suppressed the creation of solid particles but an oily yellowish liquid formed instead. Furthermore, there was no deposited adamantane on the filter with the plasma on. As we will subsequently find, comparable phenomena occurred when adamantane is mixed with CH_4 and CO_2. All the experiments proved that adamantane cannot survive in this configuration.

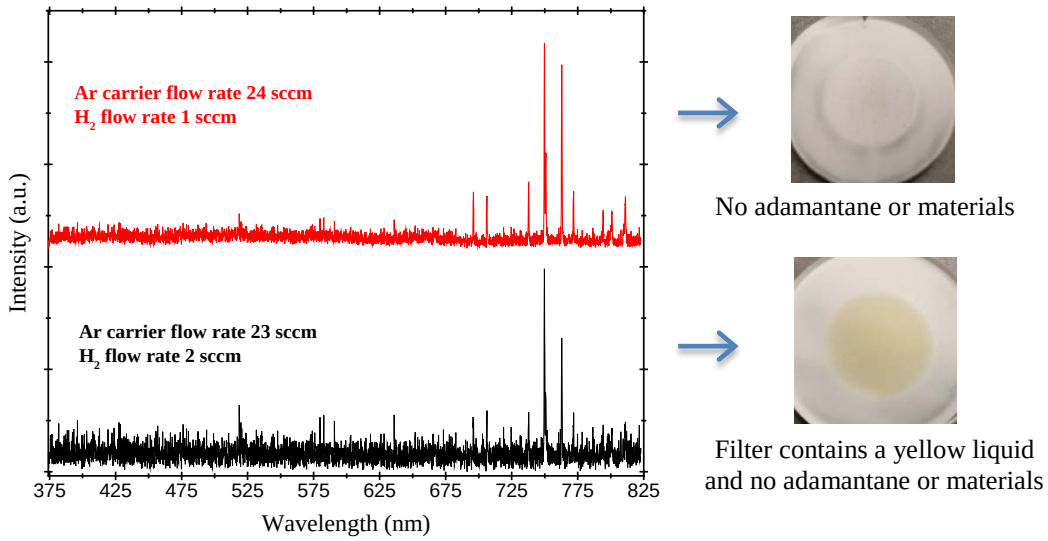

Figure 37: OES of the plasma after adding H_2 to the adamantane sublimation and photos of the collected material on the filters.

4.3.1.2. T-shaped reactor

Since the adamantane molecules were broken down after passing the plasma region, a new quartz reactor (T-shaped) was built. The major change in the suggested design was moving the adamantane's inlet downstream to the tail of the plasma. Figure 38 displays photos of the new reactor. The purpose of this design was to give the adamantane molecules contact with carbon radicals without exposing the adamantane to the plasma hot zone. Several experiments were run under various conditions. The volumetric flow rates, adamantane mass flow rate, and the downstream pressure were fixed. The common conditions of the experiments were: Ar carrier flow rate, 40 sccm; Ar dilution, 10 sccm; reactor pressure, 20 Torr; adamantane mass flow rate, 230 mg/h. Introducing the adamantane through the T-branch didn't affect the measurements of the OES (see Figure 39).

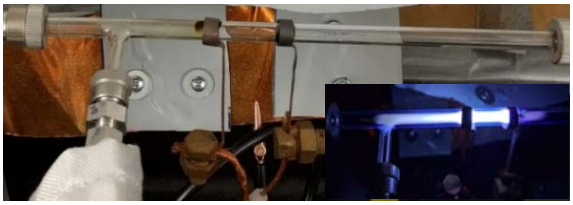

Figure 38: T-shaped reactor.

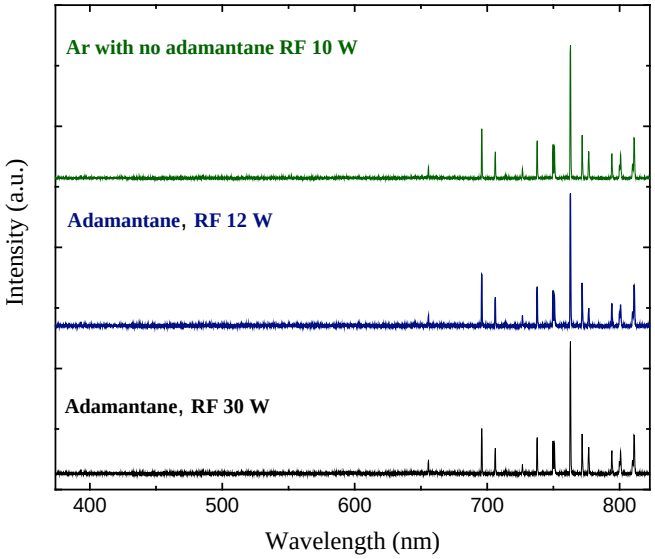

Figure 39: OES spectra in the T-shaped reactor at different RF powers.

At the conditions listed earlier, the plasma still appears to decompose some of the adamantane in this design but not in the same way as before; no solid material (except adamantane) is produced, and most of the adamantane remains intact. At 30 W applied power the product appears grainier and slightly off-yellow. This likely indicates a partial decomposition of the adamantane into other condensed species. The Raman spectra of the samples, as shown in Figure 40, seems to be dominated by signals roughly indistinguishable from adamantane.

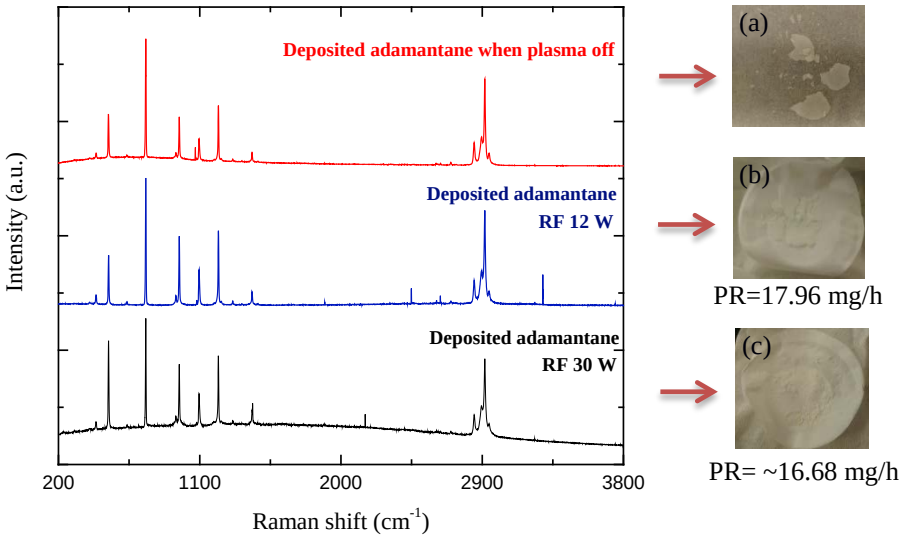

Figure 40: Raman spectra of the collected materials (where PR: production rate).

4.3.2. Capacitively coupled RF plasma discharge experiments:

For the purpose of the present discussion, it is sufficient to focus on some experiments for characterizing the fabricated material and understanding the nucleation mechanisms.

4.3.2.1. T-shaped reactor

After our favorable outcome using the T-shaped configuration with adamantane in Ar plasma experiments, further investigations were carried out at diverse conditions and gaseous mixture. The adamantane was mixed with CH_4, H_2, and CO_2 under similar volumetric flow rates (0.5 sccm), adamantane mass flow rate (~ 143 mg/h), downstream pressure (i.e., reactor pressure) (20 Torr), and RF power (50 W). The remaining conditions of each experiment depended on the details of the gaseous mixtures. The first run was performed under the following conditions: Ar dilution and carrier volumetric flow rates were 24.5 sccm and 25 sccm respectively. As a probe excited state species, OES plasma

spectra from the first run (see Figure 41) indicated the similarities of the spectrums with and without the presence of the adamantane. Also, the measured C_2/Ar, H_α/Ar, and CH/Ar peaks ratios approximately matched.

After growth, air oxidation was used first. In the air oxidation recipe the samples were heated to 550 °C for 10 min in air, as already described in Section 3.2.2 (see Figure 14).

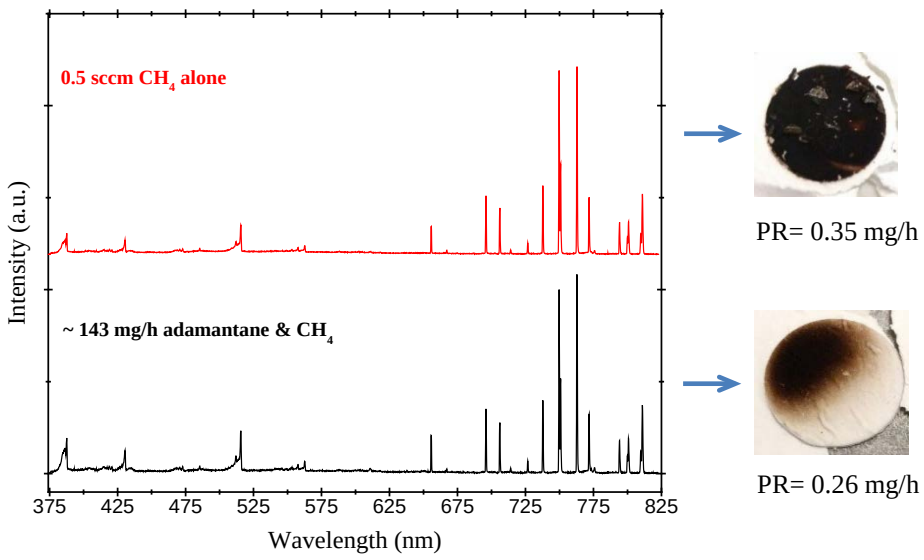

Figure 41: OES spectra of the plasma.

Raman spectra were taken before and after the oxidation of all the collected materials. Figures 42 and 43 illustrate the Raman spectra of the experiments mentioned earlier (i.e., in Figure 41) while Figure 44 shows the Raman spectra after adding H_2 to the gaseous mixture. Injecting the adamantane farther downstream from the plasma rather

than just outside of it has a much stronger impact on material morphology and production rate. In the case when the adamantane produces a mixture of solid and liquid compositions, it may be a partial conversion of adamantane into terpenes or other similar molecules. After air oxidation the final outcome is nearly indistinguishable Raman spectra. Overall, both pre-oxidized and oxidized samples' give essentially the same Raman spectra independent of the injection point of the adamantane. In all spectra, the G peak stayed almost at the same wavenumbers whereas the D peak shifted to higher wavenumbers under some conditions.

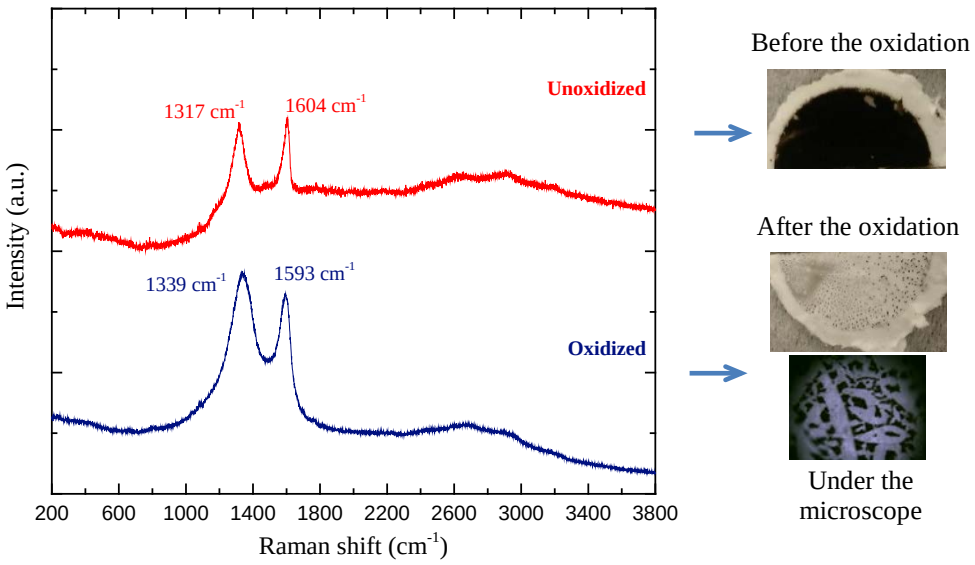

Figure 42: Raman spectra of the samples with the absence of adamantane (only CH_4).

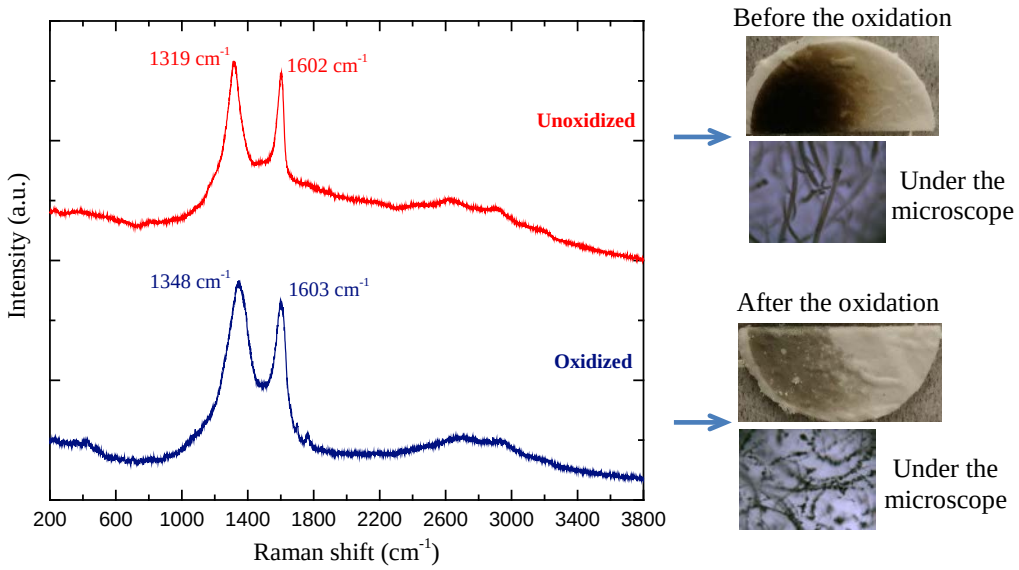

Figure 43: Raman spectra of the samples with the presence of the adamantane (~ 143 mg/h) and CH_4.

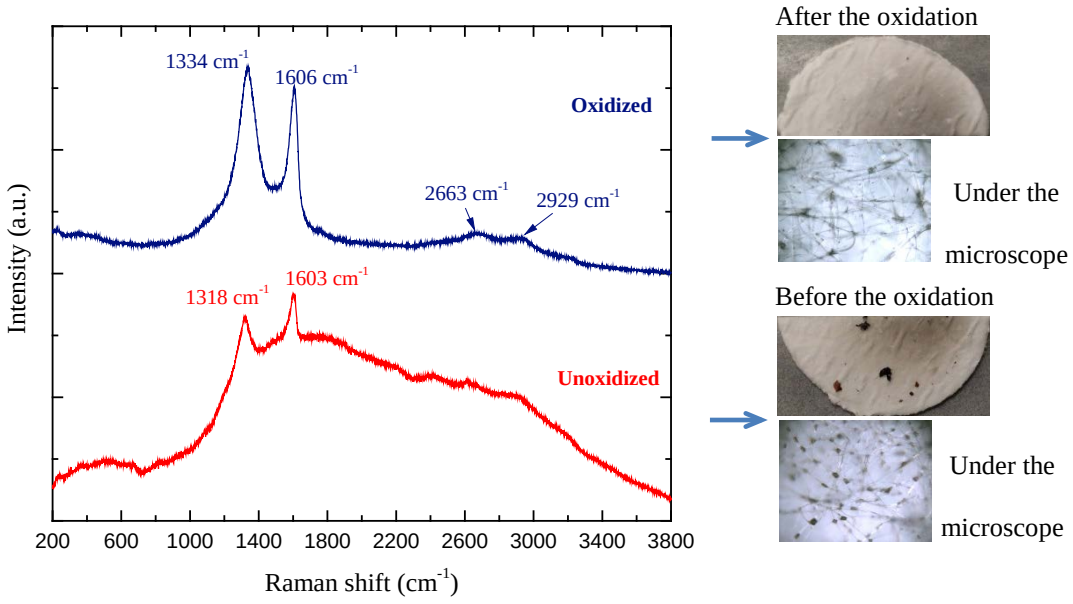

Figure 44: Raman spectra of the samples with the presence of the adamantane (~ 143 mg/h), CH_4, and H_2.

As shown in Figure 44 in the case of combining H_2, CH_4, and adamantane, two bands appeared at 2663 and 2929 cm^{-1} wavenumbers. The bands may be the second order (two-phonon) Raman D-line (2D) and the higher order (G + D) bands respectively [78]. Since nanodiamonds were not observed in these samples even with the intensive purification, it is likely that these conditions are not favorable. Nonetheless, an improvement on this T-shaped design is proposed in Section 3.2.6. But this new design was not implemented.

4.3.2.2. Straight-tube reactor

Measuring the plasma temperature isn't a simple task with this reactor since the gaseous mixture has a variety of complexes and atoms and produces many products. Thus, we proposed a method to help giving an estimated value (imprecise assessment) of the plasma temperature by applying a non-contact temperature measurement technique like a thermal imaging camera and a laser infrared thermometer (see Figures 45 and 46). Even with the low temperature limitation of the thermal imaging camera we used (270°C), which is much less than plasma temperature, this device was very helpful in showing a perspective of the plasma temperature distribution. The advantages of the laser infrared thermometer are that it has a wider range of temperature measurement and direct access to the temperature data during the experiments. In the straight-tube reactor configuration, CH4/H2, DCM/H2, DCM/O2, and CH4/H2/SiH4 under various conditions will be discussed. As long as the adamantane does not affect the plasma conditions, we can compare gas-phase nucleation with and without the presence of nanodiamond seeds.

Exp. conditions
75W, 48.75 sccm Ar dilution
0.25 sccm CH_4, 1 sccm H_2, and
the plasma volume 3.58 cm^3

Exp. conditions
100W, 48.50 sccm Ar dilution
0.25 sccm CH_4, 1.25 sccm H_2, and
the plasma volume 3.66 cm^3

Exp. conditions
250w, 48 sccm Ar dilution
0.25 sccm CH_4, 1.75 sccm H_2, and
the plasma volume 8.47 cm^3

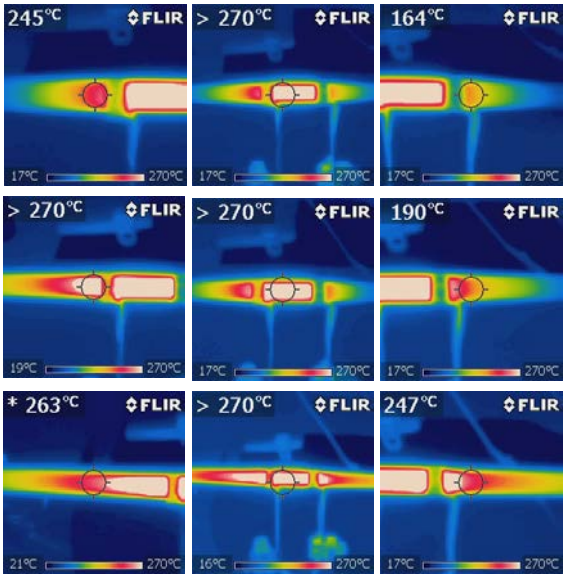

Figure 45: Thermal imaging of the plasma for three experiments under various conditions.

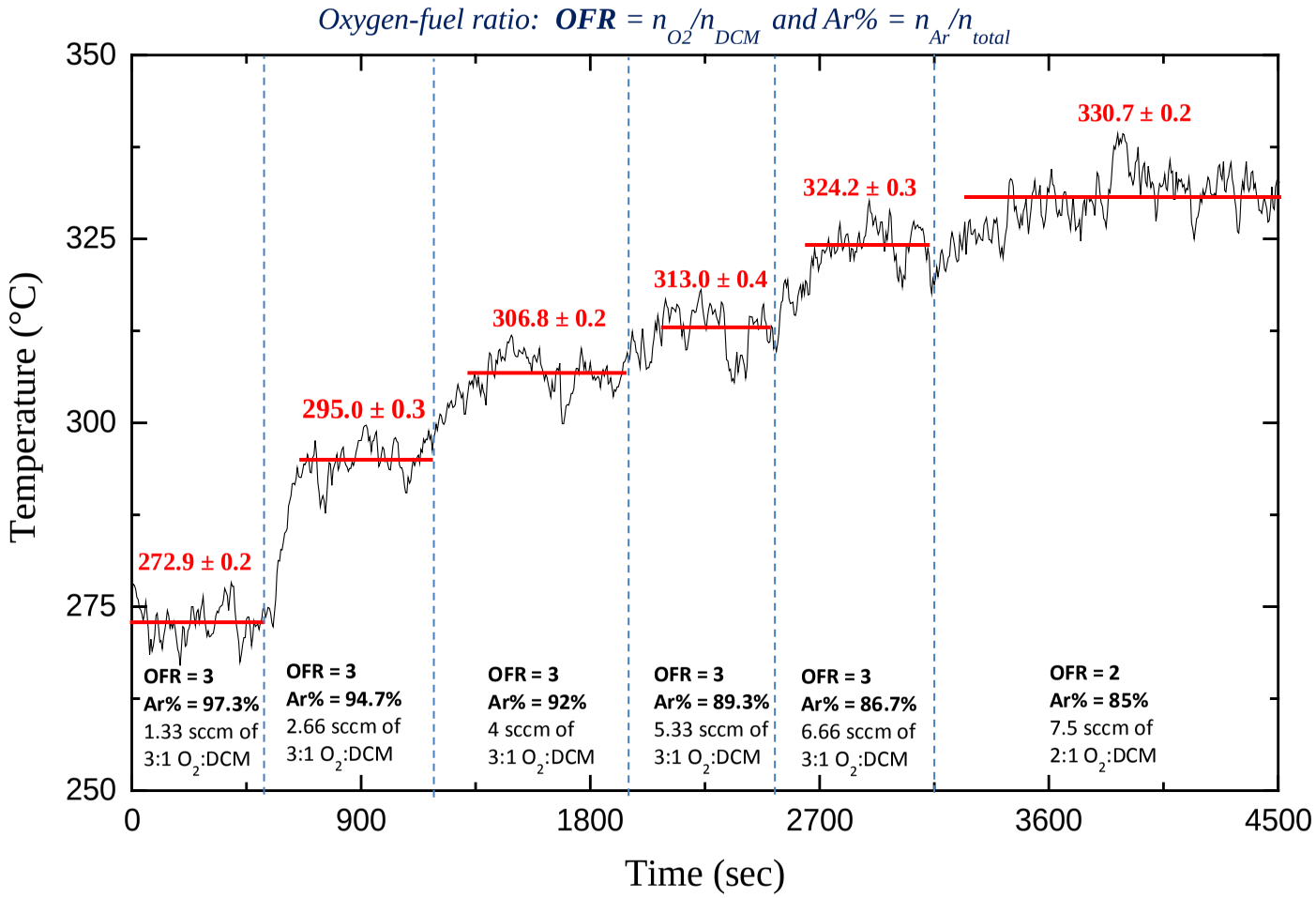

Figure 46: Laser infrared thermometer readout for several experiments.

4.3.2.2.1. CH_4/H_2 study

In the literature, the CH_4/ H_2 mixture was the most common ingredient in the growth of nanodiamonds and diamond thin films with chemical vapor deposition regardless of the use of heat or the plasma to produce radicals. Because of the significance of this mixture we performed experiments with various operating conditions as outlined in Table 5.

The common conditions: reactor pressure 50 Torr and the run time 2 hours

Exp.	Flow rate		Ratio	Ar dilution	Power	Plasma	Production	Residence time
	CH_4	H_2	CH_4:H_2	(sccm)	(W)	Volume (cm^3)	rate (mg/h)	(ms) [approx.]
①	0.25	0.75	1:3	49	75	3.66	0.60	≤150
②	0.25	1	1:4	48.75	75	3.58	0.07	
③	0.25	1.25	1:5	48.50	100	3.66	0.055	≤170
④	0.50	0.50	1:1	49	50	3.08	0.77	≤100
⑤	0.25	0.75	1:3	49		3.27	0.07	
⑥	0.25	1.75	1:7	48		3.08	NA	
⑦	0.50	0.50	1:1	49	150	5.77	2.55	≤200
⑧	0.25	0.75	1:3	49		6.93	0.71	
⑨	0.25	1.75	1:7	48		5.77	NA	
⑩	0.50	0.50	1:1	49	250	8.08	1.28	≤300
⑪	0.25	0.75	1:3	49		10.4	0.05	
⑫	0.25	1.75	1:7	48		9.62	0.02	

Table 5: Outline of CH_4/H_2 experiments.

Figure 47 presents the experiments 1 through 3 under diverse conditions. Deconvolution of the Raman spectrum of one of the experiments into constituent Lorentzian peaks: D, G, 2D, G+D, 2D' is illustrated in Figure 48. The conditions of the experiment were: RF power, 250 W; Ar dilution, 48 sccm; CH_4 flow rate, 0.25 sccm; H_2 flow rate, 1.75 sccm; downstream pressure, 50 Torr. Due to the presence of G and D' band coupling, they cannot be separated by applying Lorentzian or Gaussians functions. However, D' can be fitted with the Breit-Wigner-Fano (BWF) line shape function instead.

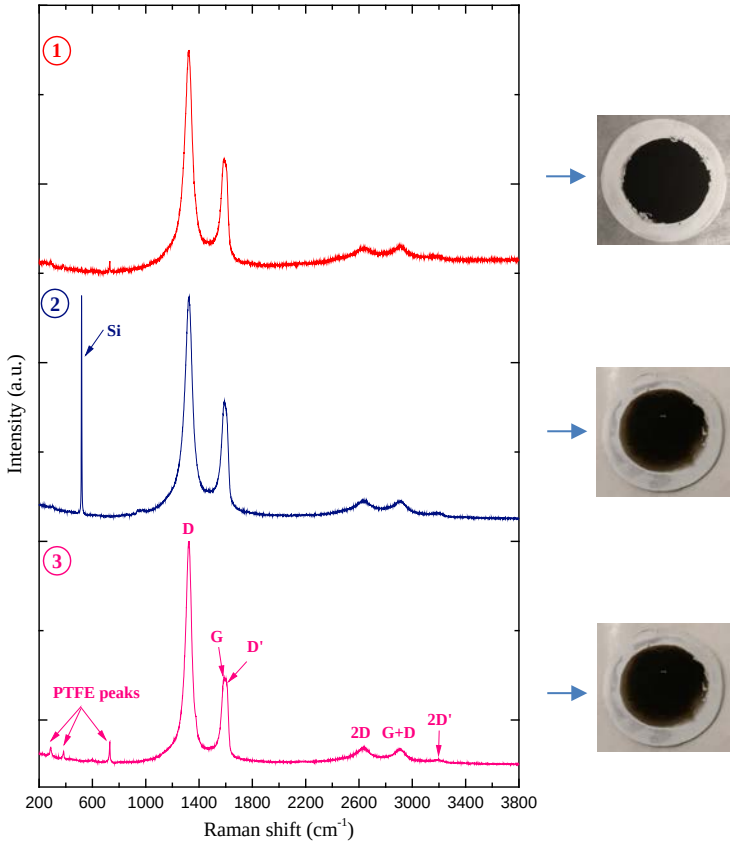

Figure 47: Raman spectra of CH_4/H_2 mixtures samples at different ratios, powers, and dilutions (for the experiments' conditions see Table 6).

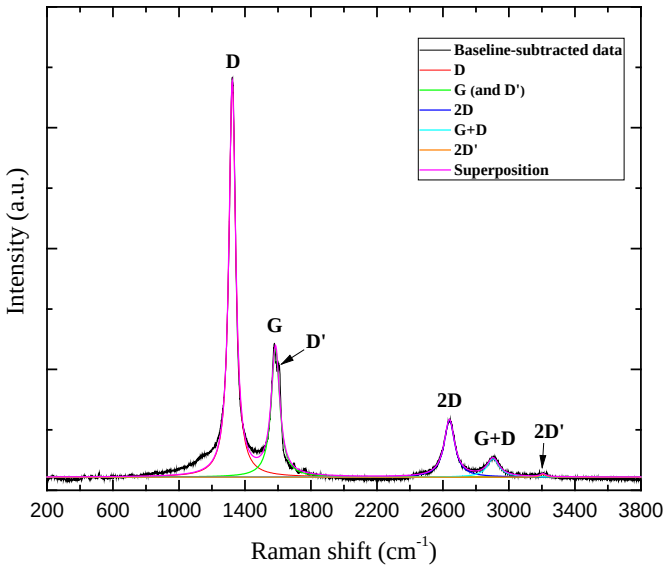

Figure 48: Raman spectrum deconvolution of one of the samples.

From Figures 49, 50, and 51, the combination of H_2 concentration and the reactor's power played dominant roles in the production rates of particles and also played a significant role in material morphology. Higher power and higher H_2/CH_4 ratio both tended to increase I(D)/I(G) and I(2D)/I(G) and decrease FWHM(D). Particularly, I(2D)/I(G), FWHM(D), and G position measures pointed to more ordered graphitic crystallinity than amorphous carbon as H_2 increased [79-81]. In general, accurate measurement G band (i.e., at the higher H_2/CH_4 ratio and 250 W) was confounded by the presence of the D' band. D' is associated particularly with vacancy disorders (as opposed to sp^3 disorders). In general, the G+D band also reflects the concentration of defects. It can clearly be observed only when the concentration of defects is high [78, 82-85].

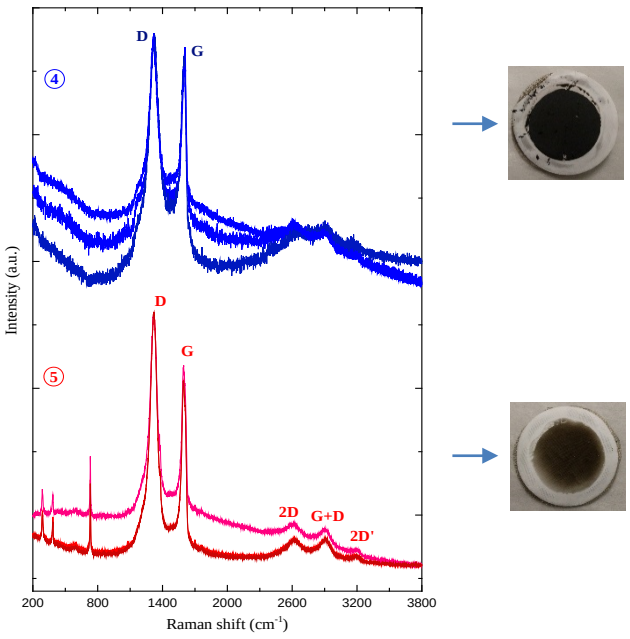

Figure 49: Raman spectra of three spots on the CH_4/H_2 mixtures filters [RF power: 50 W] (for the experiments' conditions see Table 6).

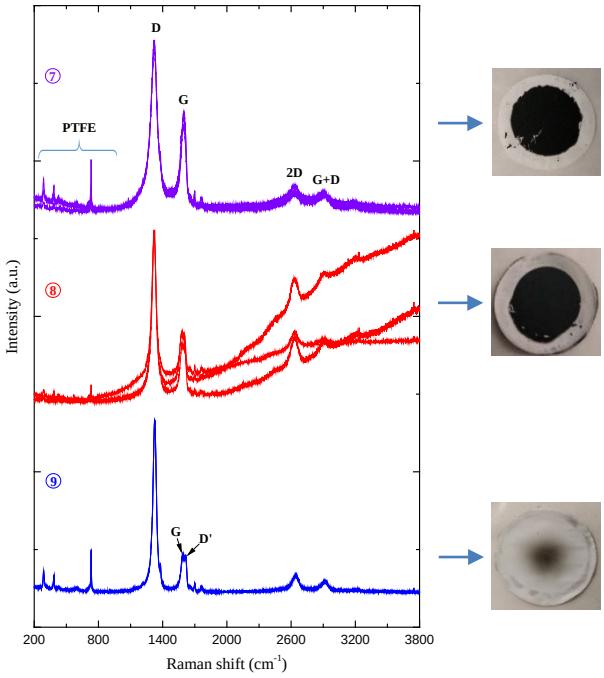

Figure 50: Raman spectra of three spots on the CH_4/H_2 mixtures filters [RF power: 150 W] (for the experiments' conditions see Table 6).

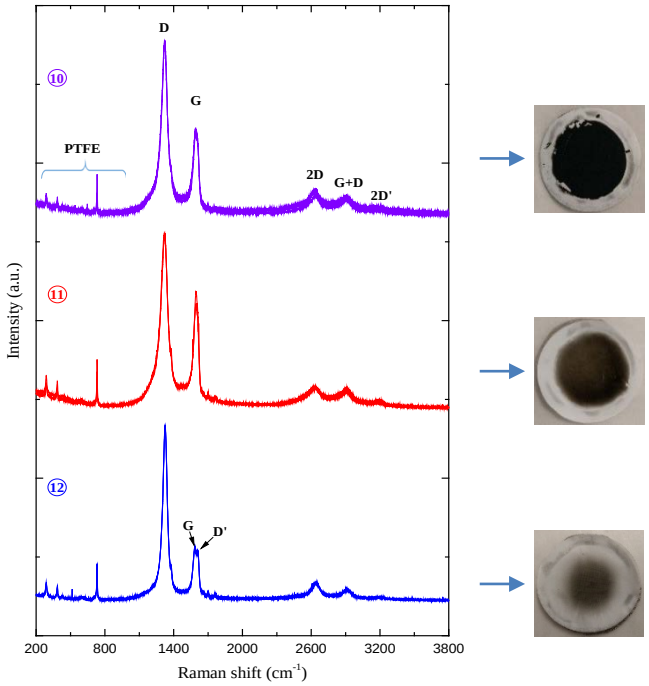

Figure 51: Raman spectra of three spots on the CH_4/H_2 mixtures filters [RF power: 250 W] (for the experiments' conditions see Table 6).

Raising the plasma power while retaining CH_4/H_2 concentrations (i.e., precursor flow rates) constantly brings forth substantially greater particle formation. This may open up the possibility of nucleating more material at higher H_2 content relative to CH_4. FWHM(D) and I(D)/I(G) seem to display the most consistent trends in the Raman spectra when increasing H_2 concentration as demonstrated in Figure 52 (b) and (d). In the TEM photos, the FWHM(D) is seen to be a reliable indicator of crystallinity; namely in 1:1[CH_4:H_2] at plasma powers of 50W(a) and 250 W (b) FWHM(D) was 135 cm^{-1} and 70 cm^{-1}, respectively. Additionally, the presence of the lattice spacings in the samples was confirmed for higher I(D)/I(G) ratios and the particles looked hollow with an onion-like exterior (see Figure 53).

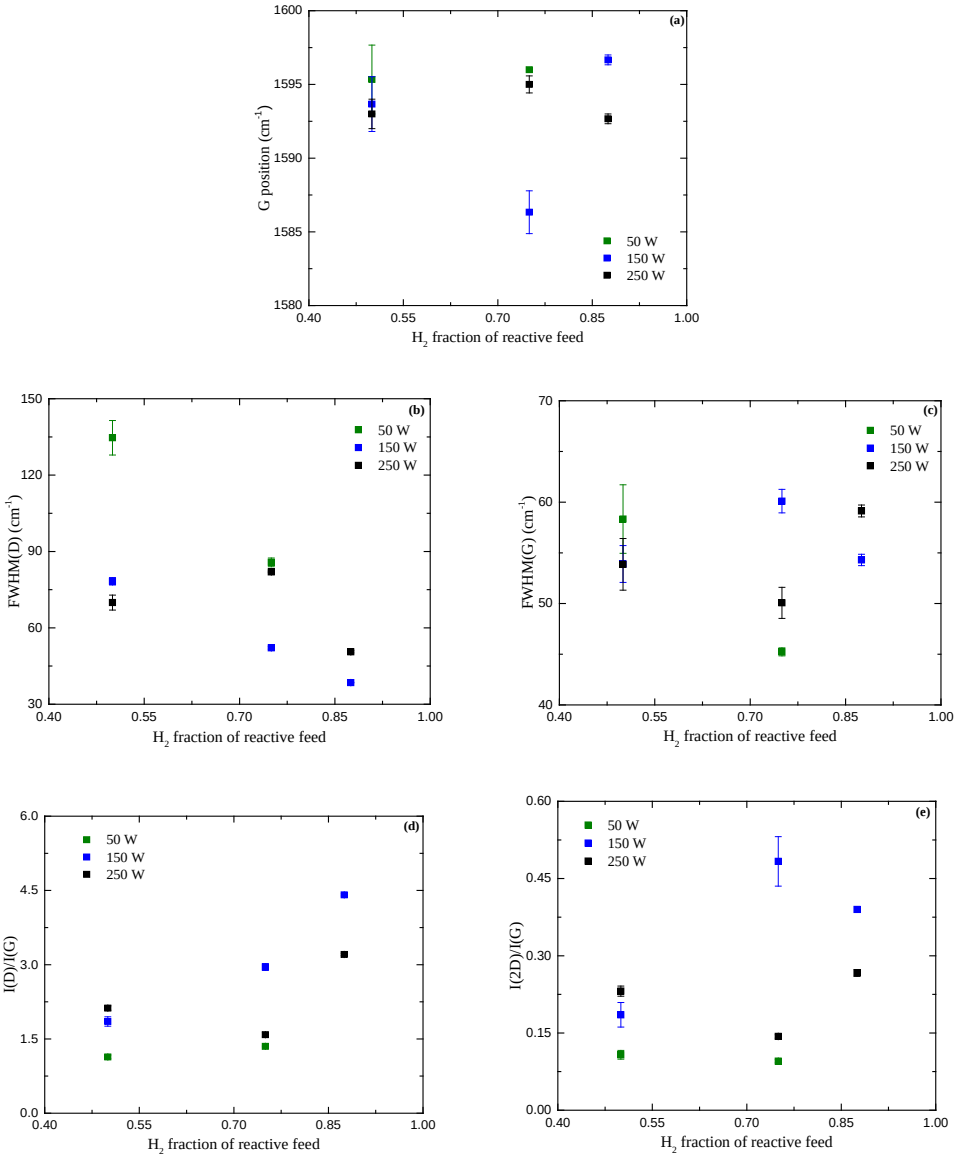

Figure 52: The trends in Raman spectra of the CH_4/H_2 mixtures filters [experiments 4 through 12] (for the experiments' conditions see Table 6).

The H_2 fraction of reactive feed was calculated based on the following equation:

$$H_2\ fraction\ of\ reactive\ feed = \frac{H_2}{H_2 + CH_4} \tag{19}$$

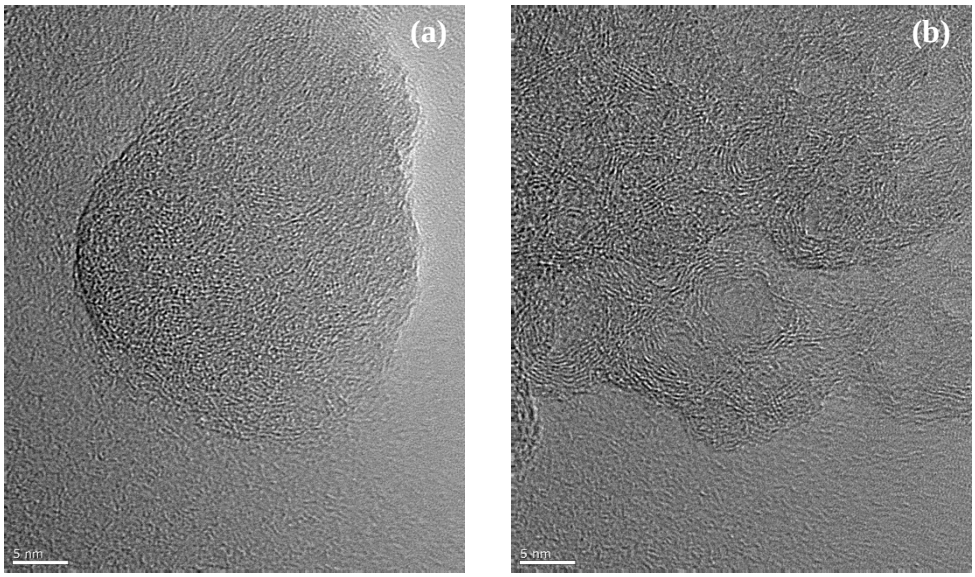

Figure 53: TEM photos of 1:1[CH_4:H_2] ratio at (a) 50W and (b) 250 W (for the experiments' conditions see Table 6) (500kx Mag.) [Scale bar, 5 nm].

4.3.2.2.2. DCM/H_2 study

Chlorinated hydrocarbons such as dichloromethane and trichloroethylene were employed in synthesizing diamond [60, 86-89]. In this study and the next one, dichloromethane with hydrogen and oxygen additives, respectively, will be discussed.

Table **6** outlines of selected DCM/H_2 experiments performed under dissimilar conditions.

In this study, the plasma optical emission spectra (OES) were shown to have a more or less consistent trend with H_2 addition and increasing power, and both contributed to a higher relative population of H atoms with respect to C_2. This was in contrast to CH_4/H_2 mixtures results which were discussed in the prior study (i.e., Section 4.3.2.2.1).

In the tendency of C_2/H_α ratio, Figure 54 (d), equation (19) was used to calculate the H_2 fraction of reactive feed. Increasing the concentration of H atoms while maintaining a constant flow rate of the carbon source raised the intensity of H_α emissions, producing more CH radicals, and suppressing the formation of C_2 radicals which increased the chance of growing nanodiamonds (see Figure 54).

The common conditions: reactor pressure 50 Torr and the bath temperature – 10°C

Experiment		①	②	③	④	⑤	⑥	⑦	⑧	⑨
Flow rate (sccm)	DCM	0.1								
	H_2	1	1.5	2	1	1.5	2	1	1.5	2
Ratio	DCM:H_2	1:10	1:15	1:20	1:10	1:15	1:20	1:10	1:15	1:20
Ar dilution (sccm)		48.54	48.05	47.54	48.54	48.05	47.54	48.54	48.05	47.54
Power (W)		50			150			250		
Plasma Volume (cm^3)		2.98	2.70	2.89	4.23	4.04	5.77	5.20	5.77	7.31
Production rate (mg/h)		0.75	1.33	NA	1.52	2.04	NA	1.90	0.48	NA
Residence time (ms) [approx.]		≈ 100			≈ 150		≈ 200	≈ 200		≈ 280

Table 6: Outline of DCM/H_2 experiments.

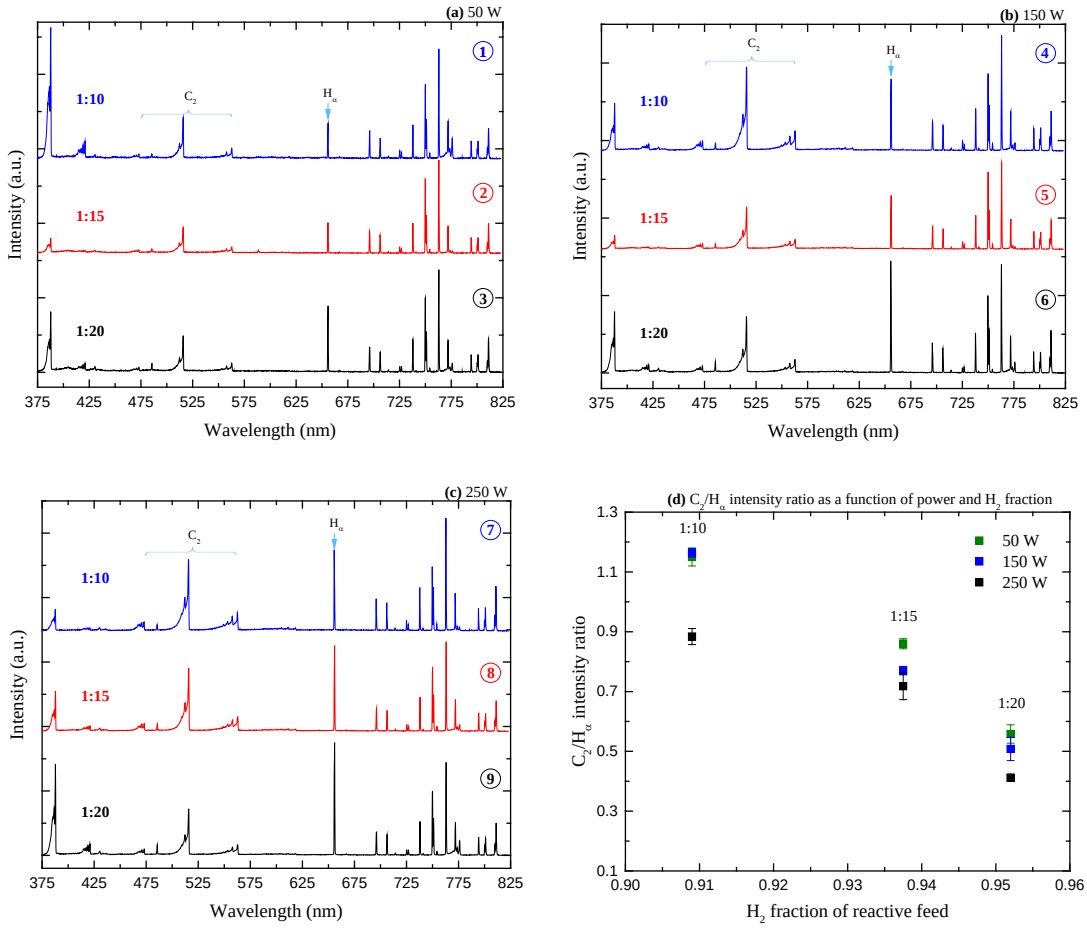

Figure 54: Spectra and C_2/H_α trends from OES of the DCM/H_2 mixtures (experiments' conditions see Table 7).

From the Raman spectra (Figures 55,56, and 57), the D and G peaks are in general broader in the DCM/H_2 mixture experiments than in the CH_4/H_2 mixture. Small 2D bands appeared only with 1:20 DCM to H_2 when using RF power greater than 50 W. The position and the FWHM of the second-order two-phonon process (2D) is a measure of the number and thickness of layers in the product. Also, the exciting energy of the laser had an impact on the position of the 2D band.

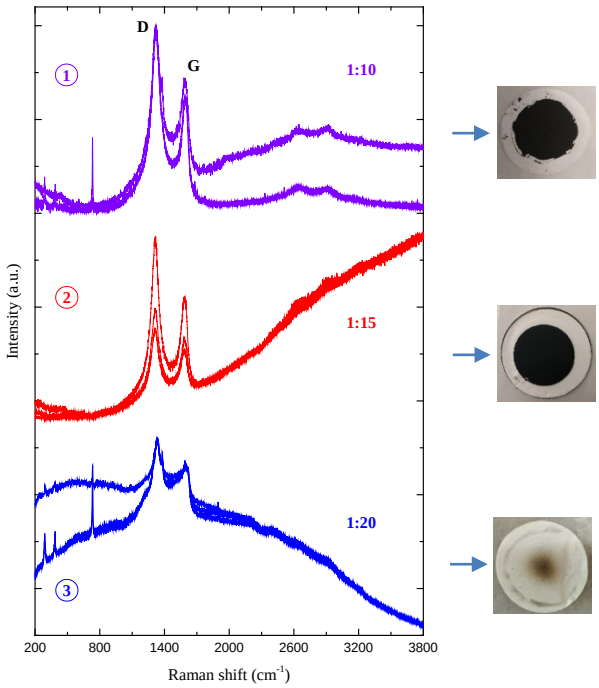

Figure 55: Raman spectra of the material on the filters [RF power: 50 W] (experiments' conditions see Table 7).

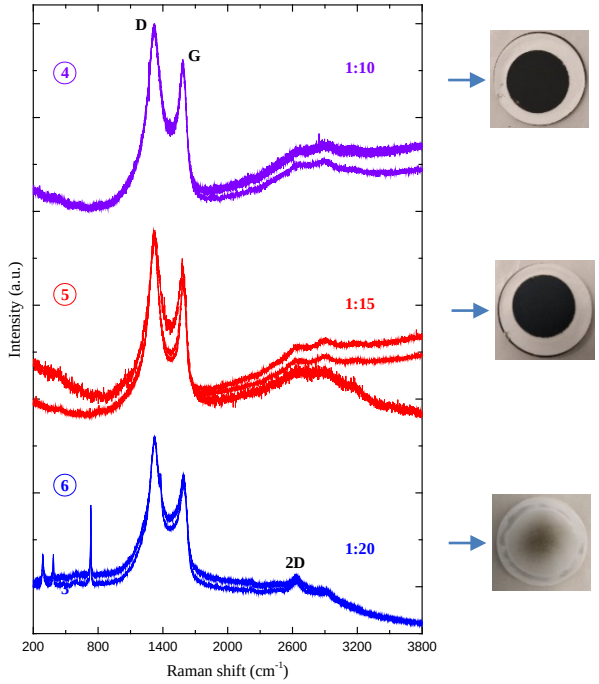

Figure 56: Raman spectra of the material on the filters [RF power: 150 W] (experiments' conditions see Table 7).

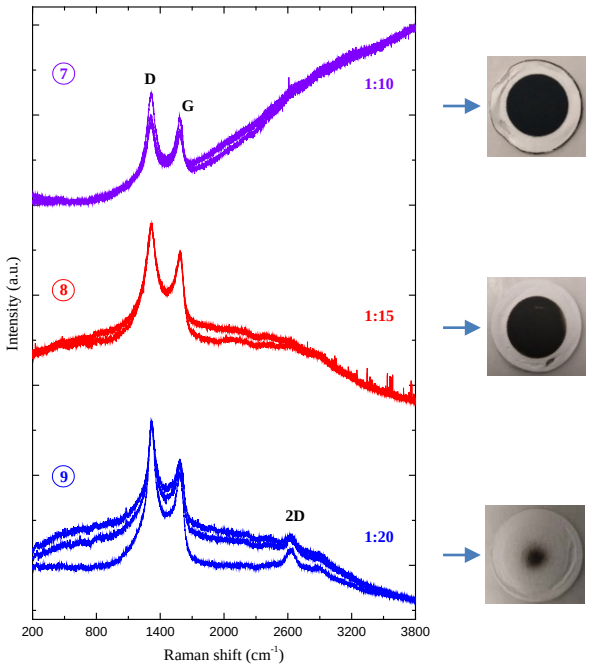

Figure 57: Raman spectra of the material on the filters [RF power: 250 W] (experiments' conditions see Table 7).

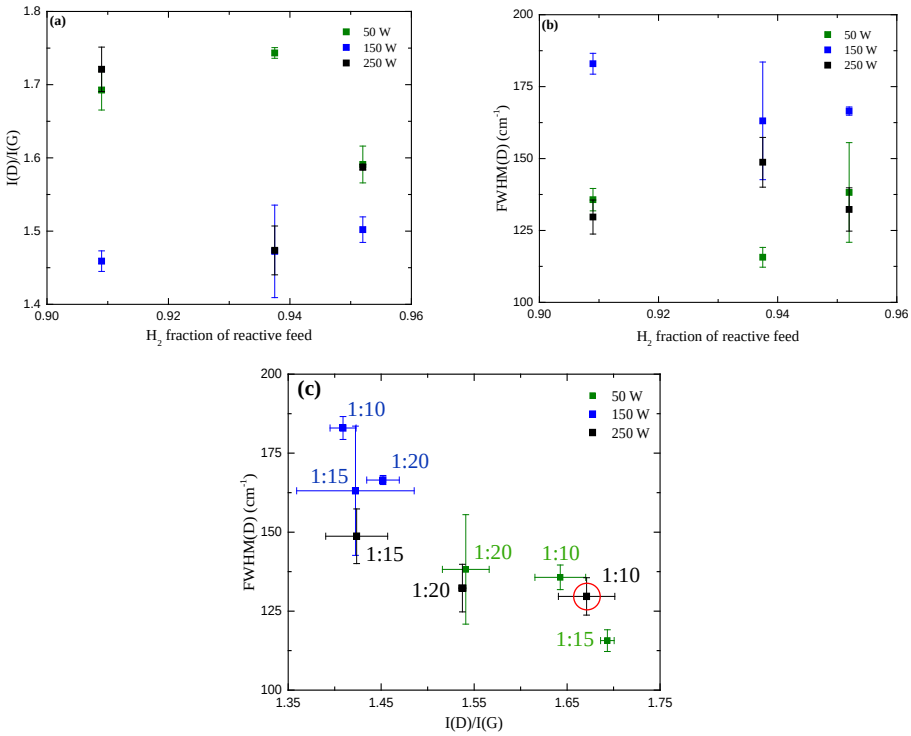

Figure 58: The trends in Raman spectra (experiments' conditions see Table 7).

There was a clear relationship between I(D)/I(G) and FWHM(D) in the Raman parameters from Figure 58 (c) when the operating power was 250. There was an obvious link between the Raman spectra and material morphology at this power. Signs consistent with 'nanocrystalline graphite', specifically at high I(D)/I(G) and low FWHM(D), coincided with an abundance of onion-like structures and particles with hollow or amorphous cores surrounded by graphitic rings as displayed in Figure 59.

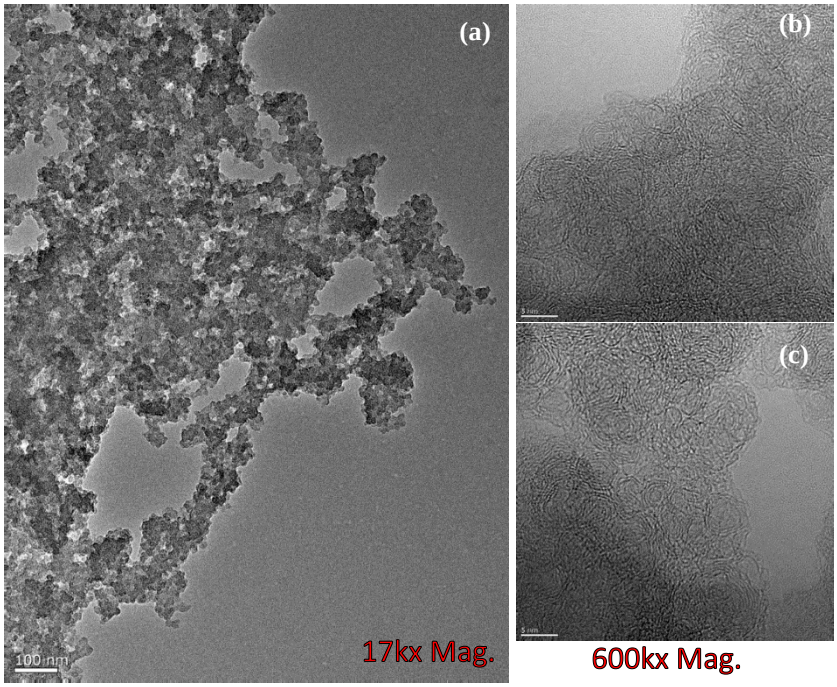

Figure 59: TEM photos of 1:10 [DCM:H_2] ratio at 250 W (experiment's conditions see Table 7). In (b) and (c), scale bars are 5 nm.

4.3.2.2.3. DCM/O_2 study

Since Frenklach, M. *et al*. [60] nucleated diamonds homogeneously under MW plasma discharge using DCM/O_2 reactants, used the same mixture in a RF plasma

discharge. The common conditions of these experiments were: reactor pressure, 50 Torr; total flow rate, 50 sccm; bath temperature, −10°C. The rest of the conditions were as described in Table 7.

Experiment		①	②	③	④	⑤	⑥
Flow rate (sccm)	DCM	0.1	0.5	1	2.5	0.1	0.5
	O_2	0.5	0.5	5	2.5	0.5	0.5
Ratio	DCM:O_2	1:5	1:1	1:5	1:1	1:5	1:1
Ar dilution (sccm)		49.40	49	44	45	49.40	49
Power (W)		50				150	
Plasma Volume (cm^3)		3.1	2.5	2	2	6.16	4.62
Production rate (mg/h)		NA	0.07	NA	NA	NA	NA
Residence time (ms) [approx.]		≈ 187	≈ 143	≈ 108	≈ 86	≈ 233	≈ 173

Table 7: Outline of DCM/O_2 experiments.

Contrary to the preceding experiments, increasing the applied RF power prevented particle nucleation as opposed to the other way around. Making solid materials with DCM/O_2 mixtures was more difficult than previously thought. Increasing the RF power, as illustrated in Figure 60, improved the population of atomic H dramatically while C_2 remained about the same. This was not the case with the DCM/H_2 mixtures (see Figure 54 [c]), and it might clarify the low nucleation rates. To recognize the impact of the O_2/DCM

ratio and Ar dilution level on the optical emission spectra (OES) of the plasma see Appendix B.

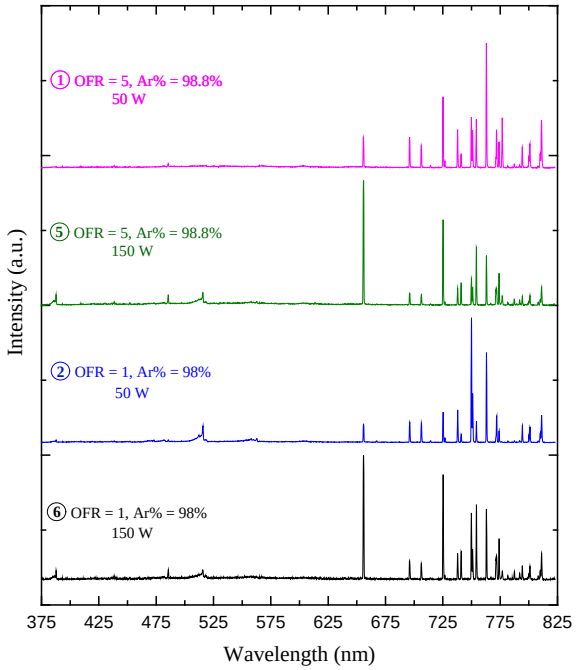

Figure 60: OES of the DCM/O_2 mixtures (experiments' conditions see Table 8).

Both oxygen-fuel ratio (OFR) and Ar percentage (Ar%) were calculated from

$$OFR = \frac{n_{O_2}}{n_{DCM}} \tag{20}$$

and

$$Ar\% = \frac{n_{Ar}}{n_{total}} \tag{21}$$

The Raman spectra here look comparable to those of the material collected from the DCM/H_2 mixtures. Together I(D)/I(G) intensity ratios and FWHM's predict mostly

amorphous carbon (see Figure 61). When the plasma had high concentrations of DCM and O_2 (i.e., higher OFR) and the applied power was increased, the temperature was significantly elevated. In this case, TEM and Raman spectra confirm mainly amorphous carbon with very little crystallinity and some circular grains as shown in Figure 62.

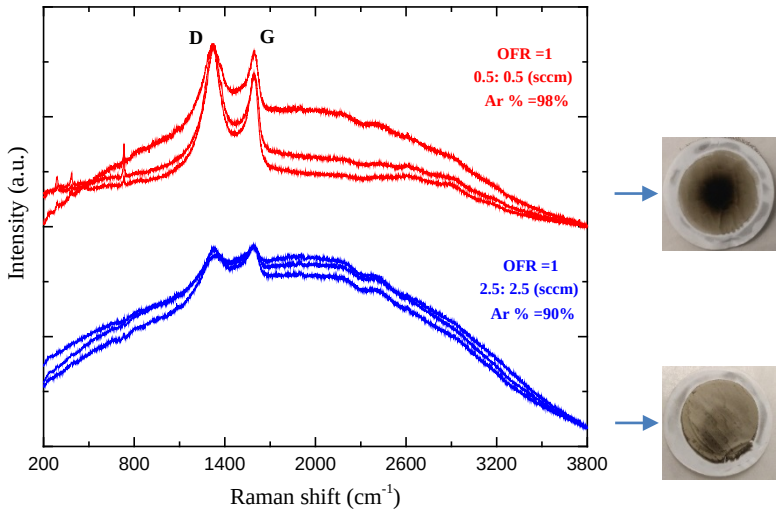

Figure 61: Raman spectra of the collected material under different reactants' concentrations (experiments' conditions see Table 8).

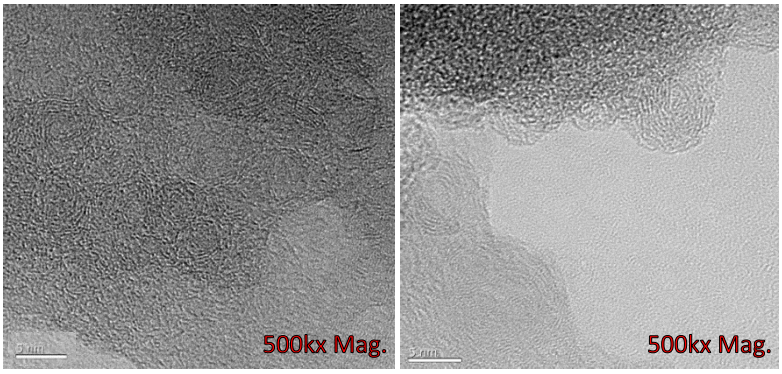

Figure 62: TEM photos of the sample that has OFR=1 and Ar% =90% (experiment's conditions see Table 8). The scale bars are 5 nm.

After running a few experiments using DCM with O_2, some issues were observed that were not noticed when using DCM with H_2. A yellow-green residue was developed on the downstream lines and the pump's oil turned black rapidly. These two problems indicated the formation of new compounds such as HCl and Cl_2. Attempts to reach higher concentrations of reactants in the plasma failed, and it was concluded that further system upgrading was required to handle the plasma byproducts.

4.3.2.2.4. $CH_4/H_2/SiH_4$ study

Since nanodiamonds were not found in CH_4/H_2 plasma growth, silicon in silane was proposed to provide seeds for nanodiamond growth from the gas-phase. In prior work hollow silicon carbide nanoparticles were synthesized with silane but only after two cascaded stages of non-thermal RF plasma chambers. The silane and Ar were first mixed to form silicone nanoparticles. Then the Si nanoparticles and the Ar were mixed with CH_4 to synthesis silicon carbide (β-SiC) nanocrystals [90]. Therefore, adding H_2 to the CH_4/SiH_4 mixture may instead fabricate nanodiamonds doped with silicon, instead of silicon carbide. Table 8 presents some of the experiments that were performed.

Exp.	Flow rate (sccm)			Ar dilution (sccm)	Production rate (mg/h)	The filter
	CH_4	H_2	SiH_2			
①	0.25	0.75	0	49	0.03	
②	0	0	0.02	49.98	0.16	
③	0.25	0.75	0.02	48.98	0.75	
④	0.25	1.75	0	48	NA	
⑤	0	1.75	0.02	48.23	NA	
⑥	0.25	1.75	0.02	47.98	1.04	
⑦	0.25	0.25	0.10	49.40	5.80	
⑧	0.25	1.0	0.10	48.65	0.98	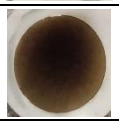
⑨	0.25	4.0	0.10	45.65	1.35	
⑩	0.25	0.25	0.25	49.25	10.46	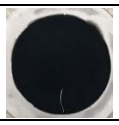
⑪	0.25	1.0	0.25	48.50	12.50	
⑫	0.25	4.0	0.25	45.50	15.70	

Table 8: Outline of the $CH_4/H_2/SiH_4$ experiments.

From Figures 63 and 64, the Raman spectra of the fabricated carbon particles with and without SiH_4 added (Experiment 3) looks very similar. Adding more H_2 has removed most of the black carbon leaving behind a yellow-orange material which is most likely silicon nanoparticles. Besides D and G bands, not much is easily identifiable in the Raman spectra. Combining CH_4 with SiH_4 greatly accelerated the growth beyond what either ingredient would produce on its own. A higher H_2 content suppressed the carbon and Si growths individually, but not when they were combined.

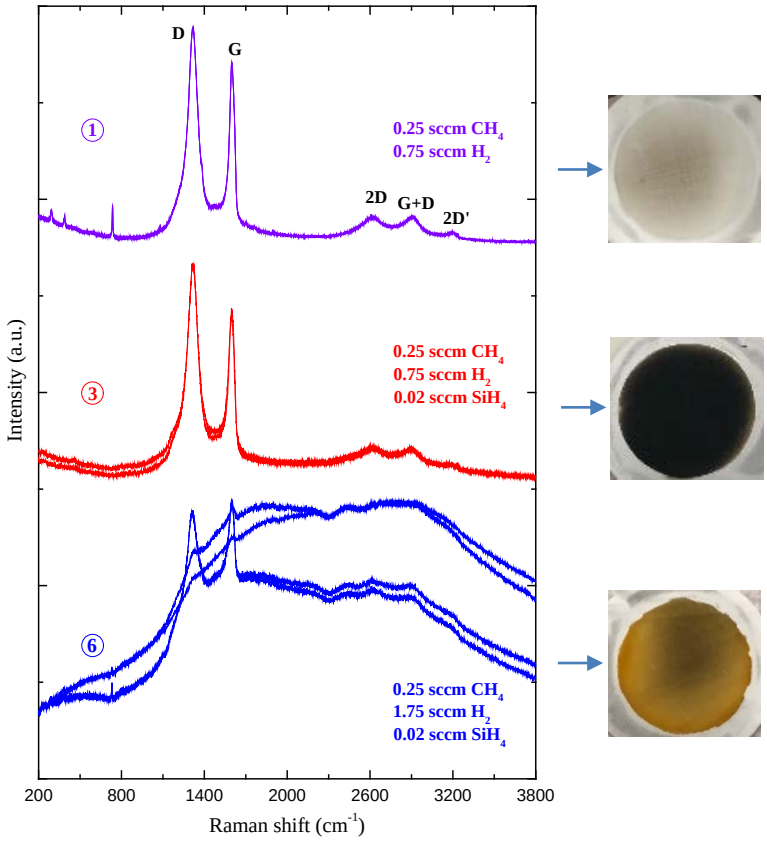

Figure 63: Raman spectra of the collected material under different reactants' concentrations (experiments' conditions see Table 9).

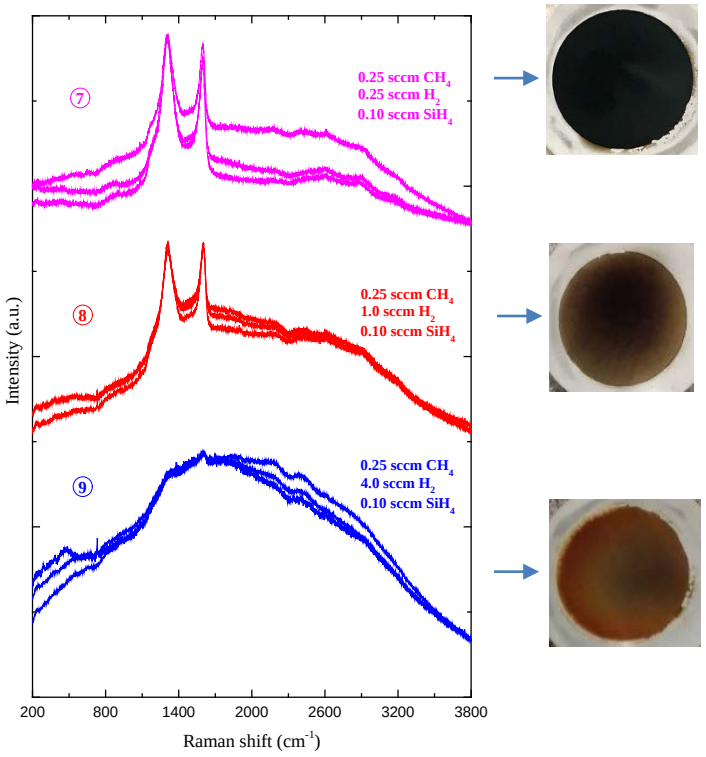

Figure 64: Raman spectra of the collected material under different reactants' concentrations (experiments' conditions see Table 9).

The collected particles looked similar to those produced by previous CH_4/H_2 mixtures, yet in the TEM there were somewhat onion-like particles with turbostratic graphite lattice fringes, but no other evidence of crystallinity (see Figure 65). In the Raman spectra both amorphous and crystalline phases of Si appear to be present, as illustrated in Figure 66, where the unlabeled peaks were all PTFE. From the TEM photos in Figure 67, the particles are mostly amorphous, though some lattice spacings are present that match well with Si (111) and (220) faces (~3.1 and 1.9 Å, respectively). SiH_4 and CH_4 have a synergistic effect on each other that promotes the growth. More results about the $CH_4/H_2/SiH_4$ study have posted in Appendix C.

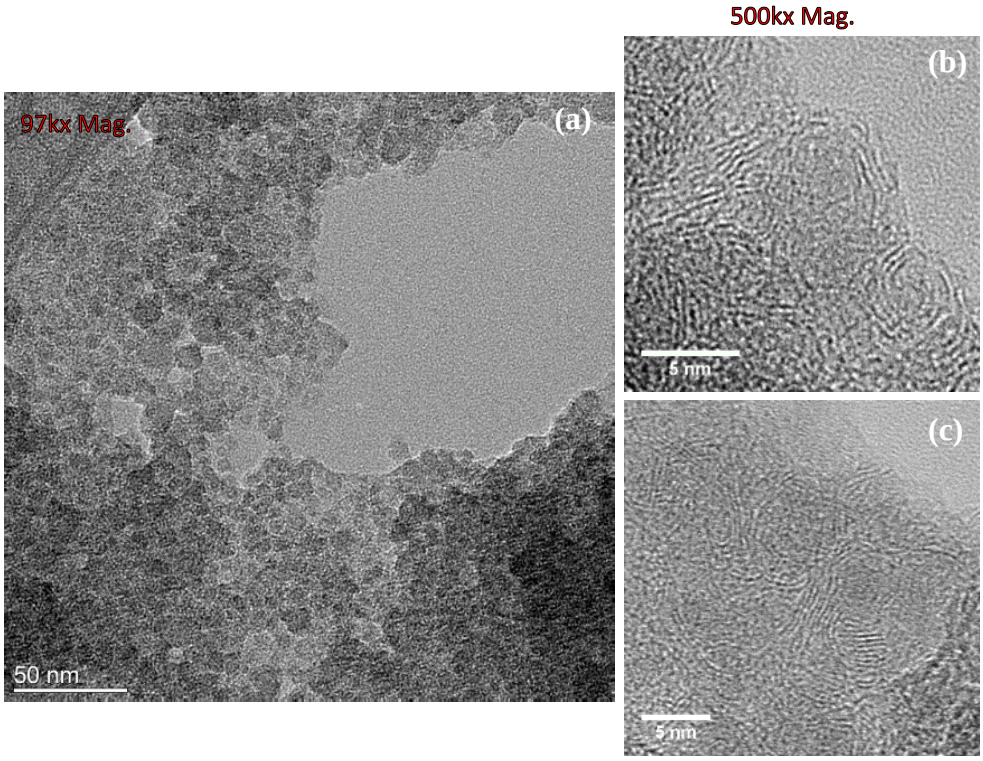

Figure 65: TEM photos of material collected from Experiment (3) (experiment conditions see Table 9). In (b) and (c), scale bars are 5 nm.

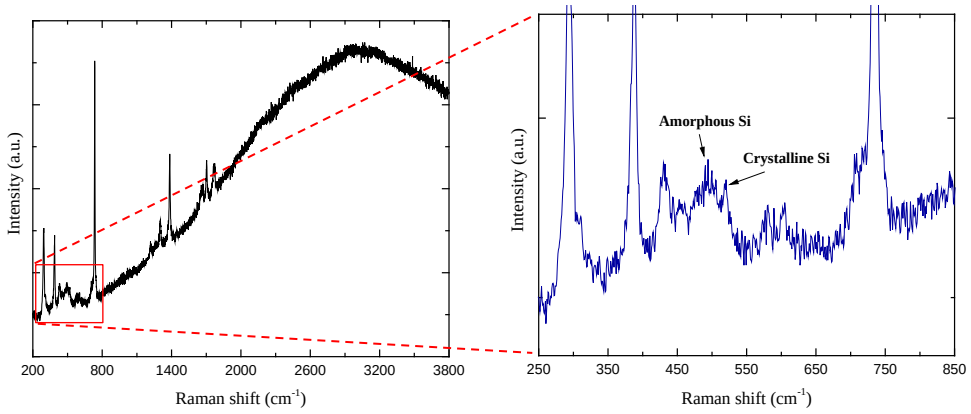

Figure 66: Raman spectrum of material collected from Experiment (2) (experiments' conditions see Table 9).

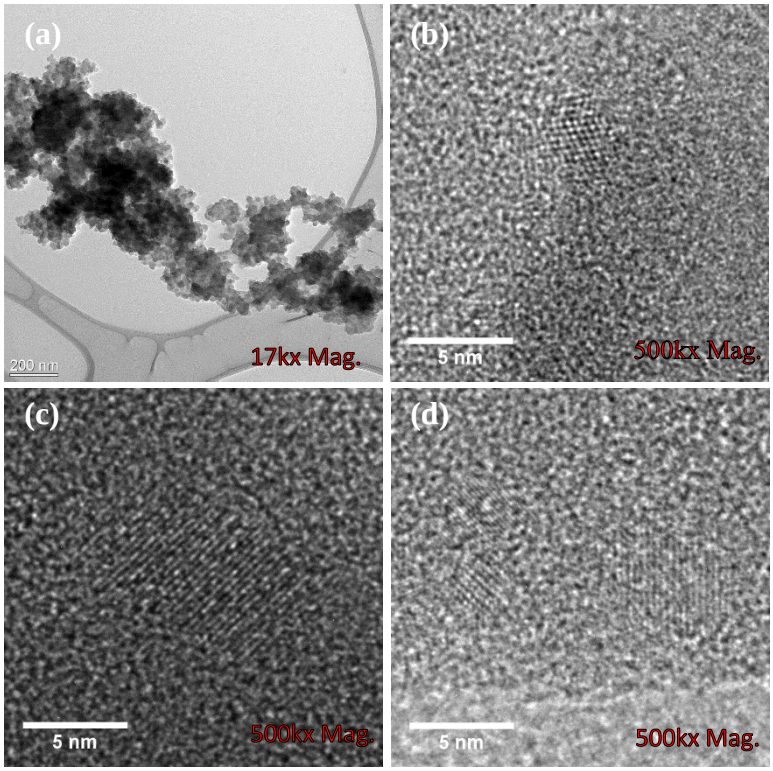

Figure 67: TEM photos of material collected from Experiment (2) (experiment conditions see Table 9).

Lowering the H_2 flow rate to 0.25 sccm and increasing the SiH_4 concentration to 0.1 sccm made a big difference in the particles' morphology. They appear to be polycrystalline where the most common lattice spacing was ~2.5-2.6 Å, which is shared by all SiC polytypes. By keeping the SiH_4 flow rate at 0.1 sccm and raising the H_2 flow rate to 0.25 sccm, the crystallinity was significantly improved, and the most common lattice spacing was 2.5 Å, as demonstrated in Figures 68 and 69. Consequently, tuning the concentration of H_2 can control the particles' sizes and suppress the amorphous carbon.

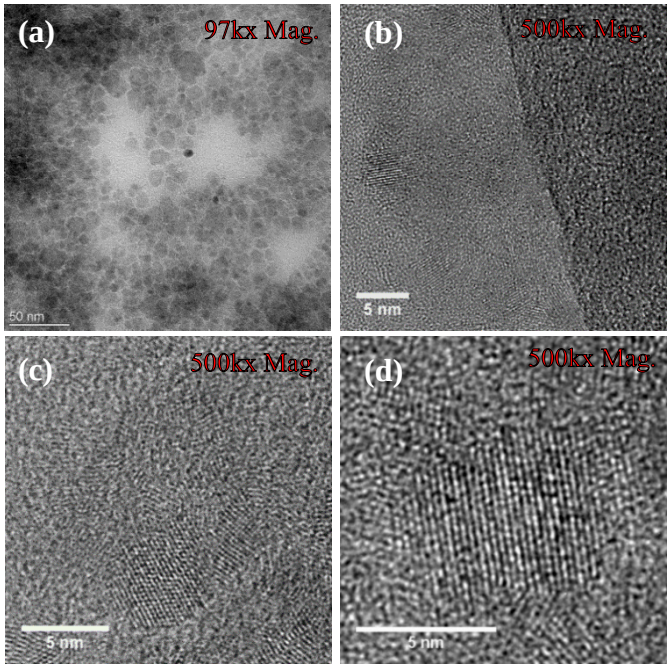

Figure 68: TEM photos of material collected from Experiment (7) (experiment conditions see Table 9).

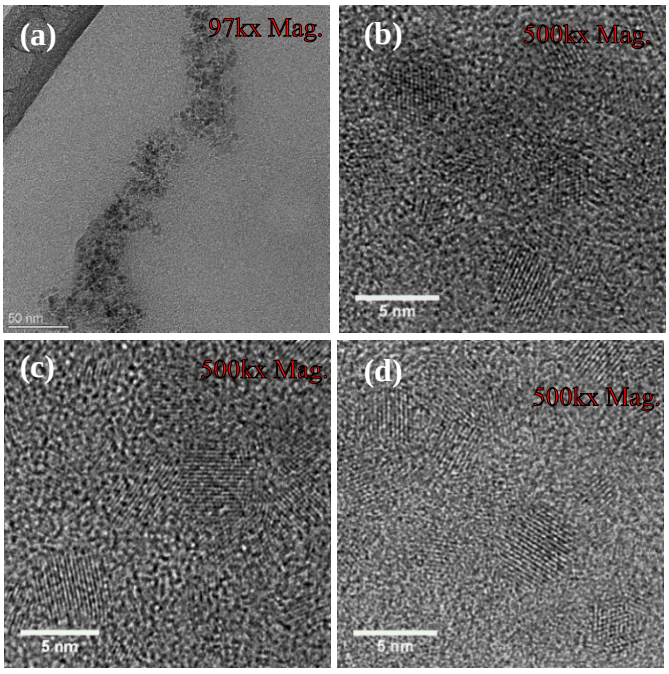

Figure 69:TEM photos of material collected from Experiment (9) (experiment conditions see Table 9).

4.3.3. Microwave plasma discharge experiments:

MW plasma discharges are broadly employed in synthesizing nanodiamonds. Because of this we selected it for use in our new reactor. The design was a vertical quartz tube with a large inner diameter (46 mm) with two inlets for diamond precursors. Two positions, top and bottom, were provided to collect the products. A simplified sketch of our MW reactor is presented in Figure 70. The detail about the MW plasma discharge was addressed in Section 3.2.7. The performed MW plasma experiments were divided into three major groups, as presented in

Table **9**. Each group includes a number of experiments. Only the successful experiments will be discussed subsequently. Roughly, the reactor pressure in all experiments was kept to be < 800 mTorr. Furthermore, the bubbler (or bed) temperatures in all the experiments were fixed at 23°C (room temperature).

A mixture of argon (Ar 95%) and hydrogen (H_2 5%) as a carrier was used in all the experiments. The MW power supply was a commercial kitchen microwave oven which was operated at a frequency of 2.450 GHz with 700 W power. Due to the MW's source inability to work for a long time, all of the experiments were run for a short period (> 30 min). The mass flow rates of the reactants were deliberately chosen to be very high to overcome this limitation.

In addition, chemical treatment was done on the collected materials. Since the material produced by the RF plasma discharge experiments' were not chemically treated, we believe that this skewed our results and if fact nanodiamonds might have been

produced, but just were not detected. The chemical treatment was described in detail in section 3.2.3. A schematic of the chemical treatment process is sketched in Figure 71.

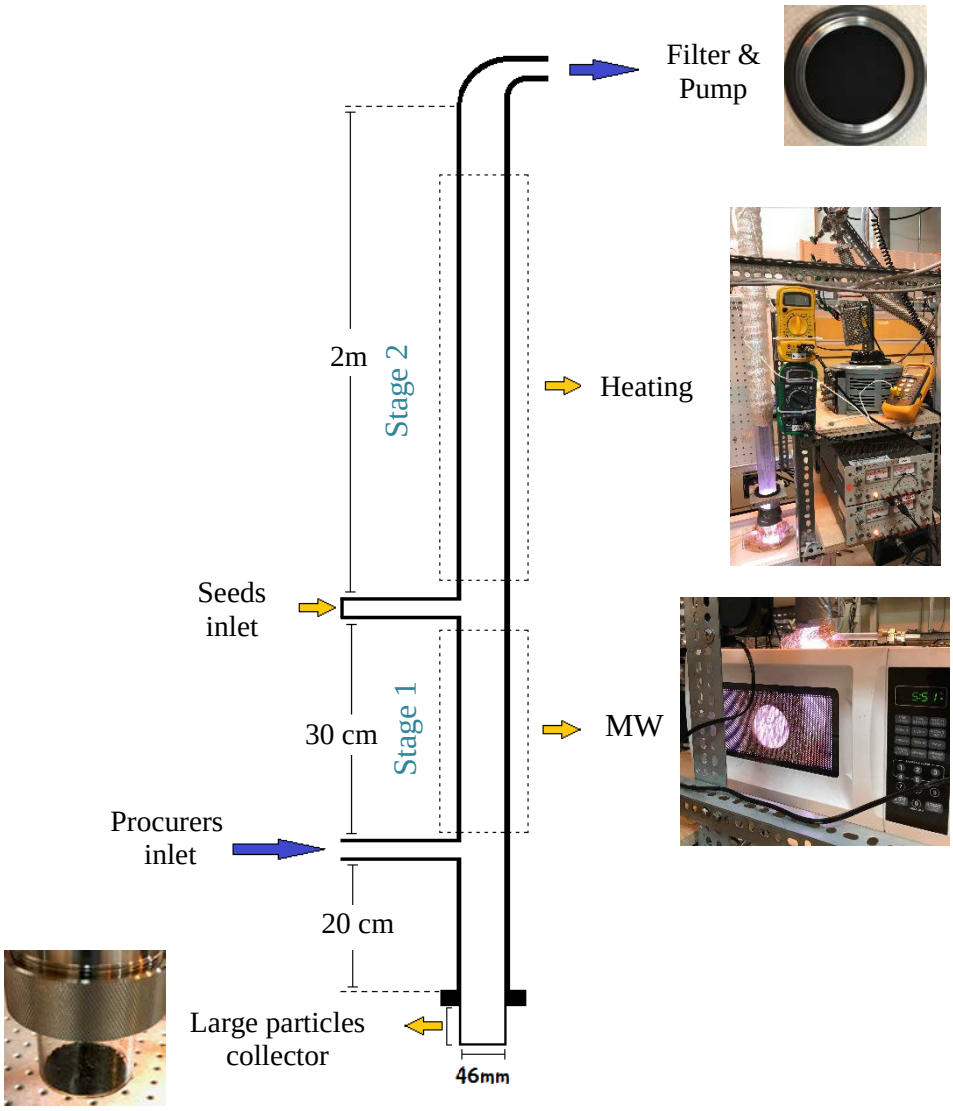

Figure 70: Scheme illustration of our MW system configuration.

Experiments' groups	①	②	③
	DCM	DCM + N_2	DCM + $C_6H_{15}N$
Carrier flow rate (sccm)	2	2	2
Mass flow rate	184.22 mg/h	48.23 g/h	>110 g/h
N_2 flow rate (ssm)	0	2	0
Bubbler temperature (°C)	23	23	23
Bubbler pressure	~ 25 psi	400 Torr	320 Torr
Reactor pressure (mTorr)	750	530	780
Stage 2 temperature (°C)	700	700	660
Dilution (sccm)	40		
MW power (W)	700		
Plasma Volume (cm^3)	~ 720		
Residence time [approx.]	Order of second		

Table 9: An outline of MW plasma discharge experiments.

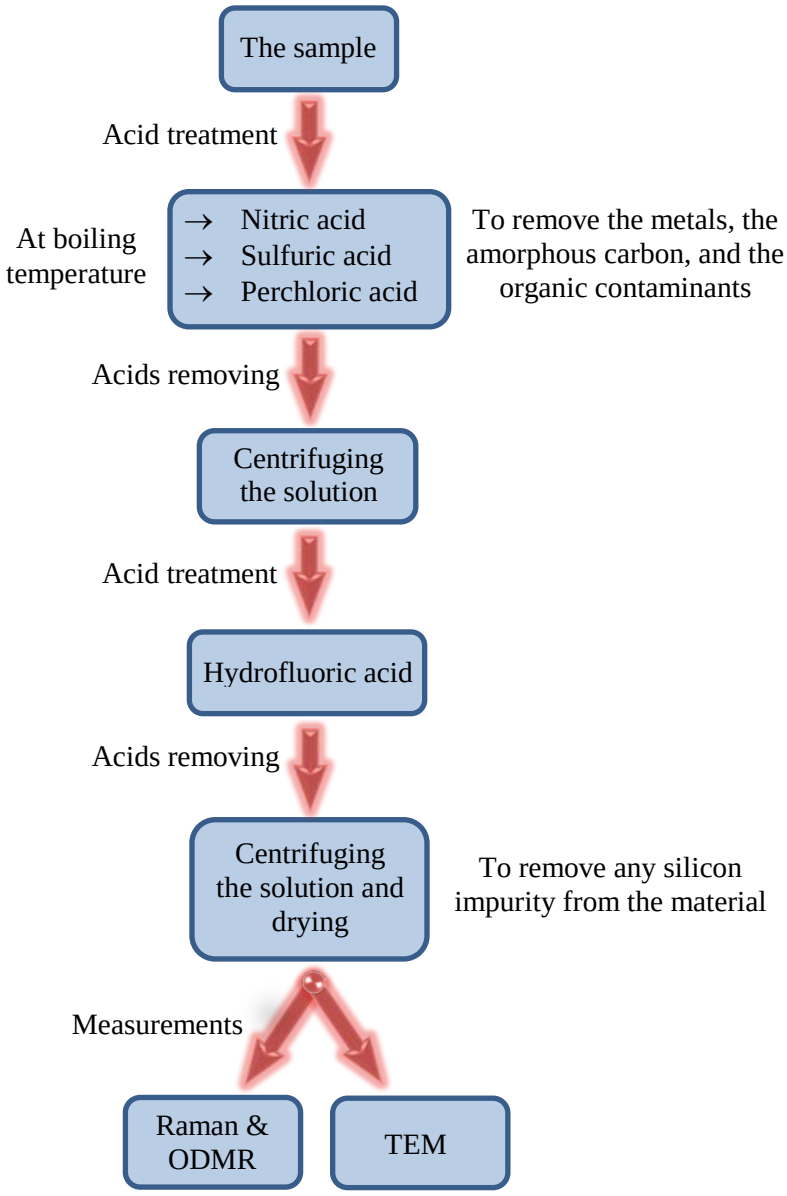

Figure 71: A summary of the chemical treatment procedure.

4.3.3.1. Group 1: DCM + Ar/H_2 gas mixture.

The first successful runs lasted about ten minutes and the conditions were as briefed in Table 10. After the acid treatment, the material was taken to a homemade confocal setup to measure Raman spectra, fluorescence, and optically detected magnetic

resonance (ODMR). Very small particles (below the diffraction limit) were detected. A 1.4 NA oil objective was utilized to get the XY scan image (see Figure 72), and the excitation laser wavelength was 532 nm. A high-intensity peak at 630 nm (1.967 eV), as demonstrated in Figure 73, was found during the Raman spectra measurements. We have seen this peak in diamond samples from other groups and commercial diamonds. In the literature no adequate explanation was published about the origin of this peak. Bray, K. *et al.* [91] have observed this peak in nanodiamonds that have been grown applying MW plasma CVD. This peak was also detected by Sandstrom, R. G. *et al.* [92] when they were studying the polycrystalline diamond films grown on a silicon substrate by MW plasma CVD. This center was noticed to be particularly pronounced in nitrogen-doped diamond films [93].

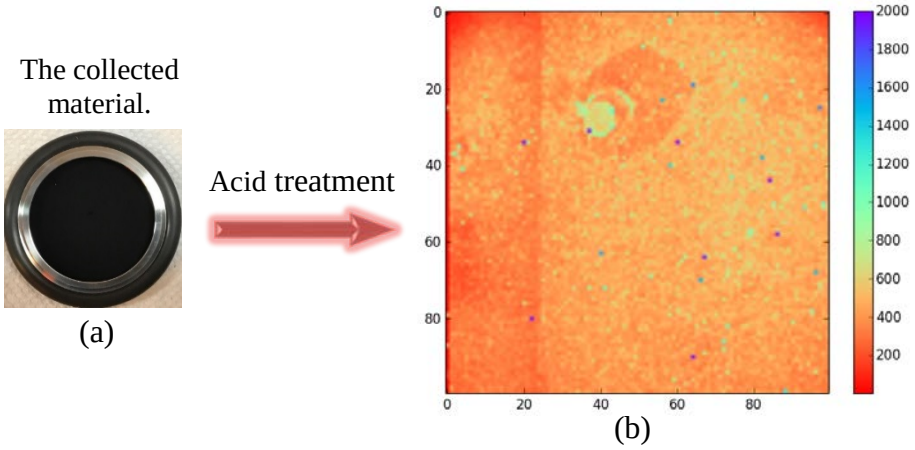

Figure 72: The filter before acid treatment (a), and an XY scan image of the sample after acid treatment (b).

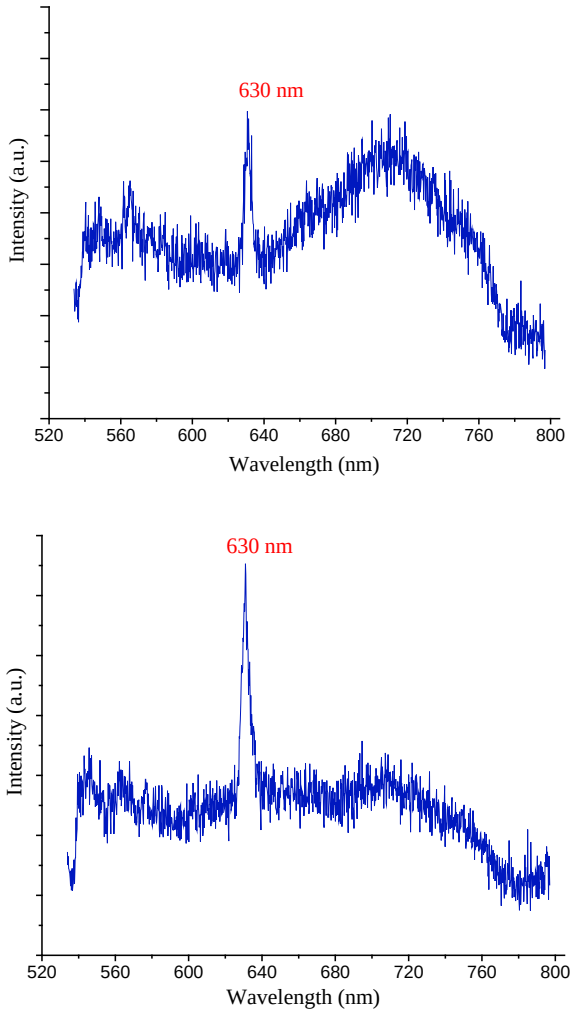

Figure 73: Raman spectra of two spots of the sample.

The TEM image of nanodiamonds, in Figure 74, was taken at a low magnification and the particles were not clearly visible until after heating up the TEM grid inside the microscope to 750°C for ~ 5 min to remove organic impurities. This was done for both samples studied. This sample wasn't yet irradiated when these TEM images were taken. Figures 75 (b) and 76 (b) show the diffraction patterns of two single particles. Software (ImageJ) was employed to measure *d* spacings from the diffraction pattern images. The

measured lattice spacings of the particles correspond to cubic diamond (111) or lonsdaleite (002) where the measured *d* spacings were between 2.05- 2.06 Å.

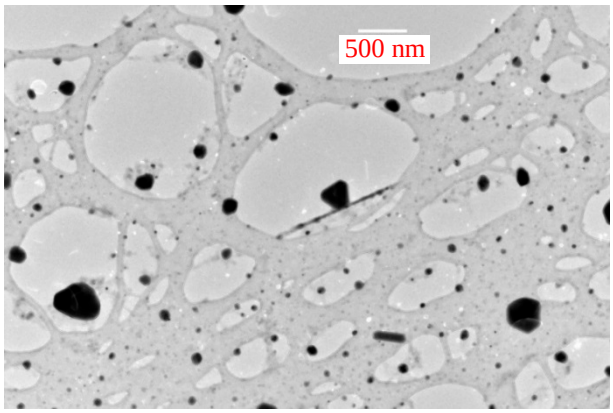

Figure 74: A TEM image.

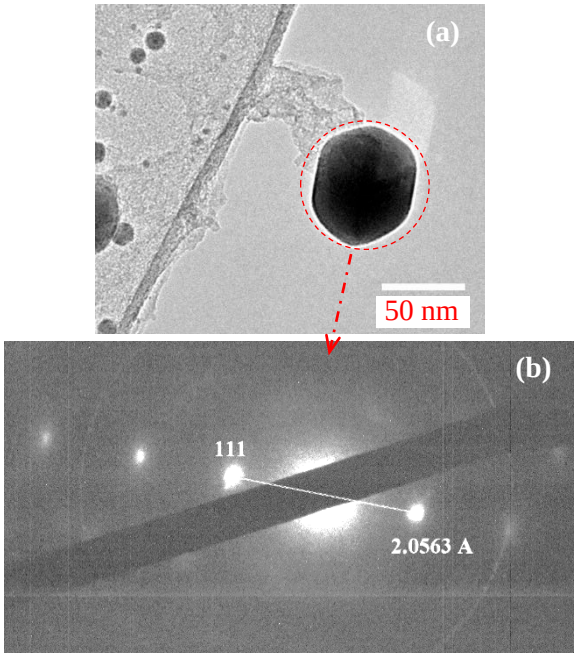

Figure 75: A TEM image (a) and diffraction pattern (b) for one of the NDs.

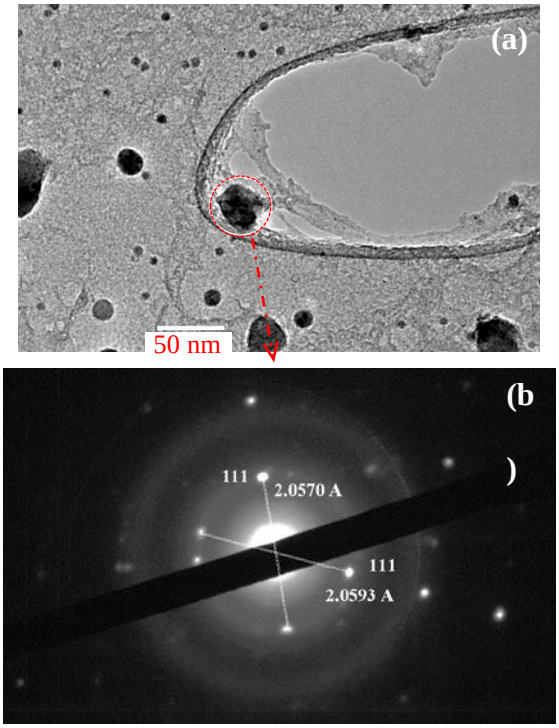

Figure 76: A TEM image (a) and diffraction pattern (b) for different ND.

4.3.3.2. Group 2: DCM + N_2 + Ar/H_2 gas mixture.

The reactor pressure was 530 mTorr when the experiment started. There wasn't a significant change or increase in the pressure by the end of the experiments even with a high DCM mass flow rate (48.23 g/h). The run time under these was ≤ 10 min due to the MW plasma source on-time limit. The particles produced in this experiment were picked up from the bottom of the system (i.e., the large particles collector reservoir) (see Figure 77). T The previous cleaning and analysis procedures were duplicated with this sample. The measured *d* spacings for this sample were between 2.031- 2.063 Å, as exhibited in Figures 78 (b) and 79 (b). These TEM images were taken before irradiation of the sample.

Figure 77: The collected material before acid treatment from the large particles collector reservoir.

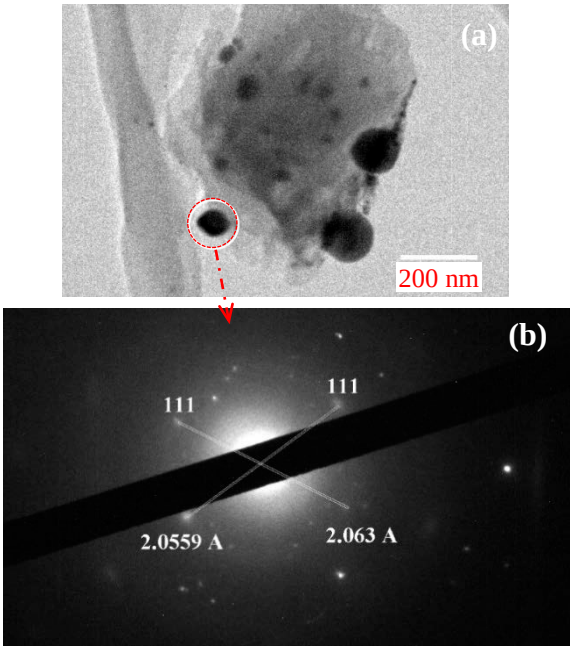

Figure 78: A TEM image (a) and diffraction pattern (b) for single ND.

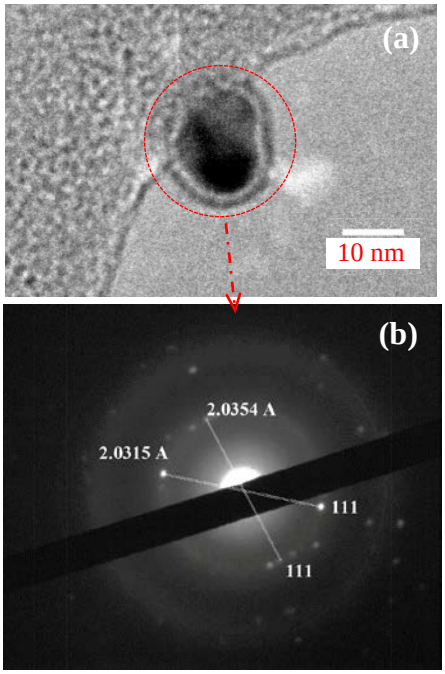

Figure 79: A TEM image (a) and diffraction pattern (b) for different ND.

4.3.3.3. Group 3: DCM + $C_6H_{15}N$ + Ar/H_2 gas mixture.

The reactor pressure in this experiment was 780 mTorr at the start and did not change much during the run. The mass flow rate of the DCM and $C_6H_{15}N$ mixture was very high (> 110 g/h). The characterized particles were taken from the material collected on the filter after chemical treatment as described earlier. The measured *d* spacings for this sample were between 2.050- 2.058 Å, as shown in Figure 81 (b). For this sample irradiation was carried out using TEM at temperature of 740 °C with electron dose ~ 8×10^{18} e/cm^2. Figure 82 (a) presents an XY optical fluorescence scan of the irradiated TEM grid which showed ND diffraction patterns. Two irradiated areas of nanodiamonds contained nitrogen-vacancy (NV^-) centers, NV^-1 and NV^-2. The Raman/fluorescence

spectrum of $NV^{-}1$ is shown in Figure 82 (b). An ODMR spectrum for $NV^{-}2$ is shown in Figure 82 (c). The peak of the ODMR spectrum was ~ 2.845 GHz, which represents a small shift in the peak from its common value in the literature which is 2.87 GHz. The origin of the shift presumably was some impurities or lattice irregularities in the NDs.

Figure 80: The material collected on the filter before acid treatment.

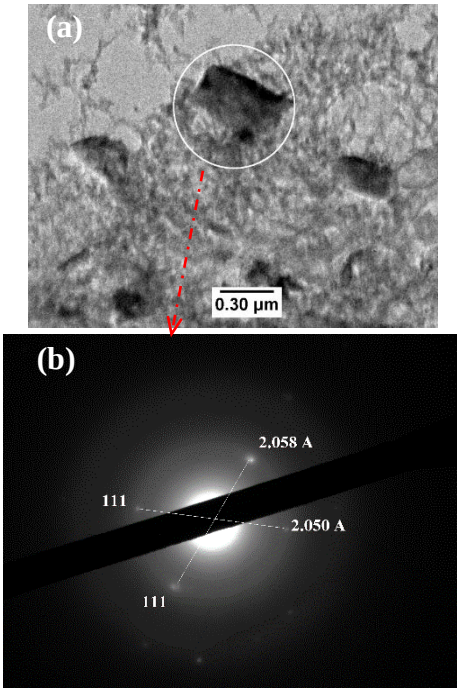

Figure 81: A TEM image (a) and diffraction pattern (b) for a single particle.

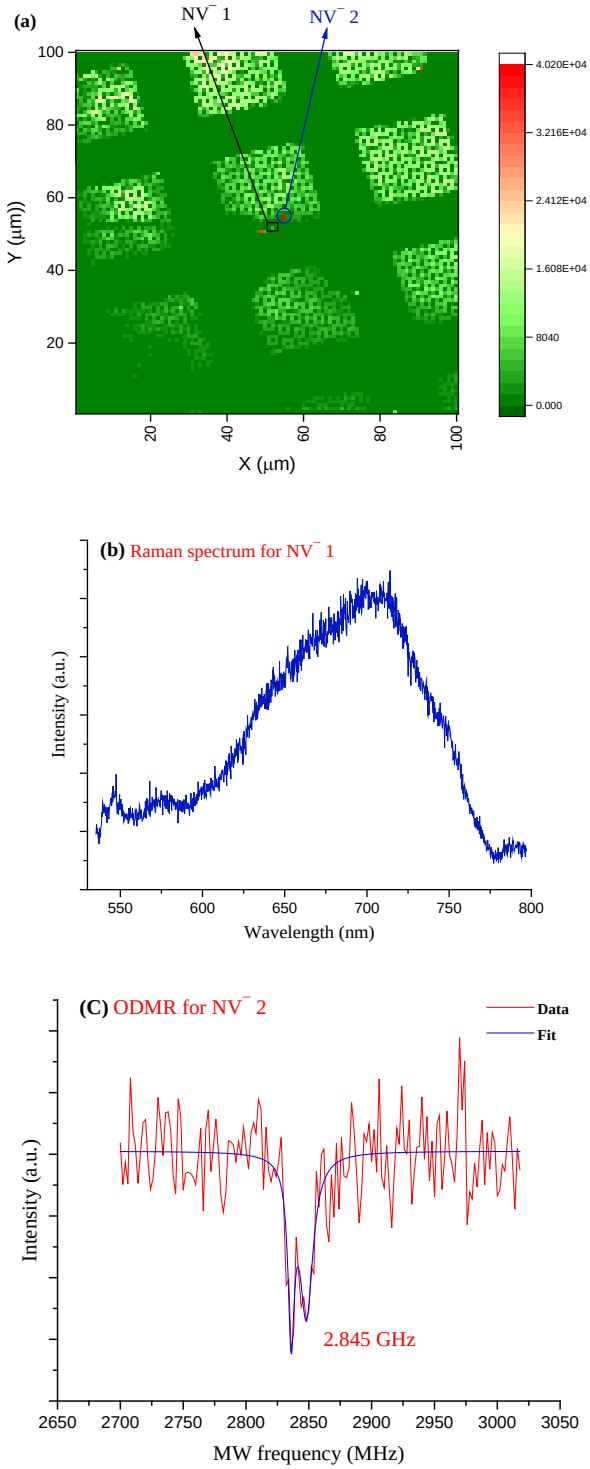

Figure 82: An XY scan image (a), Raman spectrum (b), and ODMR (c) for the sample after acid treatment and irradiation with TEM.

4.3.4. Experiments summary:

A. At Case Western Reserve University – Cleveland, OH

Each experiment was done with different powers, ratios, and volumetric flow rates.

A.1. *Straight-tube configuration reactor with adamantane*

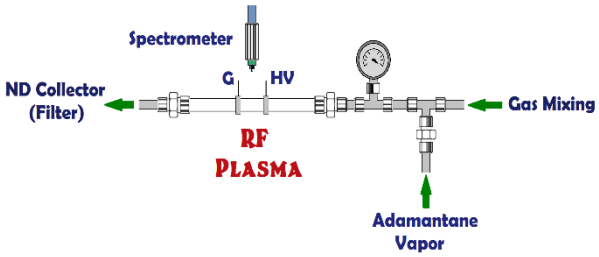

Exps. Qty	Exp. Mixtures (+ Ar plasma)	Goal	Result
3	Adamantane with No plasma	Does the adamantane reach the filter?	Adamantane collected
6	Adamantane	Does the adamantane survive?	Didn't survive, flakes
3	Adamantane + H_2	Does the hydrogen protect adamantane?	No, yellow liquid
6	Adamantane + CO_2 + CH_4	Growth NDs	Oily liquid, no particles

Table 10: The quantities of straight-tube reactor experiments with adamantane

A.2. *T-tube configuration reactor with adamantane*

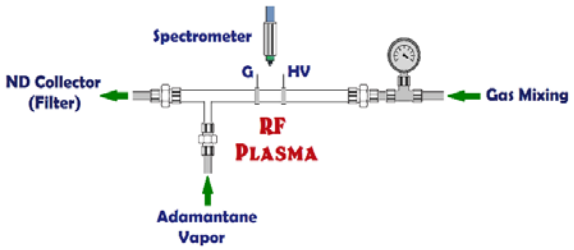

Exps. Qty	Exp. Mixtures (+ Ar plasma)	Goal	Result
3	Adamantane with No plasma	Does the adamantane reach the filter?	Adamantane collected
4	Adamantane	Does the adamantane survive?	Survived
8	Adamantane + CH_4	Growth NDs	Brown material
10	Adamantane + CO_2 + CH_4	Growth NDs	Less material

Table 11: The quantities of T-tube reactor experiments with adamantane.

A.3. *Straight-tube configuration reactor without adamantane*

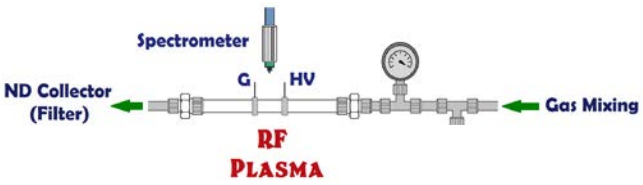

Exps. Qty	Exp. Mixtures (+ Ar plasma)	Goal	Result
25	$CH_4 + CO_2$	Find a cut-off point at which this species combination will nucleate material	No material
47	$CH_4 + H_2$	Study behavior of CH_4/H_2 mixtures and characterize materials before and after oxidation.	Power and CH_4/H_2 ratio contribute to material morphology (more lattice spacings with high power). D & G peaks still before and after.
12	$CH_2Cl_2 + H_2$	Searching for links between plasma parameters and structure of material	There was no clear trend
12	$CH_2Cl_2 + O_2$	Seeded growth	No NDs
3	SiH_4 (Silane)	Growth Si NP	Si NP (< 10 nm)
2	$SiH_4 + H_2$	Study the effect of H_2 on growth	No material
16	$SiH_4 + CH_4 + H_2$	Diamond crystals would likely have Si-V centers	SiC (~ 5 nm)

Table 12: The quantities of straight-tube reactor experiments without adamantane.

B. At Texas A&M University – College Station, TX

Exps. Precursors + Ar/H_2 gas mixture [95%/5%]	Goal	Result	NDs sizes
CH_2Cl_2 + $[Ar/H_2]$ (**5** times)	Growth NDs with new conditions	Succeeded	50nm to < 10nm
CH_2Cl_2 + $[Ar/H_2]$ + N_2 (**2** times)	Growth NDs with NV	Succeeded	100nm to 10nm
[CH_2Cl_2 + $C_6H_{15}N$ (Triethylamine)] + $[Ar/H_2]$ (**4** times)	Growth NDs with NV	Succeeded	< 300nm with NV color center

Table 13: The quantities experiments at TAMU with no adamantane.

5. FUTURE WORK

Growing nanodiamonds from the gas-phase using a bottom-up approach, growing around a diamond-like organic seed molecule (diamondoid molecule) in a plasma discharge is a new technique. The principle procedure of manufacturing NDs by this technique involves cracking light molecular weight hydrocarbons such as methane to form methyl radicals and subsequently bonding them to the seed molecules to synthesize NDs homogenously. This approach of growing diamonds will have numerous applications to bio-sensing, quantum information, and materials science because of the high quality of the fabricated NDs. Constructing an experimental setup to grow diamonds from organic molecules in different types of plasma discharge, with the ability to mix multiple growth molecules and the seed molecules in any proportion, is a prerequisite for successful seeded growth. Also, the setup needs to include diagnostics like optical spectroscopy to monitor the concentration of carbon radicals as well as to verify that the seed molecules remain intact. In the future it will be necessary to work at much lower pressures to avoid self-nucleation conditions.

Aside from nanodiamonds, micro- or nanoelectromechanical systems (MEMS/NEMS) have been attractive to scientists for more than a decade. Silicon-based MEMS devices were tested for biocompatibility and proved to be biocompatible. SiC is inert chemically and has been used as a semiconductor material in electronics. The β–SiC, for instance, has a very low thermal expansion coefficient and high thermal conductivity which might improve the MEMS/NEMS devices' sensitivities when utilized in living

cells. Since I already nucleated SiC from my RF reactor configuration, I firmly believe that with some care, upgrades, and good planning the quality and the size of the SiC nanoparticle will be improved significantly and may become useful for these MEMS devices.

After completing my Ph.D. degree, I intend to employ the obtained results and the experience from my work in the labs to contribute to these subjects and move forward with doing more experiments that I predict will benefit the scientific community.

6. CONCLUSION

NDs are highly inert chemically and biocompatible nanomaterials so they will facilitate optical tracking and imaging *in vivo* and *in vitro* environments. Based on the chemical inertness and the exceptional optical properties of fluorescent nanodiamonds (FNDs), much research has exploited the NDs to serve as biocompatible drug carriers and fluorescent imagers, including super resolution. Therefore, the utilization of FNDs in live systems has opened a wide and extremely important field for researchers. For instance, diamonds were used to achieve the requisite stability to integrate DNA with microelectronics, so as to develop bioelectronic sensing systems. In general, nanocrystalline diamonds thin film can be used as a stable substrate for eclectic biological modification.

Inside living human HeLa cells, optically detected magnetic resonance (ODMR), Rabi cycling, and spin-echoes of single FND were measured. In addition, FNDs were also employed in magnetic and temperature sensing. Temperature accuracy around 1 mK was achieved in bulk diamond. With continuous excitation, NDs' photoluminescence lasts for a very long time with no drastic decrease over time. In other words, photobleaching and blinking won't occur as happens in the samples containing dye, fluorophore molecules, and quantum dots. Furthermore, diamonds possessed many properties that were applied in the study of friction, wear, adhesion, and lubrication of two interacting moving surfaces.

My experiments were about the engineered growth of fluorescence nanodiamonds by different types of plasma discharges, DC, RF, and MW plasma discharges. My ultimate

goals in the Ph.D. experiments were to get a useful understanding of the nucleation process and achieve a high level of control over growth parameters such as the plasma power and radical concentrations.

It is paramount here to point out that throughout the experience I lived at TAMU and Case Western Reserve University while performing my experiments I have faced several obstacles with the devices I used. Since the DC, RF, and MW power supplies are the primary devices in generating plasma discharges, the issues I encountered were mostly related to them. For example, in the RF plasma experiments, it is likely that the resulting materials had NDs, yet the insufficient material purification was done to observe them. Funding limitations were the major obstacle here. Nonetheless, the results obtained from the MW plasma system at TAMU (i.e., the successful nucleation of NDs from the gas-phase) have proven that the problems can be overcome with work hard and effectively exploiting available resources.

I hope that the obtained results will positively contribute to scientific progress and open a new door for researchers.

REFERENCES

1. Ōsawa, E. and D. Ho, "Nanodiamond and its application to drug delivery". *J. Med. Allied Sci.*, 2012. **2**(2): p. 31-40.
2. El-Say, K.M., "Nanodiamond as a drug delivery system: Applications and prospective". *J. Appl. Pharm. Sci.*, 2011. **1**(6): p. 29-39.
3. Szunerits, S., *et al.*, "Antibacterial Applications of Nanodiamonds". *Int. J. Environ. Res. Public Health*, 2016. **13**(4): p. 413.
4. Mochalin, V.N. and Y. Gogotsi, "Nanodiamond–polymer composites". *Diamond Relat. Mater.*, 2015. **58**: p. 161-171.
5. Aleksenskiy, A., *et al.*, "The Fundamental Properties and Characteristics of Nanodiamonds, in Nanodiamonds: Applications in Biology and Nanoscale Medicine". 2010, *Springer*. p. 55-77.
6. Krueger, A., "The structure and reactivity of nanoscale diamond". *J. Mater. Chem.*, 2008. **18**(13): p. 1485-1492.
7. Vul', A.Y. and O.A. Shenderova, "Titl". 2013: *CRC Press*.
8. Yang, L., *et al.*, "Growth of diamond nanocrystals by pulsed laser ablation of graphite in liquid". *Diamond Relat. Mater.*, 2007. **16**(4): p. 725-729.
9. Liu, H. and D.S. Dandy, "Studies on nucleation process in diamond CVD: an overview of recent developments". *Diamond Relat. Mater.*, 1995. **4**(10): p. 1173-1188.

10. Liu, H. and D.S. Dandy, "Diamond Nucleation Mechanisms, in Diamond Chemical Vapor Deposition Nucleation and Early Growth Stages". 1995, *William Andrew Publishing*. p. 46-78.

11. Kumar, A., *et al.*, "Formation of nanodiamonds at near-ambient conditions via microplasma dissociation of ethanol vapour". *Nat. Commun.*, 2013. **4**.

12. Ajji, Z., *et al.*, "Diamond nucleation by seeding from the gas phase". *Appl. Phys. Lett.*, 1995. **67**: p. 3898-3900.

13. Chen, Y.-C. and L. Chang, "Chemical vapor deposition of diamond on silicon substrates coated with adamantane in glycol chemical solutions". *RSC Adv.*, 2013. **3**(5): p. 1514-1518.

14. Chen, Y.-C. and L. Chang, "Chemical vapor deposition of diamond on an adamantane-coated sapphire substrate". *RSC Adv.*, 2014. **4**(36): p. 18945-18950.

15. Narayan, R.J., *et al.*, "Medical applications of diamond particles & surfaces". *Mater. Today*, 2011. **14**(4): p. 154-163.

16. Lee, C.K., "Effects of hydrogen and oxygen on the electrochemical corrosion and wear-corrosion behavior of diamond films deposited by hot filament chemical vapor deposition". *Appl. Surf. Sci.*, 2008. **254**(13): p. 4111-4117.

17. Bull, S.J. and A. Matthews, "Diamond for wear and corrosion applications". *Diamond Relat. Mater.*, 1992. **1**(10): p. 1049-1064.

18. Stehlik, S., *et al.*, "Size decrease of detonation nanodiamonds by air annealing investigated by AFM". *MRS Advances*, 2016. **1**(16): p. 1067-1073.

19. Kidalov, S. and F. Shakhov, "Thermal Conductivity of Diamond Composites". *Materials*, 2009. **2**(4): p. 2467.

20. Fu, C.-C., *et al.*, "Characterization and application of single fluorescent nanodiamonds as cellular biomarkers". *Proc. Natl. Acad. Sci. U.S.A.*, 2007. **104**(3): p. 727-732.

21. Iwasaki, S., *et al.*, "Defining fundamental steps in the assembly of the Drosophila RNAi enzyme complex". *Nature*, 2015. **521**(7553): p. 533-536.

22. Gómez, D.E., *et al.*, "Exciton−Trion Transitions in Single CdSe–CdS Core–Shell Nanocrystals". *ACS Nano*, 2009. **3**(8): p. 2281-2287.

23. Efros, A.L. and D.J. Nesbitt, "Origin and control of blinking in quantum dots". *Nat. Nanotechnol.*, 2016. **11**(8): p. 661-671.

24. Thomas, M.E. and W.J. Tropf, "Optical Properties of Diamond". *Johns Hopkins APL Technical Digest*, 1993. **14**(1): p. 16-23.

25. Fang, C.-Y., *et al.*, "The Exocytosis of Fluorescent Nanodiamond and Its Use as a Long-Term Cell Tracker". *Small*, 2011. **7**(23): p. 3363-3370.

26. Yu, S.-J., *et al.*, "Bright Fluorescent Nanodiamonds: No Photobleaching and Low Cytotoxicity". *J. Am. Chem. Soc.*, 2005. **127**(50): p. 17604-17605.

27. Huang, Y.-A., *et al.*, "The effect of fluorescent nanodiamonds on neuronal survival and morphogenesis". *Sci. Rep.*, 2014. **4**: p. 6919.

28. Mohan, N., *et al.*, "In Vivo Imaging and Toxicity Assessments of Fluorescent Nanodiamonds in Caenorhabditis elegans". *Nano. Lett.*, 2010. **10**(9): p. 3692-3699.

29. Yang, W., *et al.*, "DNA-modified nanocrystalline diamond thin-films as stable, biologically active substrates". *Nat. Mater.*, 2002. **1**(4): p. 253-257.

30. Bradac, C., *et al.*, "Nano-assembly of nanodiamonds by conjugation to actin filaments". *J. Biophotonics*, 2016. **9**(3): p. 296-304.

31. Albrecht, A., *et al.*, "Self-assembling hybrid diamond–biological quantum devices". *New J. Phys.*, 2014. **16**(9): p. 093002.

32. Jozwik, K. and A. Karczemska, "The new generation Ti6Al4V artificial heart valve with nanocrystalline diamond coating on the ring and with Derlin disc after long-term mechanical fatigue examination". *Diamond Relat. Mater.*, 2007. **16**(4): p. 1004-1009.

33. Amaral, M., *et al.*, "Biotribological performance of NCD coated Si3N4–bioglass composites". *Diamond Relat. Mater.*, 2007. **16**(4): p. 790-795.

34. Krauss, A.R., *et al.*, "Ultrananocrystalline diamond thin films for MEMS and moving mechanical assembly devices". *Diamond Relat. Mater.*, 2001. **10**(11): p. 1952-1961.

35. Hegyi, A. and E. Yablonovitch, "Molecular Imaging by Optically Detected Electron Spin Resonance of Nitrogen-Vacancies in Nanodiamonds". *Nano. Lett.*, 2013. **13**(3): p. 1173-1178.

36. McGuinness, L.P., *et al.*, "Quantum measurement and orientation tracking of fluorescent nanodiamonds inside living cells". *Nat. Nanotechnol.*, 2011. **6**: p. 358.

37. Chen, X.-D., *et al.*, "Temperature dependent energy level shifts of nitrogen-vacancy centers in diamond". *Appl. Phys. Lett.*, 2011. **99**(16): p. 161903.

38. Acosta, V.M., *et al.*, "Temperature Dependence of the Nitrogen-Vacancy Magnetic Resonance in Diamond". *Phys. Rev. Lett.*, 2010. **104**(7): p. 070801.

39. Kucsko, G., *et al.*, "Nanometre-scale thermometry in a living cell". *Nature*, 2013. **500**(7460): p. 54-58.

40. Neumann, P., *et al.*, "High-precision nanoscale temperature sensing using single defects in diamond". *Nano Lett*, 2013. **13**(6): p. 2738-42.

41. Xi, G., *et al.*, "Convection-enhanced delivery of nanodiamond drug delivery platforms for intracranial tumor treatment". *Nanomed. Nanotech. Biol. Med.*, 2014. **10**(2): p. 381-391.

42. Dolmatov, V.Y., "Detonation nanodiamonds in oils and lubricants". *J. Superhard Mater.*, 2010. **32**(1): p. 14-20.

43. Valerii Yu, D., "Detonation synthesis ultradispersed diamonds: properties and applications". *Russ. Chem. Rev.*, 2001. **70**(7): p. 607.

44. Chu, Z., *et al.*, "Unambiguous observation of shape effects on cellular fate of nanoparticles". *Sci. Rep.*, 2014. **4**: p. 4495.

45. Spitsyn, B.V., *et al.*, "Vapor growth of diamond on diamond and other surfaces". *J. Cryst. Growth*, 1981. **52**(1): p. 219-226.

46. Kamo, M., "Synthesis of diamond from gas phase and its properties". *The Rigaku Journal*, 1990. **7**(2): p. 22-27.

47. Wei, J. and Y. Tzeng, "Growth of diamond by sequential deposition and etching process using hot filament CVD". *J. Cryst. Growth*, 1993. **128**(1): p. 413-417.

48. Seiichiro, M., *et al.*, "Vapor Deposition of Diamond Particles from Methane". *Jpn. J. Appl. Phys.*, 1982. **21**(4A): p. L183.

49. Matsumoto, S., *et al.*, "Growth of diamond particles from methane-hydrogen gas". *J. Mater. Sci.*, 1982. **17**(11): p. 3106-3112.

50. Sawabe, A., *et al.*, "Growth of diamond thin films in a DC discharge plasma". *Appl. Surf. Sci.*, 1988. **33**: p. 539-545.

51. Suzuki, K., *et al.*, "Growth of diamond thin films by dc plasma chemical vapor deposition". *Appl. Phys. Lett.*, 1987. **50**(12): p. 728-729.

52. Aoyama, K., *et al.*, "Diamond deposition with Ar-CO2-CH4-H2 plasma jets". *Diamond Relat. Mater.*, 1993. **2**(2): p. 337-341.

53. Kotaki, T., *et al.*, "Diamond deposition from an Ar-CCl4-H2 plasma jet at 13.3 kPa". *Diamond Relat. Mater.*, 1993. **2**(2): p. 342-346.

54. Matsumoto, S., "Chemical vapour deposition of diamond in Rf glow discharge". *J, Mater, Sci, Lett,*, 1985. **4**(5): p. 600-602.

55. Matsumoto, S., *et al.*, "Synthesis of diamond films in a rf induction thermal plasma". *Appl. Phys. Lett.*, 1987. **51**(10): p. 737-739.

56. Laimer, J., *et al.*, "Growth of diamond in an electrodeless capacitive RF discharge". *Int. J. Refract. Met. Hard Mater.*, 1996. **14**(1): p. 173-178.

57. Gries, T., *et al.*, "Diagnostics in dusty C–H–O plasmas with diamond and graphitic nanoparticle generation". *Plasma Sources Sci. Technol.*, 2010. **19**(2): p. 025015.

58. Kamo, M., *et al.*, "Diamond synthesis from gas phase in microwave plasma". *J. Cryst. Growth*, 1983. **62**(3): p. 642-644.

59. Chen, C.-F., *et al.*, "Growth of diamond from CO2-(C2H2, CH4) gas systems, without supplying additional hydrogen gas". *Surf. Coat. Technol.*, 1992. **52**(3): p. 205-209.

60. Frenklach, M., *et al.*, "Homogeneous nucleation of diamond powder in the gas phase". *J. Appl. Phys.*, 1989. **66**(1): p. 395-399.

61. Frenklach, M., *et al.*, "Induced nucleation of diamond powder". *Appl. Phys. Lett.*, 1991. **59**(5): p. 546-548.

62. D. V. Fedoseev, *et al.*, "Homogeneous formation of a diamond in the gaseous phase". *JETP Lett.*, 1980. **32**(1).

63. Bachmann, P.K., *et al.*, "Towards a general concept of diamond chemical vapour deposition". *Diamond Relat. Mater.*, 1991. **1**(1): p. 1-12.

64. Han, Y.X., *et al.*, "Enhanced diamond nucleation on copper substrates by graphite seeding and CO2 laser irradiation". *Appl. Surf. Sci.*, 2008. **254**(7): p. 2054-2058.

65. Rajanish, N.T. and C. Li, "Chemical Precursor for the Synthesis of Diamond Films at Low Temperature". *Appl. Phys. Express*, 2010. **3**(4): p. 045501.

66. Tsugawa, K., *et al.*, "Nucleation Enhancement of Nanocrystalline Diamond Growth at Low Substrate Temperatures by Adamantane Seeding". *J. Phys. Chem. C*, 2010. **114**(9): p. 3822-3824.

67. Tzeng, Y.-K., *et al.*, "Vertical-Substrate MPCVD Epitaxial Nanodiamond Growth". *Nano. Lett.*, 2017. **17**(3): p. 1489-1495.

68. Liu, W., *et al.*, "Nucleation of oriented diamond particles on cobalt substrates". *J. Appl. Phys.*, 1995. **78**(2): p. 1291-1296.

69. Gaebel, T., *et al.*, "Size-reduction of nanodiamonds via air oxidation". *Diamond Relat. Mater.*, 2012. **21**(Supplement C): p. 28-32.

70. Stehlik, S., *et al.*, "High-yield fabrication and properties of 1.4 nm nanodiamonds with narrow size distribution". *Sci. Rep.*, 2016. **6**: p. 38419.

71. "Ultraviolet-Ozone Surface Treatment, in Three Bond Technical News". 1987. **17**(20), *Three Bond Group*.

72. Vig, J.R., "UV/ozone cleaning of surfaces". *J. Vac. Sci. Technol., A*, 1985. **3**(3): p. 1027-1034.

73. Bazyleva, A.B., *et al.*, "Thermodynamic Properties of Adamantane Revisited". *J. Phys. Chem. B*, 2011. **115**(33): p. 10064-10072.

74. Mokbel, I., *et al.*, "Vapor pressures and thermal data for three high-boiling compounds of petroleum interest: 1-phenyldodecane, (5α)-cholestane, adamantane". *Fluid Phase Equilib.*, 2000. **169**(2): p. 191-207.

75. Ganeff, J.M. and J.C. Jungers, "Tensions de Vapeur du Systeme CH3Cl - CH2Cl2". *Bull. Soc. Chim. Belg.*, 1948. **57**(1-3): p. 82-87.

76. Jariwala, B.N., *et al.*, "Atomic hydrogen interactions with amorphous carbon thin films". *J. Appl. Phys.*, 2009. **106**(7): p. 073305.

77. Vohler, O., *et al.*, "Carbon, 2. Diamond, in Ullmann's Encyclopedia of Industrial Chemistry". 2000, *Wiley-VCH Verlag GmbH & Co. KGaA*.

78. Kumar, N., *et al.*, "High-temperature phase transformation and low friction behaviour in highly disordered turbostratic graphite". *J. Phys. D: Appl. Phys.*, 2013. **46**: p. 395305.

79. Ferrari, A.C. and J. Robertson, "Interpretation of Raman spectra of disordered and amorphous carbon". *Phys. Rev. B*, 2000. **61**(20): p. 14095-14107.

80. Ferrari, A.C. and J. Robertson, "Raman spectroscopy of amorphous, nanostructured, diamond–like carbon, and nanodiamond". *Phil. Trans. R. Soc. Lond. A*, 2004. **362**(1824): p. 2477-2512.

81. Chung, D.D.L., "Review Graphite". *J. Mater. Sci.*, 2002. **37**(8): p. 1475-1489.

82. Xiang, C., *et al.*, "Nitrogen-Doped Bagasse-Derived Carbon/ Low Pt Composite as Counter Electrodes for High Efficiency Dye-Sensitized Solar Cell". *J. Electrochem. Soc.*, 2017. **164**(4): p. H203-H210.

83. Hardwick, L.J., *et al.*, "An Investigation of the Effect of Graphite Degradation on Irreversible Capacity in Lithium-ion Cells". *J. Electrochem. Soc.*, 2008. **155**(6): p. A442-A447.

84. Eckmann, A., *et al.*, "Probing the Nature of Defects in Graphene by Raman Spectroscopy". *Nano. Lett.*, 2012. **12**(8): p. 3925-3930.

85. Xu, L. and L. Cheng, "Graphite Oxide under High Pressure: A Raman Spectroscopic Study". *J. Nanomater.*, 2013. **2013**: p. 5.

86. Yokosawa, K., *et al.*, "The possibility of diamond sintering by hydrothermal hot-pressing". *AIP Conference Proceedings*, 2006. **833**(1): p. 100-103.

87. Yamasaki, N., *et al.*, "Synthesis of Diamond Particles under Alkaline Hydrothermal Conditions". *Solid State Phenomena*, 2006. **114**: p. 271-276.

88. Korablov, S., *et al.*, "Hydrothermal formation of diamond from chlorinated organic compounds". *Mater. Lett.*, 2006. **60**(25): p. 3041-3044.

89. Korablov, S., *et al.*, "Synthesis of diamond from a chlorinated organic substance under hydrothermal conditions". *J. Mater. Sci.*, 2007. **42**(18): p. 7939-7949.

90. Coleman, D., *et al.*, "Hollow silicon carbide nanoparticles from a non-thermal plasma process". *J. Appl. Phys.*, 2015. **117**(19): p. 193301.

91. Bray, K., *et al.*, "Localization of Narrowband Single Photon Emitters in Nanodiamonds". *ACS Appl. Mater. Interfaces*, 2016. **8**(11): p. 7590-7594.

92. Sandstrom, R.G., *et al.*, "Study of narrowband single photon emitters in polycrystalline diamond films". *Appl. Phys. Lett.*, 2014. **105**(18): p. 181104.

93. Zaitsev, A.M., "Titl". 1 ed. 2001, New York: *Springer-Verlag Berlin Heidelberg*. 502.

94. Fukata, N., *et al.*, "Hydrogen molecules and hydrogen-related defects in crystalline silicon". *Phys. Rev. B*, 1997. **56**(11): p. 6642-6647.

95. Takashi, S. and H. Akio, "Detailed Study of Si-H Stretching Modes in μc-Si: H Film through Second Derivative IR Spectra". *Jpn. J. Appl. Phys.*, 1985. **24**(7A): p. L491.

96. Johnson, E.V., *et al.*, "Raman scattering analysis of SiH bond stretching modes in hydrogenated microcrystalline silicon for use in thin-film photovoltaics". *Sol. Energy Mater. Sol. Cells*, 2009. **93**(10): p. 1904-1906.

APPENDIX A

RF setup cleaning procedure:

1. Under vacuum overnight [or pump down to the base pressure (**20mTorr**)].
2. Run Ar in the beginning and after **3min** run the plasma then take OES [For Carbon and H_2 check]
3. Turn off the plasma as well as Ar MFC.
4. If there are carbon peaks in the OES go to step #5 for cleaning, if not go to step #9.
5. Run H_2 at full scale **(5.00 SP)** and turn the plasma on at **100W** for **10-15min**. Take OESs during the cleaning.
6. Turn off the plasma as well as H_2/CH_4 MFC.
7. Pump down to the base pressure (**20mTorr**).
8. Run Ar and turn the plasma on to check for carbon again.
9. To purge the H_2/CH_4 MFC from H_2 turn it on at full scale **(5.00 SP)** as well as the valves after and before it (**Note: make sure H_2 and CH_4 valves off**)
10. Pump H_2/CH_4 MFC down to the base pressure (**20mTorr**).
11. Turn off the valve after H_2/CH_4 MFC then pump down the lines (i.e., upstream and downstream lines) for **several minutes**.
12. Turn the CH_4 valve on as well as the valve after H_2/CH_4 MFC for purge for 15min.
13. Turn off the H_2/CH_4 MFC and the valves.
14. Pump down to the base pressure (**20mTorr**).

15. Purge up and down stream lines with Ar for **5min** three times and pump down for **8min** between them [three times to reach the base pressure (**20mTorr**)].
16. Turn the plasma on and then take OES.
17. Turn the plasma off and shut off the bypass valve then pump down through the filter line.
18. Adjust the closer needle valve to the pump to fix rector's pressure to the required.
19. Then decrease Ar flow rate and inject the precursor to the desired conditions.
20. After **5min,** turn the plasma on for running full experiment and take OESs.

APPENDIX B

Influence of O_2/DCM ratio and dilution level on OES spectrums:

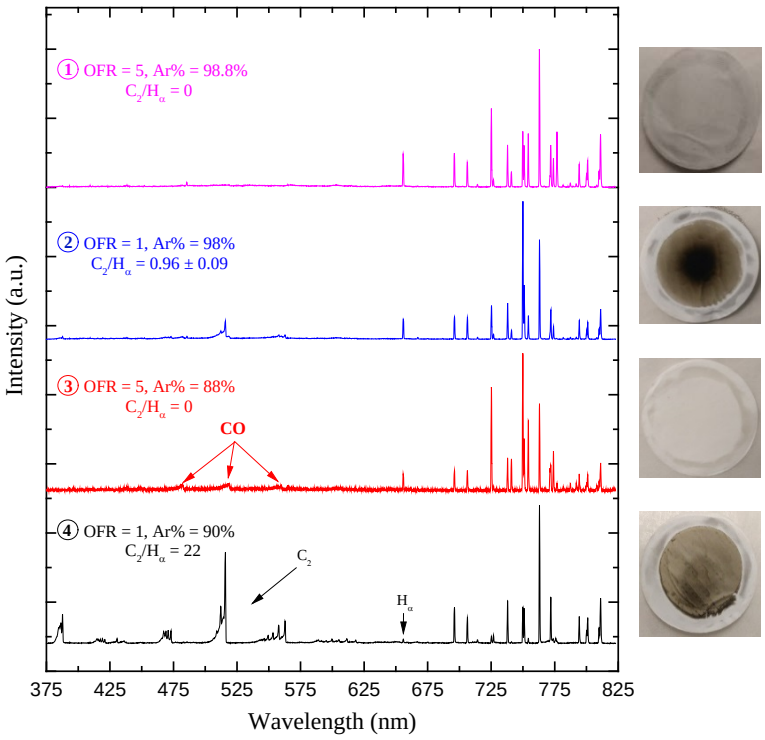

Figure B- 1: OES of the DCM and O_2 mixtures (experiments' conditions see Table 8).

Increasing the concentration of O_2 in the gasous mixture caused the emergence of carbon monoxide's (CO) peaks in the OES as shown in Experiment (3) in Figure (B-1). The flow rates of the Ar, DCM, and O_2 were 44, 1, and 5 sccm respectively. The OFR was calculated from equation (21) and Ar% from equation (22).

APPENDIX C

Raman spectra of four of the $CH_4/H_2/SiH_2$ experiments:

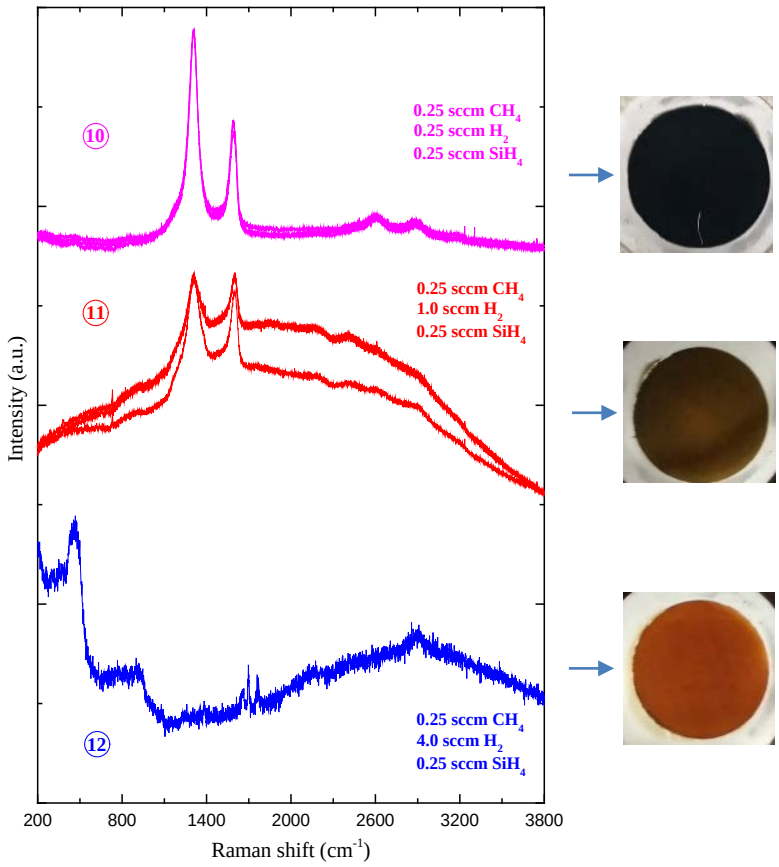

Figure C - 1: Raman spectra of material collected under different reactants' concentrations (experiments' conditions see Table 9).

The cause of the strange behavior of the Raman spectrum of Experiment (12) is unclear. The positions of the peaks made identifying their origin more difficult. No further examination was done on the sample.

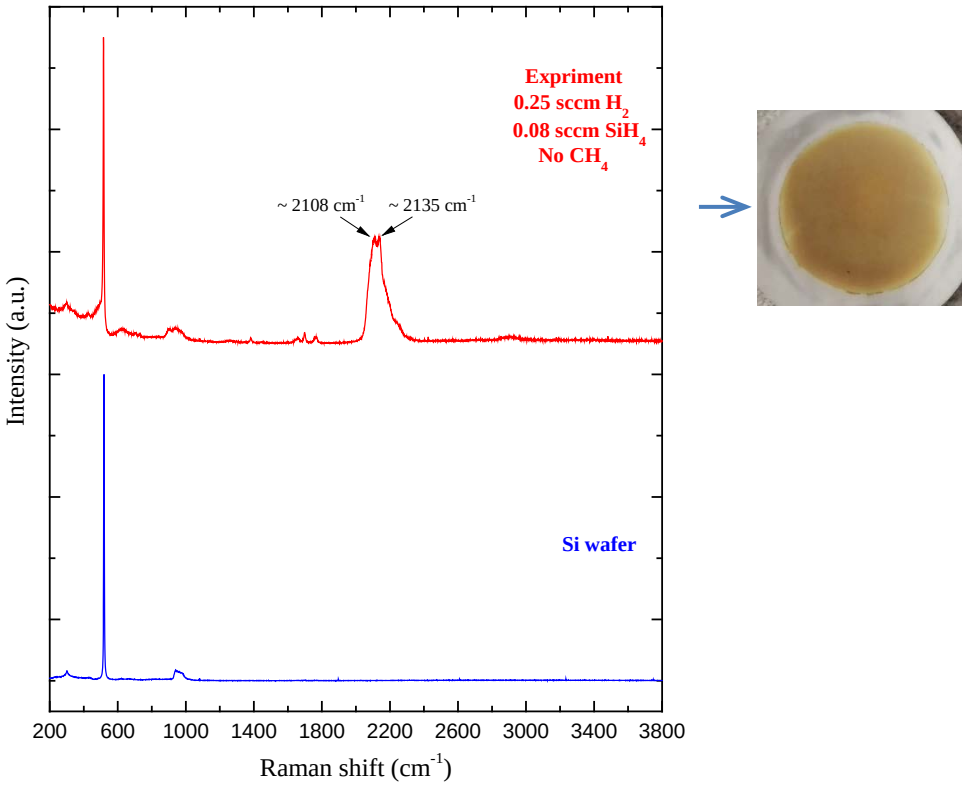

Figure C - 2: Raman spectra of material collected and Si wafer.

The consequence of raising the silane to 0.08 sccm and maintaining the H_2 to be 0.25 sccm, was that twin peaks was observed as displayed in Figure C-2. The cause of these peaks might correspond to Si-H stretching modes on Si (111) and (110) faces [94-96].